A FABRY-PEROT INTERFEROMETER AND ITS APPLICATIONS TO MEASUREMENT OF THE THERMOSPHERIC TEMPERATURES AND WINDS

A Thesis for the Degree of Doctor of Philosophy

in the University of Adelaide

submitted by

Anthony Richard David Bower B.Sc. (Hons)

The Mawson Institute for Antarctic Research

August 1974

CONTENTS

SUMMARY (i)

STATEMENT (ii)

ACKNOWLEDGEMENTS (iii)

CHAPTER

1. INTRODUCTION 1

2. THE FABRY-PEROT INTERFEROMETER 4

2.1 Introduction 4
2.2 Principles of the Fabry-Perot Interferometer 6
2.2.1 The étalon 6
2.2.2 Recording the Spectrum 7
2.2.3 Scanning the Spectrum 8
2.3 Instrument Function 11
2.3.1 The Airy Function 12
2.3.2 Defect Functions 13
2.3.3 Aperture Function 13
2.3.4 Recorded Function 14
2.4 Resolving Power and Light Gathering Power 15

3. DEVELOPMENT OF THE FABRY-PEROT INTERFEROMETER 17

3.1 Introduction 17
3.2 Piezoelectric Stacks 17
3.3 Parallelism Control 19
3.3.1 Test on Original Design 20
3.3.2 Design Modifications 21
3.4 Separation Control 21
3.4.1 Differential Transformer Displacement Transducer 22
3.4.2 Capacitance Transducer 22
3.5 Temperature Control 25
3.5.1 Air Temperature Control 25
3.5.2 Ancillary Heaters 27
3.6 Installation at Mount Torrens 27

4. THE MAWSON INSTITUTE FABRY-PEROT INTERFEROMETER 30

4.1 Optical and Mechanical Design 30
4.1.1 Optical Design and Adjustment 30
4.1.2 Mechanical Details 32
4.2 The Plates 33
4.2.1 Testing for Flatness 34
4.2.2 Coatings 36
4.3 Parallelism Control 38
4.3.1 Basic Principles 38
4.3.2 Collimated Light Sources and Detectors 40
4.3.3 Gain Requirements 41
4.4 Separation Control 41
4.4.1 Capacitance Displacement Transducer 42
4.4.2 The Servo Loop 43
4.4.3 Barometer 44
4.4.4 Scanning the FPI 45

4.5 Temperature Control 46
4.5.1 Basic Principles 47

5. DETECTION OF VERY LOW LIGHT LEVELS 48

5.1 Introduction 48
5.2 The Photomultiplier Tube 49
5.3 Quantum Efficiency Enhancement by Total Internal Reflection 50
5.3.1 Introduction 50
5.3.2 Preliminary Measurements 51
5.3.2.1 Measurements on Photomultiplier Tube 51
5.3.2.2 Design Considerations 52
5.3.3 Hirschfeld Cone 53
5.4 Reduction of Dark Current 55
5.4.1 Temperature Dependence 55
5.4.2 Magnetic Defocusing 56
5.4.3 Electrostatic Shielding 60
5.5 Detection Systems 60
5.5.1 Analogue Detection 60
5.5.2 Pulse Counting 61
5.6 Photomultiplier Chamber 63
5.6.1 Shutter Control 64
5.6.2 Cooling System 64
5.7 Concluding Remarks 65

6. OPERATIONAL PROCEDURE AND ANALYSIS OF THE RESULTS 67

6.1 Selection of the Order of Interference 67
6.2 Calibration 69
6.2.1 Mercury Lamp and He-Ne Laser 70
6.2.2 Procedure 71
6.2.3 Results 71
6.3 Collection of Results 72
6.4 Analysis of Results 73
6.4.1 Manipulation of the Data 73
6.4.1.1 Indexed Sequential Filing System 75
6.4.2 Analysis Technique 75
6.5 Operational Characteristics 78

7. THERMOSPHERIC TEMPERATURES AND WINDS 81

7.1 Introduction 81
7.2 Review of Earlier Observations 81
7.2.1 FPI Measurements 81
7.2.1.1 Temperatures 81
7.2.1.2 Winds 83
7.2.2 Measurements by Other Methods 84
7.2.2.1 Satellite Observations 84
7.2.2.2 Chemical Releases 84
7.2.2.3 Thomson Scattering 85
7.2.2.4 Michelson Interferometer 85
7.3 Results Obtained at Mount Torrens 86
7.3.1 Contamination by Hydroxyl Emissions 86
7.3.2 Kinetic Temperatures 88
7.3.2.1 Diurnal Variation 88
7.3.2.2 Dependence on Magnetic Activity 90
7.3.3 Neutral Winds 91
7.3.3.1 Diurnal and Seasonal Variation 91
7.3.3.2 Winds During Magnetic Disturbances 93
7.3.3.3 Comparison with Models 95
7.4 Concluding Remarks 96

8. CONCLUSION AND SUGGESTIONS FOR FUTURE WORK 97

APPENDIX ELECTRONIC CIRCUITRY 98

Parallelism Control 98
Three Phase Oscillator 98
PIN Diode Preamplifier 98
Bandpass Filter and Phase Sensitive Detector 99
The Equalizer 100
600V Supply 100
Stabilized Power Supplies 100
Adjustments 101

Separation Control 102
10 kHz Oscillator 102
Differential Amplifier 102
10 kHz Rectifier 103
Equalizer 105
Scan Input Attenuator 105

Temperature Control 107
Error Amplifier and Triac Trigger 107
Triac Switch 108

Pulse Counting Electronics 109
Preamplifier and Discriminator 109
Ratemeter 109

Photomultiplier Shutter Control Electronics 110

BIBLIOGRAPHY 112

SUMMARY

A 15cm scanning Fabry-Perot Interferometer was used to measure the doppler width and shift of the atomic oxygen [OI] λ630nm line in the night airglow. From these measurements over a 12 month period at Mt. Torrens (near Adelaide) kinetic temperatures and neutral wind velocities have been determined.

The theory of the Fabry-Perot Interferometer (FPI) is presented with emphasis on the criteria involved in the selection of operating parameters. The development of the FPI constructed in the Mawson Institute for Antarctic Research is outlined and a detailed description of the instrument is then given. Full particulars are given of the servo-systems which were developed to control parallelism and separation of the FPI plates and to maintain high thermal stability within the instrument.

The detection of very low light levels such as are encountered in the night airglow, was the subject of considerable investigation. Work carried out in this area led to refinements in the detection system which increased the signal-to-noise ratio by almost two orders of magnitude.

Observations during periods of low magnetic activity revealed diurnal patterns in temperature and wind velocity broadly in agreement with previous observations. The zonal component of the neutral wind is observed to have a pronounced seasonal variation.

Enhancements of the temperature and the meridional component of the wind were found always to accompany magnetic disturbances. Equatorward winds with velocity greater than 200m/sec were found to be present even during fairly minor magnetic disturbances.

STATEMENT

This thesis contains no material which has been accepted for the award of any other degree or diploma in any University and, to the best of the author's knowledge, it contains no material previously published or written by another person, except where due reference is made in the text.

(A.R.D. Bower)

ACKNOWLEDGEMENTS

The research work described in this thesis has been greatly assisted by the cooperation of the personnel of the Mawson Institute for Antarctic Research, The University of Adelaide. In particular, special thanks are extended to Dr. F. Jacka, Director of the Mawson Institute for Antarctic Research, for his suggestion of the research topic, for active participation in the development of the Fabry-Perot Interferometer and for his guidance and constructive criticism during the preparation of the material and ideas presented in this thesis. The author's co-worker, Mr. P.A. Wilksch made significant contributions during the developmental and observational stages of the project and was also responsible for developing the technique for analyzing the results. Thanks are also extended to Mr. D.F. Creighton for his assistance in developing the Fabry-Perot Interferometer.

The author acknowledges the assistance of Mrs. M. Molnar, who typed this thesis and to Mrs. L. Lomax who prepared some of the diagrams.

The research was carried out while the author was supported by a Commonwealth Postgraduate Award.

CHAPTER 1

INTRODUCTION

The night airglow was discovered over fifty years ago and has been the subject of considerable study ever since. The investigations have been made with an array of instrumentation, such as spectrographs for identifying the emissions that constitute the airglow and photometers for measuring the intensities of these emissions. Studies of the airglow from Mount Torrens (near Adelaide) have been carried out for a number of years. Schaeffer (1970) made extensive measurements of the intensity of emission of the forbidden atomic oxygen line at λ630nm. This thesis describes the development of a Fabry-Perot Interferometer to continue observations of this emission line and the results of these observations. The aim of this project was to make measurements of the thermospheric temperatures and winds. These measurements can be achieved by a number of techniques, which may be divided into two categories; namely ground-based or in-situ observations. The former category includes measurement of the doppler broadening and shift of atomic emission lines, from which the kinetic temperature and neutral wind can be deduced. Another ground-based technique is the measurement of the electron and ion temperatures and winds using incoherent scatter radar. The in-situ observations include the determination of the neutral wind by measurement of the slight changes in the inclination of satellites' orbits to the equator. Releases of chemical impurities from rockets can also be used to obtain information about the temperatures and winds in the upper atmosphere.

In Chapter 2, a justification is given for the choice of a Fabry-Perot interferometer (FPI) to measure doppler widths and shifts of the oxygen [OI] λ630nm emission line. This emission line results from excitation of the oxygen atom to the ^1D level. In the night airglow this is primarily achieved by dissociative recombination of electrons with O_2^+, (Schaeffer, 1970). The principal chemical reactions are:

$$O^+ + O_2 \rightarrow O_2^+ + O + 1.53 \text{ eV} \qquad \ldots(1.1)$$

$$O_2^+ + e \rightarrow O + O + 6.96 \text{ eV} \qquad \ldots(1.2)$$

The $O(^1D)$ state has a very long mean lifetime of approximately 110 sec and so emission from the atmosphere below 200km is unimportant due to collisional deactivation. The dominant species for deactivation of $O(^1D)$ is considered to be N_2 (Schaeffer, 1970).

The height profiles of electron density, O_2, O and N_2 thus determine the height distribution of the λ630nm emission. The electron density peaks at approximately 300km, while the three neutral densities decrease with increasing height in the region of interest. The λ630nm emission therefore, peaks at approximately 250km, which is slightly below the peak of the electron density height profile.

In Chapter 3, the development of the Mawson Institute FPI is described and then in Chapter 4 a full description of this instrument is given. The author devoted considerable time to the study of the detection of very low light levels and the results of this work are presented in Chapter 5. The operational procedure for the FPI and the technique for analyzing the results are described in Chapter 6.

In Chapter 7, the results obtained from Mt. Torrens (near Adelaide) are presented. The temperature and wind measurements are

given separately and careful distinction is made between magnetically disturbed and quiet periods. A brief conclusion and suggestions for future research are given in Chapter 8.

CHAPTER 2

THE FABRY-PEROT INTERFEROMETER

2.1 Introduction

Interferometry has been applied to the study of the night sky from as early as 1923, when Babcock used a Fabry-Perot Interferometer (FPI) to determine the wavelength of the λ557.7nm line of atomic oxygen, emitted in the aurora. Until recently the FPI was only used to measure the temperature of the layers emitting the λ630 nm and the λ557.7nm lines of atomic oxygen. The spectral line width is determined by doppler broadening and at half maximum has a value given by the Buisson and Fabry (1911) relation,

$$h = 7.16 \times 10^{-7} \lambda (T/M)^{1/2} \qquad (2.1)$$

where λ is the wavelength of the emission, T is the temperature in degrees absolute and M the atomic weight of the emitting atoms. From our own work and that of previous investigators, it is known that the F-region of the upper atmosphere, from which the λ630nm line emanates normally has a temperature in the range 500-1500°K. From (2.1) this corresponds to λ630nm line widths in the range 2.5-4.4pm. This implies that the instrument employed in the measurement of such widths must be capable of high resolution. This requirement can be met by the prism spectrometer, the grating spectrometer, the Fabry-Perot interferometer, and the Michelson interferometer. The relative merits of the prism, grating and Fabry-Perot spectrometers have been discussed by Jacquinot(1954). He compared the light gathering power of the three different instruments with, in each case, equal resolving power and dimensions. He found that the FPI is vastly superior for any choice of resolution and

so it would be the obvious choice for studies of low level light sources, such as the nightglow.

The Michelson interferometer is comparable to the FPI in light collecting power for a given resolution (Hunten et al, 1967). It is possible greatly to improve the Michelson interferometer by the use of field-compensation, first suggested by Connes (1956). This technique has been utilized by Hilliard and Shepherd (1966a) in the construction of a wide angle Michelson interferometer (WAMI). The principal improvement is that the WAMI light gathering power may be of the order of a thousand times greater than that of the FPI at the same effective resolution.

The WAMI can, however, only be used when the background continuum from the night sky is easily determined. Hilliard and Shepherd (1966b) have used this instrument to study the λ557.7nm line in the aurora and nightglow, with very good time resolution. This line lies in a region which is relatively free of other emission lines, (Broadfoot and Kendall, 1968). The hydroxyl band OH(7-1) which is distributed either side of the λ557.7nm line has a total band intensity of only 22R , (Chamberlain and Smith, 1959).

The λ630nm line, however, lies amidst the much stronger OH(9-3) band, which is reported by Chamberlain and Smith (1959) to have a total band intensity of 110R. In particular the $P_1(2)$ line at 628.76nm and the $P_1(3)$ line at 630.68nm would make the analysis of results obtained with the WAMI very difficult to interpret. Since the study of the λ630nm line was the main aim of this project it was decided that the FPI was the most useful instrument for this purpose.

If the oxygen atoms emitting the lines are undergoing a gross movement relative to the FPI, then the lines will exhibit a wavelength shift,

$$\delta\lambda = \lambda v/c \qquad (2.2)$$

where λ is the wavelength of the emission line, v is the line-of-sight velocity and c is the velocity of light. Winds in the F-region of the upper atmosphere are of the order of $100ms^{-1}$, which corresponds to a wavelength shift in the λ630nm line of 2×10^{-4}nm. Since the FPI is more suitable for the measurement of wavelength shifts than the Michelson interferometer, this was another reason for the selection of the former.

2.2 Principles of the Fabry-Perot Interferometer

2.2.1 The étalon

The basic principles of the FPI can be found in most optical textbooks; see for example Born and Wolf (1965). The FPI in its most basic form is illustrated in Figure 1. The basic element of the FPI (usually called the étalon) is a pair of transparent plates which have their adjacent faces polished very flat and are maintained parallel to a high degree of accuracy. The deviations from flatness and parallelism are usually expressed as a fraction of the wavelength λ546.1nm of the mercury green line. The adjacent faces of the étalon are covered with coatings of high reflection coefficient R, with low absorption coefficient, given by

$$A = 1 - R - T \qquad (2.3)$$

where T is the transmission coefficient.

A ray of light incident on the étalon is divided by multiple

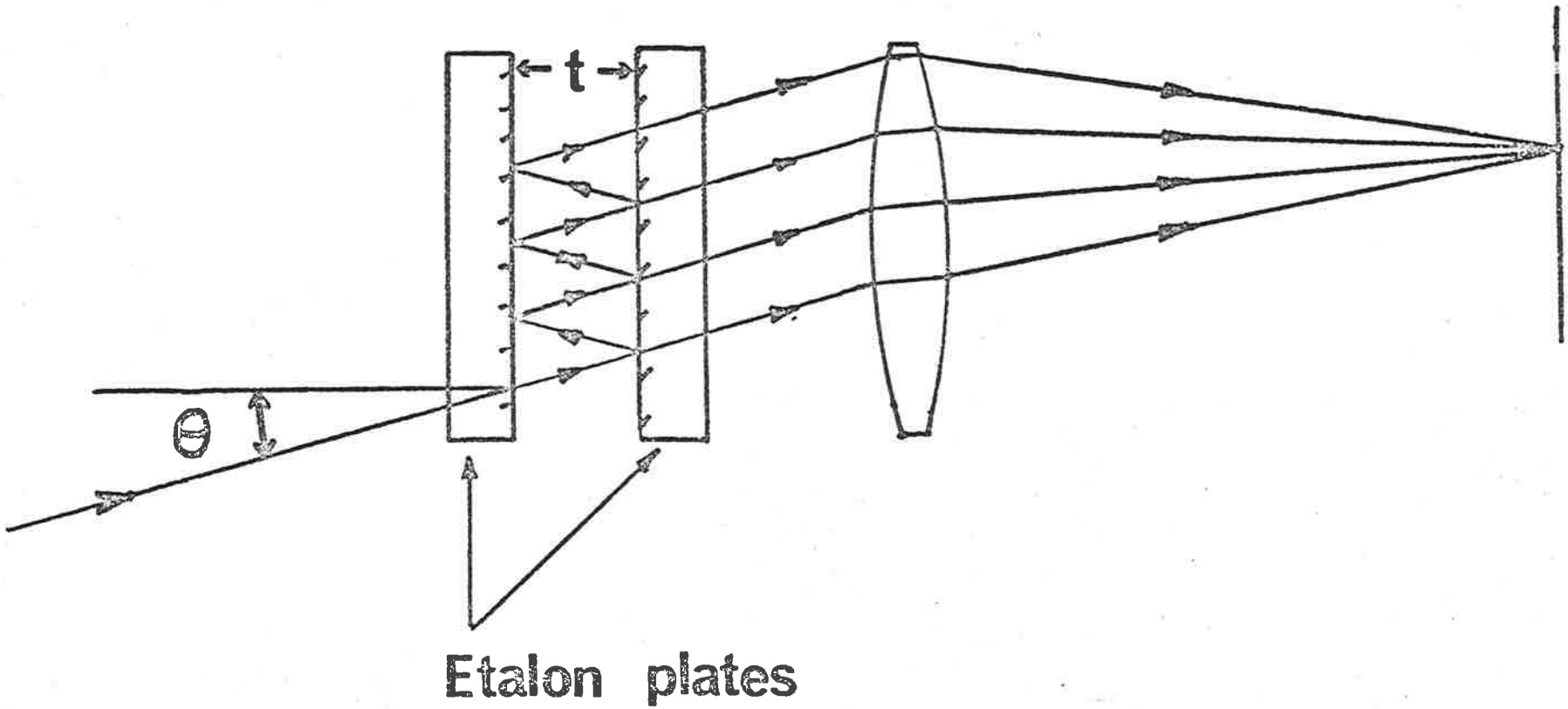

FIG. 1. The Fabry-Perot Interferometer.

transmissions and reflections into a series of parallel transmitted and reflected rays. The transmitted rays are brought together by the lens to form an interference pattern in the focal plane. The circular fringes produced from a monochromatic source are known as fringes of equal inclination or Haidinger fringes. Each transmitted ray is optically retarded relative to the preceding ray by a path length, P which is given by,

$$P = 2nt \cos\theta \qquad (2.4)$$

where n is the refractive index of the medium between the plates and t is the plate spacing. If the order of interference m, defined as $m = P/\lambda$ has an integral value then constructive interference occurs; and if m is non-integral then transmitted rays destructively interfere and the incident energy is reflected.

2.2.2 Recording the Spectrum

Prior to the development of the photomultiplier tubes the method of recording the FPI fringes was to place a photographic plate in the focal plane of the lens, shown in Figure 1. When applied to the study of low level light sources such as the nightglow (Wark and Stone, 1954), very long exposure times were required. Other disadvantages of photographic recording, such as difficulty of analysis, have been discussed by Karandikar (1959).

The FPI is utilised as a spectrometer by replacing the photographic plate with an annular diaphragm and then allowing the portion of the fringe pattern selected by the diaphragm to pass to a photomultiplier tube. In practice, the annular diaphragm has zero internal diameter and is therefore a circular aperture. Jacquinot

and Dufour (1948) suggested the use of several concentric annular diaphragms, which would increase the light gathering power of the FPI. This mask would be very difficult to construct and so this suggestion has not been utilised, to date. With the circular aperture at the centre of the fringe pattern this defines a series of wavelengths $\lambda_m = P/m$ which will be detected by the photomultiplier tube, where m is the order of interference. This implies that some form of pre-monochromator is required to isolate the wavelength of interest.

To scan over a range of wavelengths, the optical retardation, P is varied. From equation (2.4) it can be seen that this is achieved by varying any one of n, t or θ. The FPI described in this thesis utilises the variation of t, the plate spacing and the reasons for this selection will be given in the next section.

2.2.3 Scanning the Spectrum

The three basic methods of scanning have been reviewed by a number of authors, including Karandikar (1959), Jacquinot (1960) and more recently by Shepherd (1967). By far the most popular method, particularly in studies of the upper atomosphere, has been the variation of refractive index, or pressure scanning. The refractive index of a gas at constant temperature is directly proportional to its pressure for small scanning ranges. The range of the wavelength scan $d\lambda$, is obtained from equation (2.4) and $\lambda = P/m$, namely,

$$d\lambda = \frac{\lambda}{n} dn = \lambda k dp \qquad (2.5)$$

where dp is the pressure change and k is a constant which depends

on the gas used. Jacquinot (1960) quotes a value of $k = 3 \times 10^{-4}$ per atmosphere for air, which corresponds to a wavelength scanning range of approximately 0.2nm at λ630nm, for a one atmosphere pressure change. This range is independent of the plate spacing and so this method of scanning is used primarily for high resolution studies. The scanning range can be increased by using a gas of higher refracitive index, such as Freon (Nilson and Shepherd, 1961) or by varying the pressure by more than one atmosphere. The chief disadvantage of this method is the slow scan rate, which is required to prevent temperature variations in the medium between the plates. Biondi and Feibelman (1968) have achieved a scan through one interference order in ∿1 minute, however, this is still somewhat slow for observation of the twilight glow or the aurora.

The second method involves the variation of the spacing between the plates by translating one plate relative to the other. The relationship between wavelength scan range $d\lambda$, and the variation in spacing dt, is

$$d\lambda = \frac{\lambda}{t} dt \qquad (2.6)$$

This implies that the range of the scan increases as the spacing decreases. Karandikar (1959)discusses the various techniques involved in achieving the spacing variation; magnetostrictive or piezoelectric supports for the FPI plates seem to be the most useful.

Magnetostrictive variation of the spacer length has been successfully applied by Slater et al. (1965) in the construction of a rugged FPI for rocket observations of the dayglow. In order to obtain a reasonable scanning range, however, large currents must be

passed through the magnetizing coils, which may cause thermal problems.

Piezoelectric scanning, however, involves very low power consumption and so thermal effects are insignificant. Studies on the behaviour of lead titanate ceramics are reported later in this thesis and reveal hysteresis and creep phenomena, which complicate the use of these materials. Another limitation is the restricted range of movement obtainable without the use of unduly high voltages. The latter difficulty has been overcome by Ramsay and Mugridge (1962) who used a stack of piezoelectric discs to increase the expansion coefficient.

The difficulty common to both these techniques, is that of keeping the plates parallel to a high degree of accuracy during the scan. The servo-parallelism control system devised by Ramsay (1962), which is applied to a piezoelectrically scanned FPI is capable of maintaining the plates parallel to within the error of flatness of the interferometer surfaces.

The third scanning method involves changing the angle of incidence θ, by either rotating the étalon (Karandikar, 1959) or by displacing the aperture. The latter has been discussed by Shepherd et al. (1965) and involves the expansion of the annular aperture whilst maintaining its area constant. This method involves great mechanical difficulties and has so far been little used.

The piezoelectric scanning system with servo parallelism control was chosen for the Mawson Institute FPI for the following reasons. It makes possible the study of auroral and twilight phenomena because of the rapid scan rate; it eliminates the need for

routine adjustments to parallelism and,because the mean separation of the plates can be reset quite quickly, it is far more versatile than most conventional pressure scanning instruments.

2.3 Instrument Function

The Fabry-Perot Interferometer is in practice an instrument of finite resolution, which implies that the instrument transmission versus wavelength function is of finite width. Three independent proporties of the FPI contribute to the instrument function. These are the flatness of the étalon plates, the reflectivity and absorption of the coatings applied to these plates and the aperture which limits the field of view of the instrument. In this section, a function describing each of these properties will be defined. The overall instrument function is the convolution of these three functions. The convolution of two functions $X(\lambda)$ and $Y(\lambda)$ is defined as

$$Z(\lambda_0) = \int_0^\infty X(\lambda)Y(\lambda-\lambda_0)d\lambda \qquad (2.7)$$

This is denoted as

$$Z = X * Y \qquad (2.8)$$

The three functions contributing to the instrument function will be introduced in a manner similar to that employed by Chabbal (1953). An elegant summary of this approach is presented by Jacquinot (1960) in a review paper on interference spectroscopy. More recently Hernandez (1966) has obtained an analytical description of the FPI.

2.3.1 The Airy Function

Assuming the étalon to have plates which are perfectly smooth and parallel and to have coatings with reflection coefficient less than one, the instrumental function is the Airy function (Jacquinot, 1960)

$$A(\lambda) = \frac{\tau_A}{1 + \frac{4R}{(1-R)^2}\sin^2(\Pi P/\lambda)} \qquad (2.9)$$

where τ_A is the transmission coefficient which depends on the reflection and absorption coefficient of the coatings and is given by

$$\tau_A = (1 - \frac{A}{1-R})^2 \qquad (2.10)$$

The Airy function is illustrated in Figure 2. The peaks of this function occur at $\lambda = P/m$, where m, an integer, is the order of interference. When the reflection coefficient is close to unity then $4R/(1-R)^2$ in (2.9), becomes large and the transmitted intensity is very small except when $\lambda = P/m$. The interval between peaks of the Airy function, designated $\Delta\lambda$, is called the free spectral range,

$$\Delta\lambda = \lambda/m \qquad (2.11)$$

The finesse is defined as the ratio of the free spectral range to the width of the peak,

$$N_R = \frac{\Delta\lambda}{a} = \Pi\sqrt{R}/(1-R) \qquad (2.12)$$

and is called the reflective finesse because it depends only on the reflection coefficient of the coatings.

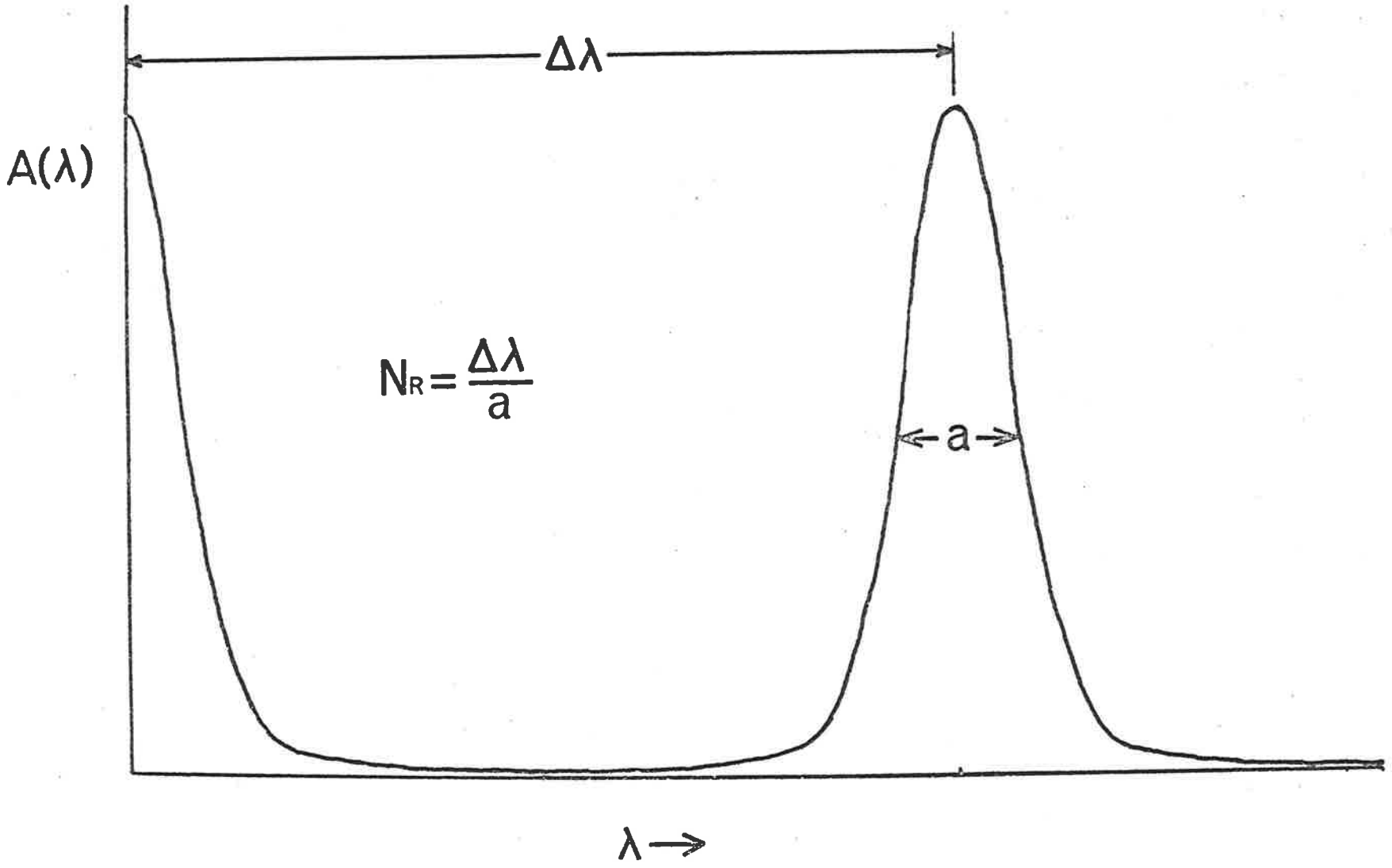

FIG. 2. The Airy Function, illustrating the reflective finesse, N_R.

2.3.2 Defect Functions

The discussion so far has been concerned with the so-called perfect étalon. The effects of non-uniformity of plate spacing and of finite aperture will now be considered. The approach is similar to that of Chabbal (1953), in which the effect of each defect on a perfect étalon is considered and the corresponding instrumental function determined. The overall instrumental function of a practical FPI is then obtained by convolution of these individual functions.

Chabbal (1953) discusses the two simplest forms of plate defects, which can be described by analytical functions. These are the spherical defect, which is described by a rectangular function and the surface roughness defect, described by a gaussian function. In the general case the defect function is of the form,

$$D(\lambda) = \frac{1}{\hat{S}} \frac{dS}{d\lambda} \qquad (2.13)$$

where $\hat{S}$ is the area of the FPI plates and $dS/\hat{S}$ is the fraction of the étalon area which has peak transmission in the interval $d\lambda$. If the width of this function is denoted by d then a defect finesse can be defined as,

$$N_D = \Delta\lambda/d \qquad (2.14)$$

by analogy to (2.12). This is an important quantity because it imposes an upper limit on the overall instrumental finesse and for this reason has been called the "limiting finesse".

2.3.3 Aperture Function

Assuming that the FPI has a perfect étalon and plate coatings with R = 1, the instrument function is solely due to the finite

aperture and is defined as,

$$F(\lambda) = \frac{1}{\hat{\Omega}} \frac{d\Omega}{d\lambda} \tag{2.15}$$

where $\hat{\Omega}$ is the total solid angle subtended by the instrument. The aperture finesse is defined as

$$N_f = \Delta\lambda/f \tag{2.16}$$

where f is the half-width of the aperture function.

2.3.4 Recorded Function

The function recorded by the FPI will now be synthesized by referring to Figure 3. Firstly the étalon function E, is determined by convolution of the Airy function and the defect function.

$$E(\lambda) = D * A \tag{2.17}$$

The instrument function I, is due to the convolution of the étalon and aperture functions,

$$I(\lambda) = F * E \tag{2.18}$$

If the spectral radiance of the source is $B(\lambda)$ and its total radiance $\hat{B}$, then the source function is defined as,

$$G(\lambda) = B(\lambda)/\hat{B} \tag{2.19}$$

If this source is presented to the FPI then the recorded function is,

$$\Phi(\lambda) = \hat{B}\hat{S}\hat{\Omega}G * I \tag{2.20}$$

Referring to Figure 3, the functions on the left (D, F, G) have all been normalised to unit area under the curve. The area within

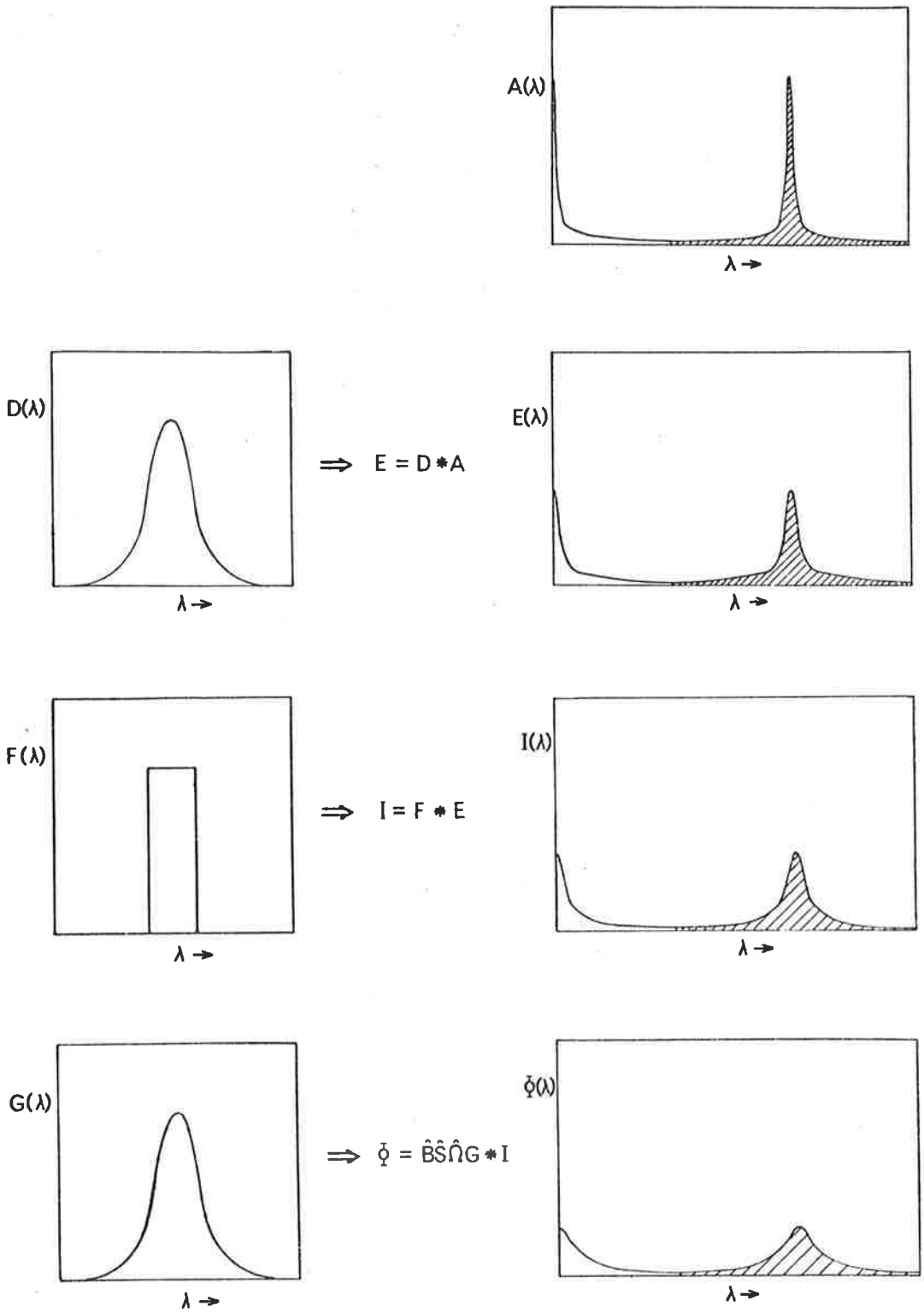

FIG. 3. Schematic diagram illustrating the various functions which are convolved together to produce the instrument recorded function.

the shaded section, under the Airy function is determined by the reflection coefficient of the plate coatings. The corresponding areas under functions E, I and Φ are the same because they result from convolution of the Airy function with the normalised functions D, A and G. The functions E, I and Φ become progressively broader and hence the peak transmission is reduced. The peak height of the function denoted $I(\lambda)$ is the overall peak transmission of the instrument, which will be further discussed in the next section.

2.4 Resolving Power and Light Gathering Power

The resolution of a FPI capable of just resolving two lines λ_0 and λ_1 may be defined as,

$$\delta\lambda = \lambda_0 - \lambda_1 = i \tag{2.21}$$

where i is the width at half maximum of the instrument function. The resolving power is defined as

$$R = \lambda/\delta\lambda = \lambda/i \tag{2.22}$$

The physical significance of the finesse now becomes apparent. The finesse represents the maximum number of spectral elements which can be resolved in one free spectral range.

The light gathering power of the instrument may be defined as,

$$L = \tau S\Omega \tag{2.23}$$

where τ is the overall transmission of the instrument. This term is the product of three factors

$$\tau = \tau_A \tau_D \tau_F \tag{2.24}$$

where τ_A is the peak amplitude of the Airy function, given by

(2.10). The factor τ_D is the peak amplitude of the defect function and expresses the reduction in transmission due to the convolution A * D. The factor τ_F is the peak amplitude of the aperture function and as above, expresses the reduction in transmission due to the convolution of A * D with F.

Chabbal has shown that the optimum luminosity is achieved when the widths of the three functions A, D and F are approximately equal. This condition also optimises the light gathering power X resolving power product, (Chabbal, 1953) given by,

$$LR = 2\Pi\tau S \qquad (2.25)$$

This relationship implies that in selecting the resolving power and light gathering power of the instrument, a compromise will need to be made. Details of the compromise in the case of the Mawson Institute FPI will be given in Chapter 6.

CHAPTER 3

DEVELOPMENT OF THE FABRY-PEROT INTERFEROMETER

3.1 Introduction

This chapter is devoted to the development of the Mawson Institute FPI for high resolution studies of the doppler widths and shifts of the atomic oxygen lines λ577.7nm and λ630nm, emitted by the upper atmosphere. The description of the instrument in its final form will be given in Chapter 4 and the developmental work on the detection of low light levels will be described in Chapter 5.

Constructional work on the FPI commenced in 1967 and progressed at a rate, such that when the author joined the project in 1969 a large amount of the mechanical construction had been completed. It was envisaged at this early stage that 12-18 months should be sufficient to design and build the electronics and to complete the final assembly and debugging. The large amount of debugging that would actually be required could not have been envisaged at that stage.

3.2 Piezoelectric Stacks

The servo system for maintaining the FPI plates parallel necessitates the use of piezoelectric supports for both plates. The lower plate is supported on three piezoelectric supports consisting of ten annular discs of PZT5H, manufactured by Brush Clevite Co. Ltd. The discs have an inner diameter of 9mm, an outer diameter of 20mm, a thickness of 2mm and are of lead zirconate-lead titanate composition. The upper FPI plate is suspended on three stacks each consisting of two such discs. The electrodes are berylium-copper washers which are cemented between alternate piezoelectric discs by

electrically conductive adhesive. The construction is illustrated in Figure 20. To strengthen the assembly a bolt is passed through the centre of the stack to couple together the brass couplings on the ends. Finally, the stack is encased with an insulating layer of epoxy-resin. Electrical connections are made by soldering directly onto the berylium-copper washers, taking care not to over heat the piezoelectric discs.

The PZT5H composition was chosen because of its large piezo-electric coefficient, which for a stack of ten discs was measured to be approximately 4.5nm/volt. This meant that a power supply capable of delivering 600 volts would produce the desired displacement and the risk of electrical "flash-over" was small.

The displacement characteristics of the ten disc stacks were measured with a Hewlett Packard linear displacement transducer Model 24DCDT-100. This has a built in carrier oscillator and demodulator which produces a DC output voltage proportional to the linear displacement of the core. The manufacturer quotes a coefficient of 4mV/μm and claims that the transducer has linearity error less than 0.5 percent of full scale and zero hysteresis.

The results obtained were later verified by measurements with a capacitor transducer, which will be described in Chapter 4. The non-linearity and creep behaviour observed is therefore, a property of the piezoelectric stack and not the displacement transducer. The displacement-voltage characteristic is shown in Figure 4, and shows evidence of gross non-linearity and hysteresis. A further undesirable property of the piezoelectric material was also discovered, which will be called "creep". After the application of a voltage

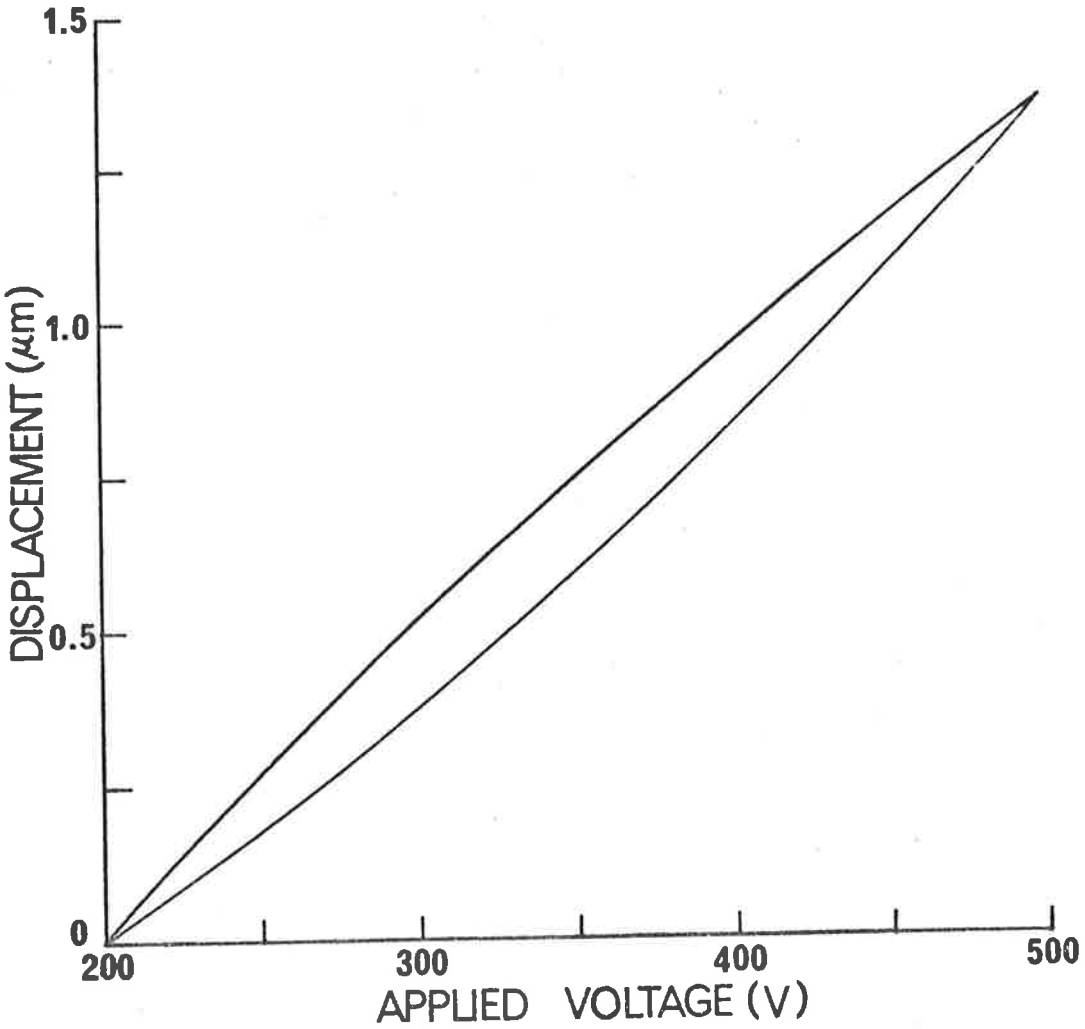

FIG. 4. Displacement as a function of applied voltage for a 10 disc PZT5H piezoelectric stack. The average piezoelectric coefficient is 4.5nm/volt.

step to the stack, the resultant displacement would be partially achieved instantaneously; however, further movement amounting to approximately 10 percent of the full displacement would continue for some tens of seconds before a near to final displacement was reached.

Pre-polarization of the discs was carried out by the manufacturer and it was felt that this may not have been carried out properly. Ramsay and Mugridge (1962) have reported that pre-polarization by applying an electric field to the discs at a temperature greater than the Curie point (193°C) and then allowing them to cool with the field applied, significantly reduces hysteresis. Pre-polarization of a stack of four discs was carried out in this fashion and was found to have no effect on the hysteresis or creep.

Since no solution to the non-linear movement of the plate supports could be found it was concluded that dynamic stabilisation of the FPI plate separation would be essential.

More recent tests carried out by T. Cocks have revealed that both the composition and configuration of the piezoelectric material play a part in determining its linearity characteristics. A near linear response with almost zero hysteresis has been achieved with PZT4 material constructed in a tube configuration.

3.3 Parallelism Control

The principles of the automatic parallelism control system for the FPI were developed within the C.S.I.R.O. division of Physics by Ramsay (1968). A full description of this system will be given in the next chapter and only details relevant to the developmental problems will be given at this stage.

3.3.1 Tests on Original Design

Three silica lugs were cemented at 120° intervals onto the periphery of each FPI plate. The upper plate was supported by its lugs in a bronze ring, which was suspended from the roof of the étalon chamber by three piezoelectric stacks, each of two discs. In the original design, the orientation of the support lugs were offset by 30° relative to the piezoelectric stacks. This support system proved to be unsatisfactory.

The control system requires that the uppoer plate be oscillated about its centre, which is achieved by applying a sine wave drive to each of the stacks supporting it. The phase of the drive applied to each support is 120° in advance of that applied to the previous one. This produces a travelling wave on the edge of the plate while the centre of the plate remains stationary. The oscillation of the plate should be such that the phase difference between diametrically opposite points is 180 degrees.

In early 1970, the FPI was assembled for the first time in order to assess the performance of the parallelism control. It soon became apparent that the mode of oscillation of the ring and FPI plate was nothing like what was expected. Extensive studies were made of the behaviour at different frequencies of oscillation, using a strain gauge displacement transducer. Frequencies in the range from 1 kHz to 10 kHz were tried, none of which were found to be entirely satisfactory. The particular design configuration and the materials used gave rise to quite complex resonant behaviour in this frequency range. Since no suitable drive frequency could be found it was decided to modify the design.

3.3.2 Design Modifications

The material chosen for the metal-work of the FPI was a special stress-relieved bronze, of excellent mechanical stability. It was suggested that this material may be partly responsible for the resonant behaviour and that a high carbon meehanite would be more suitable for use in the frequency range of 1 to 10 kHz. Consequently the FPI plate support rings and the lens-cell were reconstructed using meehanite. The original and the modified design are both shown in Figure 5. The bronze lens cell from which the étalon chamber was supported, was replaced with a meehanite cell and an annular ring of meehanite was mounted on top of the upper bronze plate. The plate support rings were redesigned so that the piezoelectric stacks and the plate support lugs were on the same axes, rather than being displaced by 30°, as in the original design. Many holes were drilled in the rings to reduce the weight and also to discourage the formation of standing waves around the rings.

The oscillatory behaviour was found to be much better with these modifications and the choice of a suitable operating frequency, near 4 kHZ was quite straight forward.

3.4 Separation Control

The early investigations on the behaviour of the piezoelectric supports which revealed non-linearity and creep meant that a dynamic servo system would need to be developed to control the spacing of the FPI plates.

The requirements on the displacement transducer would be a resolution better than 1nm, with a bandwidth of 10 Hz. The long term drift should also be within this limit over a period of several hours.

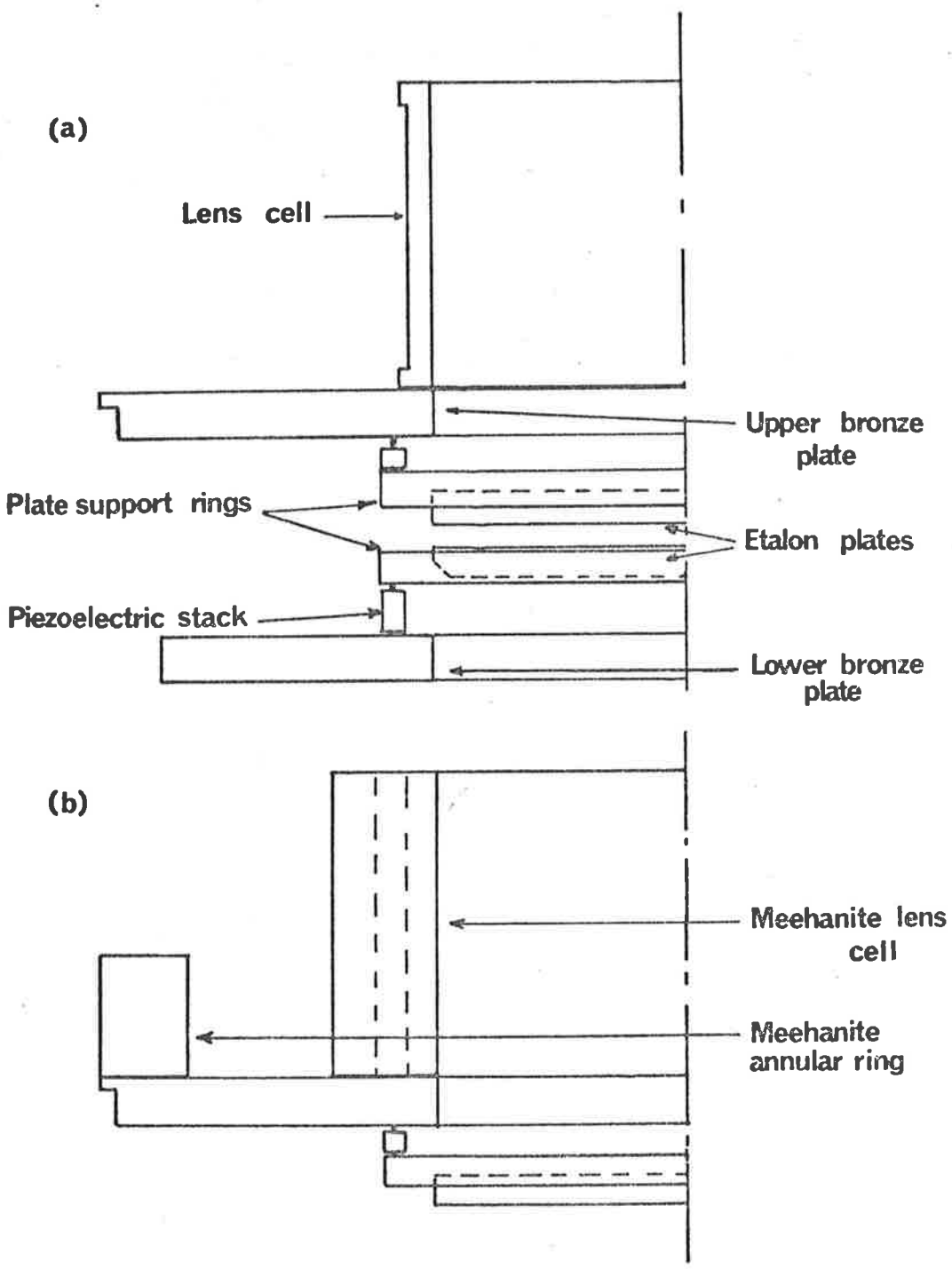

FIG. 5. Illustration of the changes made to the FPI; (a) original design, (b) modified design.

3.4.1 Differential Transformer Displacement Transducer

It was thought that the Hewlett Packard 24DCDT-100 displacement transducer would probably meet these specifications if it were placed in a temperature controlled environment. Unfortunately the transducer itself dissipated 900mW which made the maintenance of high temperature stability a very difficult exercise. This inherent heat dissipation also meant that long periods of time were involved before thermal equilibrium was reached. Tests on the long term stability of the transducer indicated that it would probably meet the required specification in this regard.

The resolution of the transducer with a bandwidth of 10 Hz was, however, only about 10nm, due to noise inherent in the device. The "unlimited resolution" claimed in the data sheet was only obtainable with intolerably narrow frequency response.

The work carried out on this displacement transducer was not wasted however, because it was later found to be suitable for use in a pressure transducer for monitoring atmospheric pressure.

3.4.2 Capacitance Transducer

After discovering that no suitable transducer was commercially available it was decided to proceed with the construction of one within the Mawson Institute. The capacitance transducer appeared to be the most promising, despite the fact that little in the way of published results appeared to exist. An exception to this was the work of Thompson (1958) and more recently a comprehensive review has been published by Jones and Richards (1973).

The simplest form of capacitance transducer consists of a pair of parallel plates. The capacitance of this system is directly

proportional to the area of the plates and inversely proportional to the separation between the plates. One plate is made smaller in area than the other so that only change in separation will strongly affect the capacitance and other relative movement will be unimportant.

A more elaborate design is shown in Figure 21 and consists of five plates. Plates 1, 3 and 5 are fixed in position, while plates 2 and 4 which are coupled together, are displaced. This configuration was chosen because of its greater output and lower temperature dependence. The symmetry of the design ensures that a temperature change will affect each inter-plate capacitance by the same amount and so the output will not change.

The electrical equivalent circuit for the five plate transducer is shown in Figure 21. Electrical connection is made to the plates so that the circuit is of a bridge configuration. The designation C_{12} refers to capacitance between plates 1 and 2. The AC drive voltage applied to the transducer was provided by a Hewlett Packard 3300 function generator. The frequency chosen was 10 kHZ and the amplitude 2 volts peak-to-peak.

The first prototype was constructed from stainless steel and used neoprene 'O'-rings as the flexible elements separating the plates. The choice of neoprene proved unfortunate because the response was unacceptably non-linear. The non-linear behaviour was eventually attributed to the neoprene spacers and so the transducer was redesigned using phosphor-bronze leaf springs as the flexible spacers.

The transducer was calibrated and tested using the interferometer, by coupling it onto the lower FPI plate support ring. Variations in plate spacing are transmitted to the transducer by an irvar rod which is coupled to the upper support ring. Using the 10 disc piezoelectric stacks which support the lower plate it is possible to scan over approximately 12 orders of interference at λ546nm. The output from the transducer was noted corresponding to successive mercury green line peaks transmitted by the FPI. The measurements revealed no detectable departures from linearity that could be attributed to the transducer. The maximum likely error in setting on the peak and in the electronics was 0.5% of full scale. The resolution of the transducer was much better than 1nm and in this application was actually limited by the electronics. The long term stability, however, was somewhat marginal and only met the specifcation when well temperature controlled. This was partly due to the thermal expansion of the invar rod and the other metal components in the coupling system between the transducer and the étalon, which is illustrated in Figure 20. This effect can be compensated for by altering the clamp position relative to the rod as explained in Chapter 4. The transducer is well thermally isolated from outside temperature changes and so exhibits a long response time to such effects. A more serious temperature dependence arose due to warping of the bronze plate from which the upper FPI plate is supported. This warping was transmitted via the piezoelectric stacks to the coupling system between transducer and étalon. Since the upper bronze plate forms the top of the étalon chamber and so is in contact with the outside air; this effect has a short response time to outside temperature variation. The difference in response time is apparent from the graph shown in Figure 6. A 1°C change was made

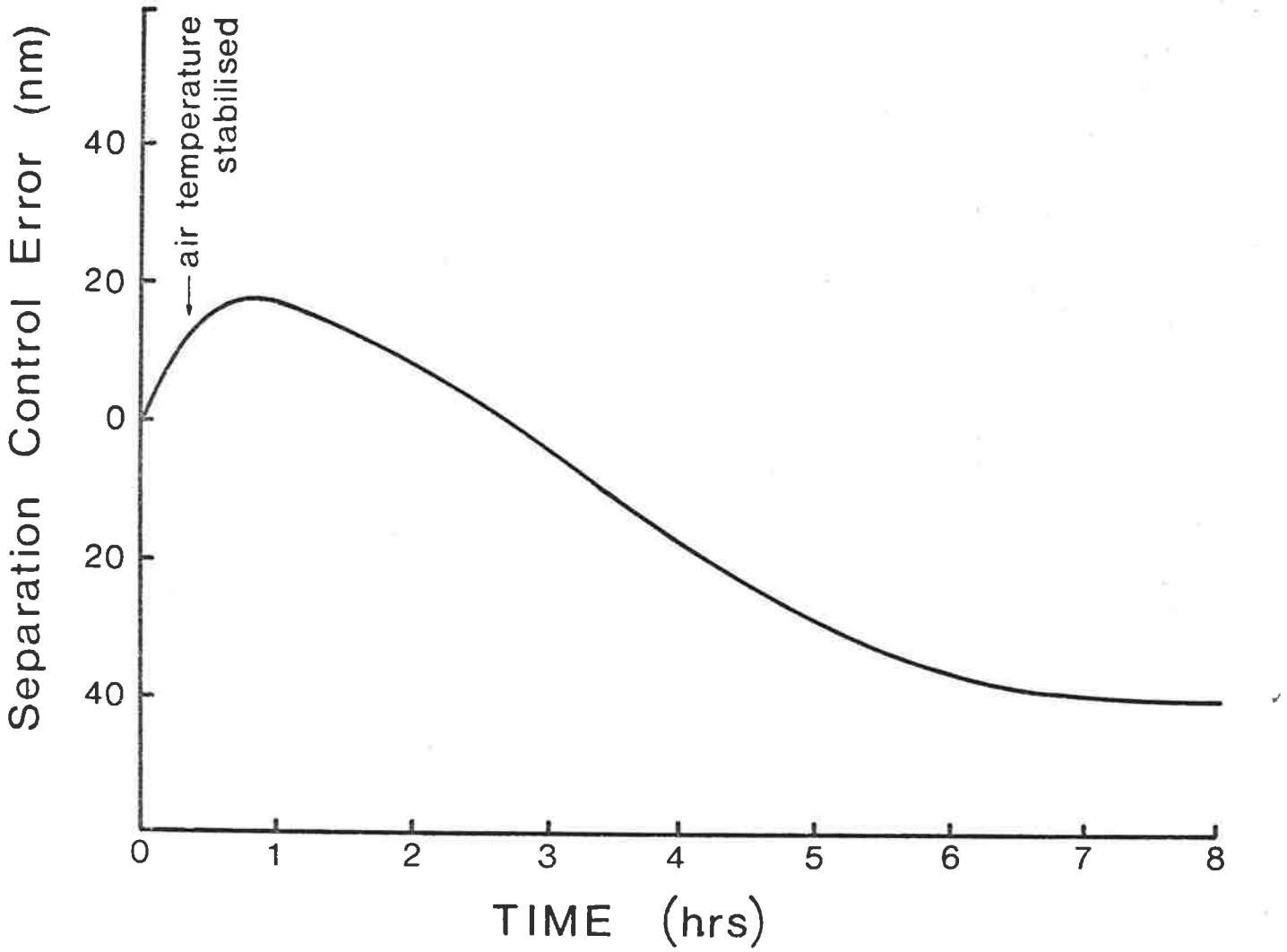

FIG. 6. Separation control error as a function of time after a 1°C change in air temperature.

to the air temperature setting and the separation error plotted as a function of time. The error due to warping occurs almost instantaneously, while thermal expansion in the coupling system only becomes the dominant effect after one hour has elapsed. It became clear that temperature control to within 0.01°C would be essential for the transducer to meet the requirement on long term stability.

3.5 Temperature Control

3.5.1 Air Temperature Control

The FPI is enclosed in a three-sided box approximately two metres in height and with sides 0.73 metres wide. It was intended that the air in this box would be controlled to within 0.1°C using a mercury in steel capillary thermostat. The air is drawn past heaters mounted in vertical ducts by paddle-wheel type fans mounted at the bottom of the ducts. The two ducts were approximately 1.8 metres in height and have air intakes at the top. The thermostat was mounted so that the sensing bulb was at the same level as the étalon. The temperature variations in the air were monitored using a thermistor.

It was found that the temperature fluctuations were 0.1°C in amplitude but were of such a long period (15 minutes) that the capcitance transducer was affected. Separation control errors of $\pm$ 2nm were observed with the same periodicity as the temperature fluctuations.

A heater was wound on the aluminium étalon chamber cover (designated barrel heater) in an attempt to reduce the dependence on air temperature fluctuations. A thermistor embedded in the wall of the barrel was used to control the temperature. The electrical

mains supply (240V AC) was used to power the heater and it was controlled by a triac switch. The triac switch was operated in the phase control mode which enabled proportional control over a small temperature range about the set-point. This type of electronics emits a large amount of radio-frequency noise, which was found to interfere with the low level circuitry used in association with the capacitance transducer. It was replaced by a system which switches the power only when the AC voltage is near zero-crossing. The electronics with the zero-crossing control will be fully described in the Appendix. Use of the barrel heater reduced the perturbations in the transducer, but not sufficiently to be acceptable and so the mercury in steel thermostat was replaced by a thermistor and zero-crossing system.

The air temperature fluctuations were not significantly reduced in amplitude, but the period was reduced considerably. The addition of a third paddle-wheel fan positioned between the output of the two ducts and with its output directed towards the top of the FPI enclosure, further reduced the period of the fluctuations. Another factor which was responsible for this improvement was the use of "rate-feedback". This means that the current delivered to the heater is proportional not only to the error in temperature, but also to the rate at which the set-point is being approached. A correction of this type reduced the over-shoot due to the poor coupling between heater and thermistor. With all these refinements the period of the air temperature fluctuations was reduced to two minutes while the amplitude was slightly less than 0.1°C. The schematic diagram in Figure 7 illustrates the positioning of the heaters and thermistors described above.

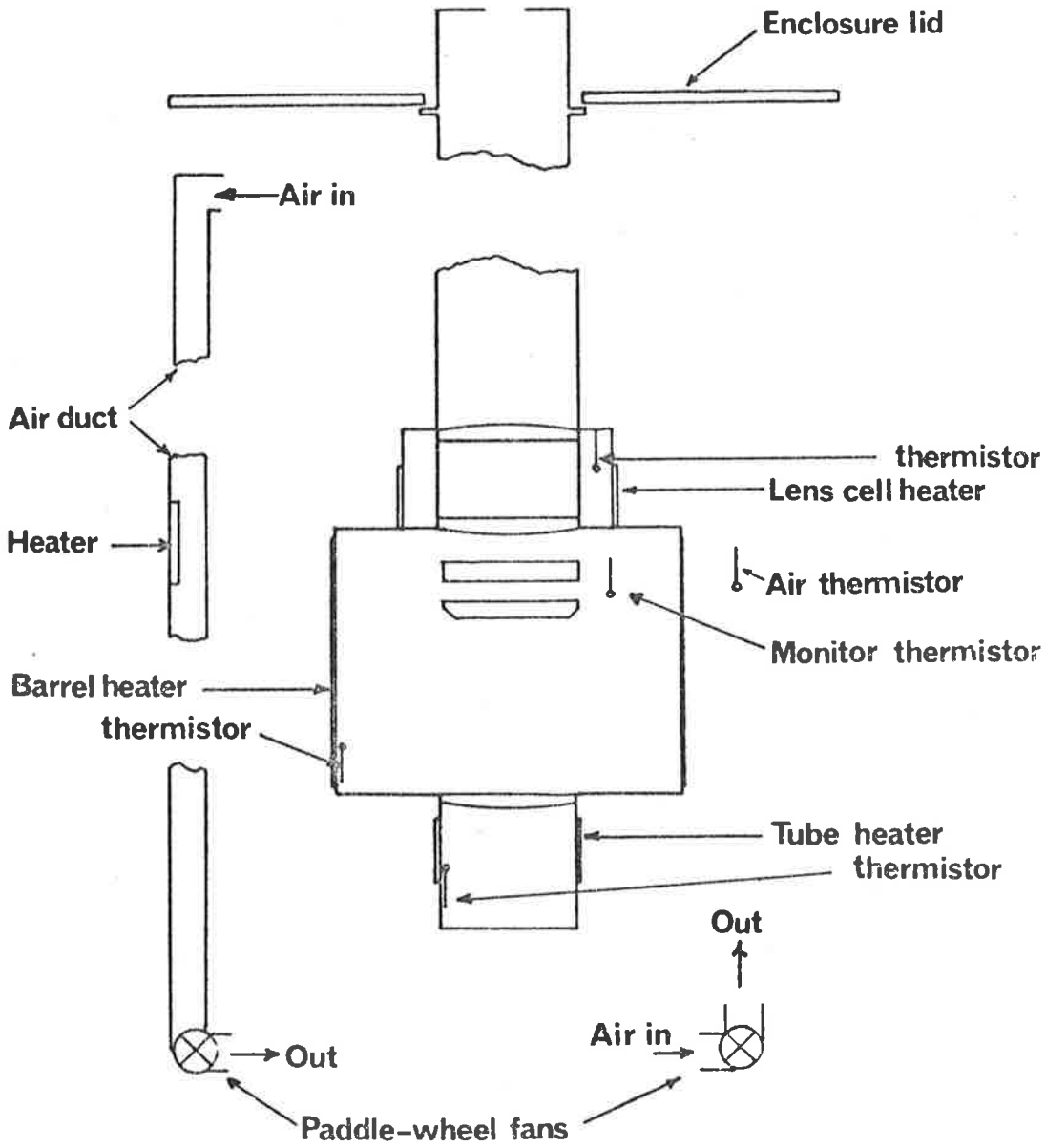

FIG. 7. Schematic diagram illustrating the temperature control system used in the Mawson Institute FPI.

3.5.2 Ancillary Heaters

In addition to the duct and barrel heaters two further heater and thermistor combinations are shown in Figure 7. The first of these consists of a heater wound on the meehanite lens cell and a thermistor embedded into the top of the cell. This was found to be necessary because temperature changes outside the box were transmitted down the metal-work of the FPI and hence perturbed the transducer. It was also felt that a heater should be provided to isolate the étalon chamber from the refrigerated photomultiplier chamber. Hence the so-called tube heater and thermistor were incorporated into the FPI, but were later found to be unnecessary.

Exhaustive tests on the thermal stability of the interferometer were carried out over a period of months and continued after the installation at Mount Torrens. A thermistor was mounted inside the étalon chamber to monitor the air temperature near the FPI plates. Temperature fluctuations in this region were typically less than 0.002°C over a 24 hour period.

3.6 Installation at Mount Torrens

The developmental work on the capacitance transducer and the temperature control was considered to be completed at the end of 1971 and so the final refining of the instrument was then commenced. The first step was to chemically blacken all the internal parts of the interferometer to reduce light scattering. The outside of the FPI was cadmium plated in an attempt to increase the thermal isolation of the instrument. The FPI was completely assembled once more in the laboratory for final tests before moving it into the field.

In June 1972, the move was made to the Mount Torrens field station, which is about 30 miles East of Adelaide. It was found

that the temperature variations in the field station were so large that it was necessary to run an air-conditioner continuously to prevent disturbing the FPI temperature control.

A telemetry link between Mount Torrens and the University of Adelaide had been in operation for several years to enable transmission of the measurements of the earth's magnetic field made with a flux-gate magnetometer, sited near the field station. The 15 watt, 160 MHz transmitter and associated yagi antenna were found to interfere with the low level circuitry used in the FPI. The transmitter and antenna had to be repositioned, well away from the station, before this interference could be sufficiently reduced.

The most serious problem encountered after field installation was the suppression of background light emitted by the parallelism control lamps which was reaching the photomultiplier tube; despite the use of a series of masks. The addition of an aperture at the focal plane of the output lens considerably reduced the background light, however, optical filtering of the lamps was needed to completely remove it. The spectral response of the hp 5082-4200 series pin photodiode, which was used as detector in the parallelism control, is shown in Figure 8(a). The peak of the response occurs in the near infra-red, whilst in this region the photomultiplier with S-20 photocathode has little or no response. A Wratten 87C filter (see Figure 8(b)) was incorporated in the lamp housing to block emission below a wavelength of 800nm and so reduced the background from this source to negligible proportions.

Airglow observations were commenced in July 1972 and continued until October, 1973. During this period more refinements were

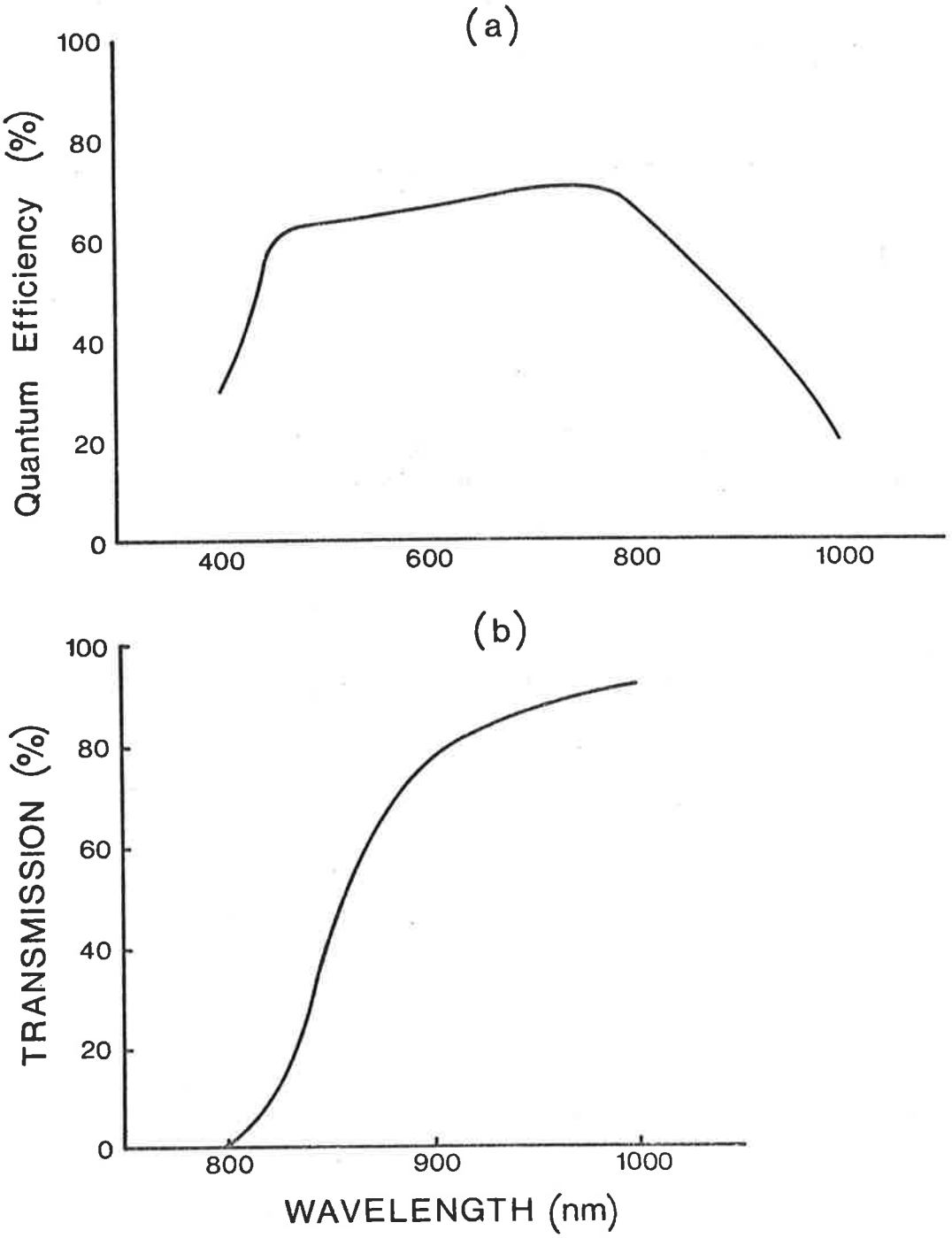

FIG. 8. Spectral responses of (a) the hp. PIN photodiode and (b) the Wratten 87C infrared filter.

made to the FPI detection system which will be fully described in Chapter 5.

CHAPTER 4

THE MAWSON INSTITUTE FPI

In this chapter the FPI constructed in the Mawson Institute for Antarctic research will be described in its final form. A description will be given in Chapter 6, of the operational procedure for collecting results, the analysis of these results and the technique for calibrating the FPI.

4.1 Optical and Mechanical Design

4.1.1 Optical Design and Adjustment

The optical design of the FPI is illustrated by the schematic diagram in Figure 9. The light is introduced into the interferometer by a periscope consisting of two back-silvered mirrors. The upper mirror can be rotated about a horizontal axis to achieve variation of the zenith angle of viewing and the whole periscope can be rotated about a vertical axis to vary azimuth angle. The periscope is followed by the narrow-band interference filter; which could be one of the three whose characteristics are given in Table 1. The parameter λ_0 is the wavelength for peak transmission at normal incidence and at a temperature of 30°C; and T the percentage of the incidence light which is transmitted at that wavelength.

The next component is a 150mm, f/6 lens, at the focus of which is the field step. This arrangement of the input optics ensures that the light passing through the interference filter is near-parallel.

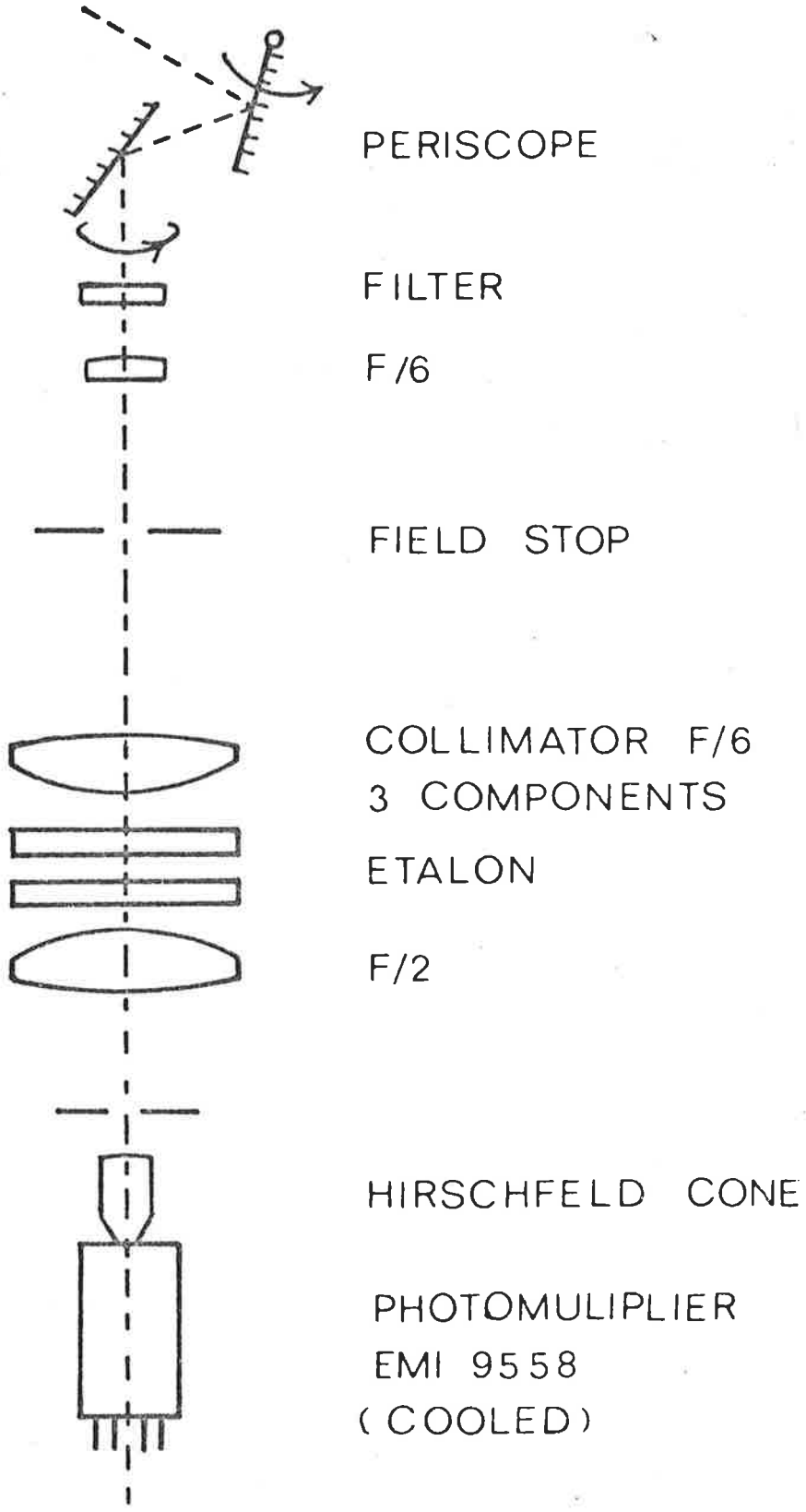

FIG. 9. Schematic diagram of the interferometer optical system.

TABLE 1

INTERFERENCE FILTER CHARACTERISTICS

	λ_0	T(percent)	Bandwidth (nm)
RED I	630.0	62	0.85
RED II	630.0	47	0.38
GREEN	557.7	40	0.8

The field stop is accurately positioned at the focus of the collimator, which is a three component 900mm, f/6 lens. The étalon is next, followed by a single component 300mm, f/2 lens, at the focus of which is an aperture with diameter just large enough to not limit the field of view of the FPI.

The final optical component is the Hirschfeld cone, which introduces the light into the window of the photomultiplier tube so that multiple reflections occur within its front window. This device will be fully described in the next chapter.

The alignment of the optics proved to be quite straight forward as the only critical adjustments are the FPI plate spacing and parallelism and the alignment of the field stop and collimating lens. The latter alignment is achieved by auto-collimation using the mirror surface of the top FPI plate. The field stop is replaced by a glass window with a graticule of fine concentric circles engraved on it. The holder for the field stop (or graticule) can be moved up or down relative to the collimator lens to provide focusing and the upper étalon plate can be slightly tilted to align the field stop with the optic axis. With the graticule in position, focusing

adjustment is made until no parallax can be observed between the graticule and its reflected image. The upper plate is then tilted until the graticule and its reflected image are coincident. Fine movement of the FPI plates is achieved by use of the differential screws from which the piezoelectric supports are mounted. The construction of the fine movement control is illustrated in Figure 21. Rotation of the fine-adjust nut only achieves a movement given by the difference between threads I and II which are 15 and 16 per cm respectively. The FPI plates are supported from this type of fine movement control which enables adjustment of parallelism to within 10nm. These small errors can be accounted for by application of the appropriate voltages to the piezoelectric stacks, either manually or automatically by the parallelism control servo.

The lower FPI plate is supported from a large bronze disc which in turn is supported on three steel screws 25mm in diameter and approximately 350mm long. These screws have a very fine thread of 20 turns per cm so that simultaneous rotation of all three provides movement of the lower étalon plate relative to the upper. The drive for this movement is provided by an electric motor via a gear system of very high reduction ratio. Movement of the bronze support plate and hence the lower étalon plate can be measured to the nearest 0.01mm by a micrometer coupled to the disc by a push rod. Very fine plate separation adjustments including the scanning of the spectrum are made by use of the ten disc piezoelectric stacks and measured using the capacitance displacement transducer.

4.1.2 Mechanical Details

The details of the mechanical design of the FPI have been or

will be presented within the sections of the thesis to which they directly relate. Hence, the description given here is in the form of a general description of the instrument, including some fine details which have not been mentioned elsewhere.

The interferometer is housed in a large temperature controlled box from which it is supported by a number of steel springs. This form of support is used in order to improve isolation from vibrations. The upper-most unit which houses the periscope mirrors is mounted on the roof of the box, independent from the main body-work of the FPI. This unit also contains an 80 watt heater, a fan and a thermostat. The heated air is blown over the mirrors to prevent water condensation and also over the interference filter, which is usually maintained at approximately 30°C. The periscope unit has a small hatch in its side to permit the changing of interference filters and the adjustment of the thermostat. The light from the mercury isotope lamp, which is used for calibration purposes, is also introduced into the FPI by passing a light-pipe through the periscope hatch.

4.2 The Plates

The fused silica plates which make up the étalon are obviously the most critical optical component of the FPI. They were made by Mr. John Cole, now of Cole Precision Optics, Adelaide and were delivered in May 1969. The original specifications for these plates were 150mm diameter and 25mm thick with a flatness of $\lambda/80$ at 546nm over the central 145mm diameter. At this stage no technique had been developed adequately to measure the flatness of the plates without coatings. The initial coatings which were applied by Mr. J. Ward of Weapons Research Establishment, Salisbury were of silver

and dielectric composition. The reflective finesse at λ630nm was 100 which enabled accurate studies to be made of the plate defects. It was found that the defect finesse was only 20 which indicated that the plates had not met their original flatness specification. Some of the defects could be attributed to non-uniformity of the coatings causing variations in the phase change at reflection over the coating surface (Ramsay, 1968). In late 1971 when the final stages of development were being carried out, it was decided to make an attempt to improve the quality of the plates.

4.2.1 Testing for Flatness

The simplest method of testing for flatness is to apply a high reflectance coating such as silver or aluminium, with sufficient uniformity that the plate defects are the major factor in determining the defect finesse. This method was rejected however, because it would have proved too time consuming and so a technique for testing uncoated plates was developed.

The graphs in Figure 10 illustrate the transmission of the FPI as function of frequency with and without coatings. It is clear that the fringe pattern in (a) (coated plates) will have greatest contrast in transmission, while in (b) (uncoated plates) the contrast is much better in the reflected fringe pattern. The reflected pattern is approximately the complement of the transmitted pattern for low absorption and so consists of dark fringes on a light background.

The experimental arrangement for viewing the reflected fringe pattern is illustrated in Figure 11. The light source needs to be very bright and so a He-Ne laser is used. The laser is followed by a lens to spread the beam and so illuminate the whole étalon

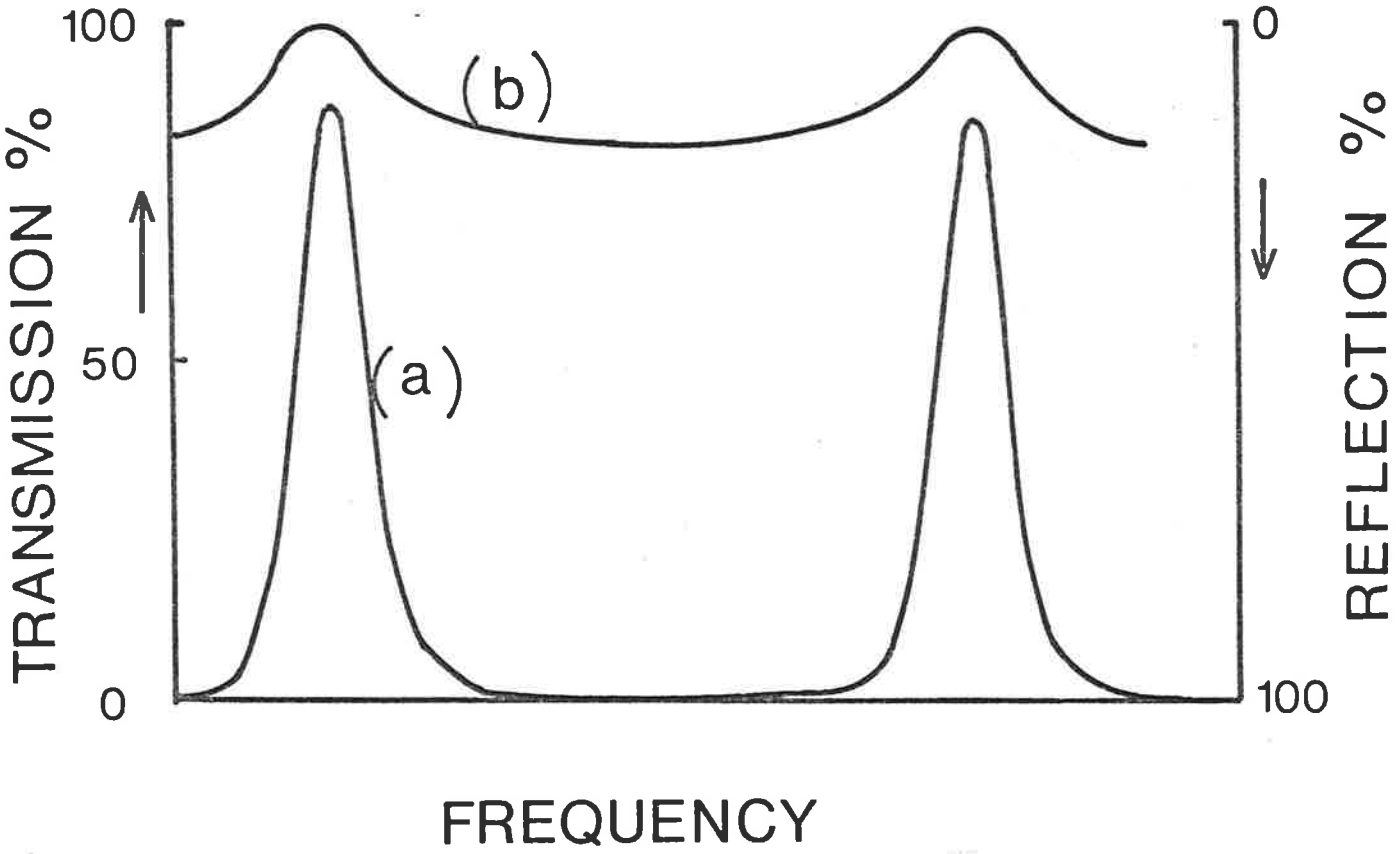

FIG. 10. FPI transmission as a function of frequency for (a) high reflectance coatings (reflectance = 0.9 and absorption = 0.01) and (b) no coatings (reflectance = 0.04 and absorption = 0).

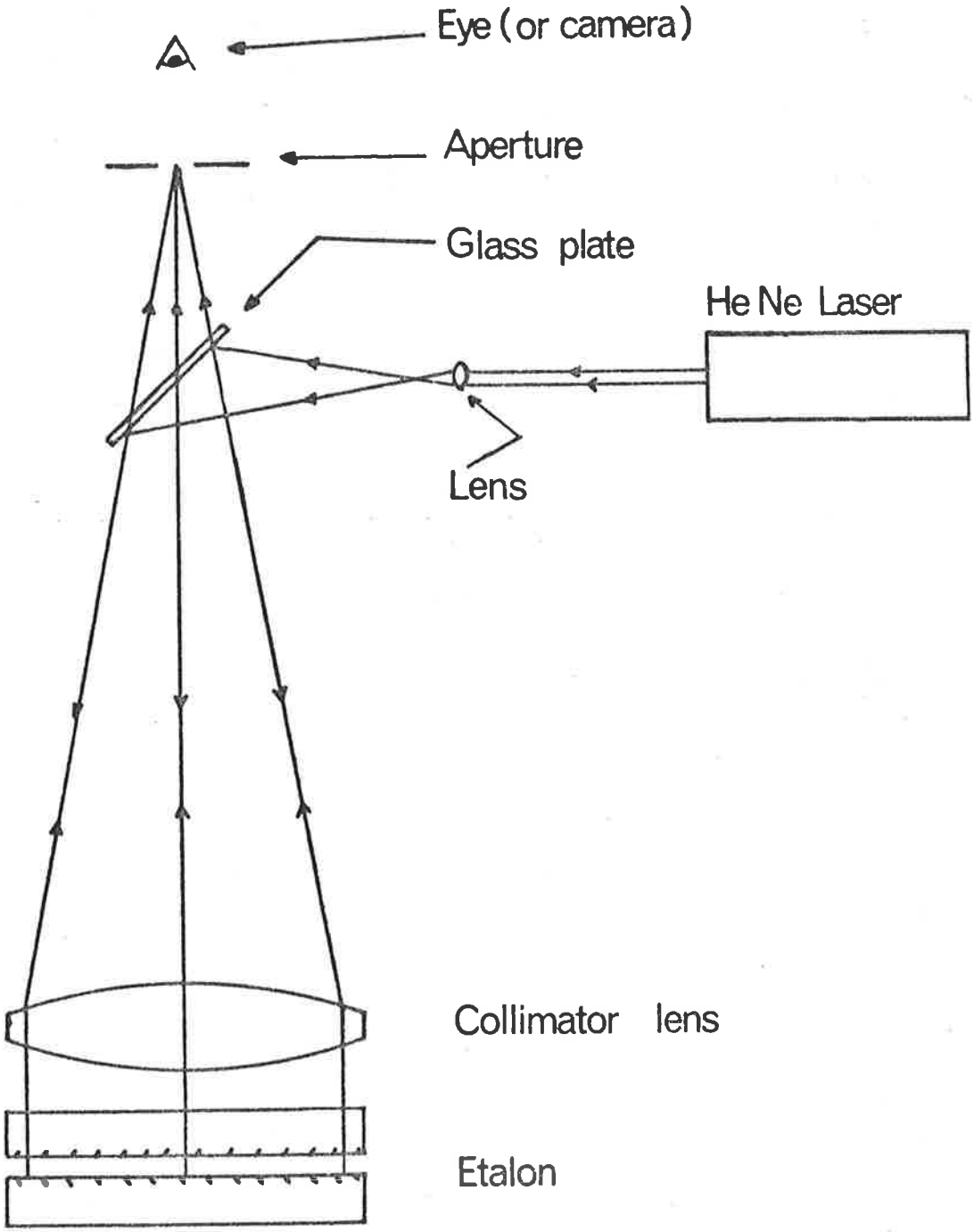

FIG. 11. Illustration of the experimental arrangement for viewing interference fringes in reflected light from the FPI. This arrangement was used for assessing the flatness of the plates prior to application of the high reflectance coatings.

aperture. A glass plate at 45° to the input beam is used to reflect a fraction of this beam to the étalon under test. The reflected fringe pattern is viewed through an aperture directly above the glass plate. The pattern can be viewed by eye or recorded on film by positioning a camera above the aperture. The interference fringes observed are Fizean fringes; sometimes called fringes of equal thickness. A number of examples of such fringes are shown in Figure 12, for the plates near parallel. In each case the air film between the plates is wedge-shaped and the axis of this wedge is varied to investigate the full aperture of the plates. For perfectly flat plates the fringes would be straight and parallel to one another. Any distortion in the fringes is due to a plate irregularity and indicates that more polishing is required. The edge-off effect is quite apparent in Figure 12 and other defects are also apparent in the central area of the plates.

Each time the plates were re-polished a new set of photographs was taken in order to assess the quality of the plate surfaces. The optical technician, Mr. J. Cole who was polishing the plates would then use the photographs as a guide for re-working the plates. This procedure was repeated until it was thought that the plates had reached the desired flatness.

A second method of assessing the plate flatness, using the same apparatus, was also devised. With the plates parallel and the étalon spacing so small that the source line width is insignificant the laser line is scanned in small steps by varying the voltages applied to the piezoelectric stacks. A photograph is taken each time the plate separation has been varied by 1nm. Two such photographs are shown in Figure 13. A set of photographs of this type

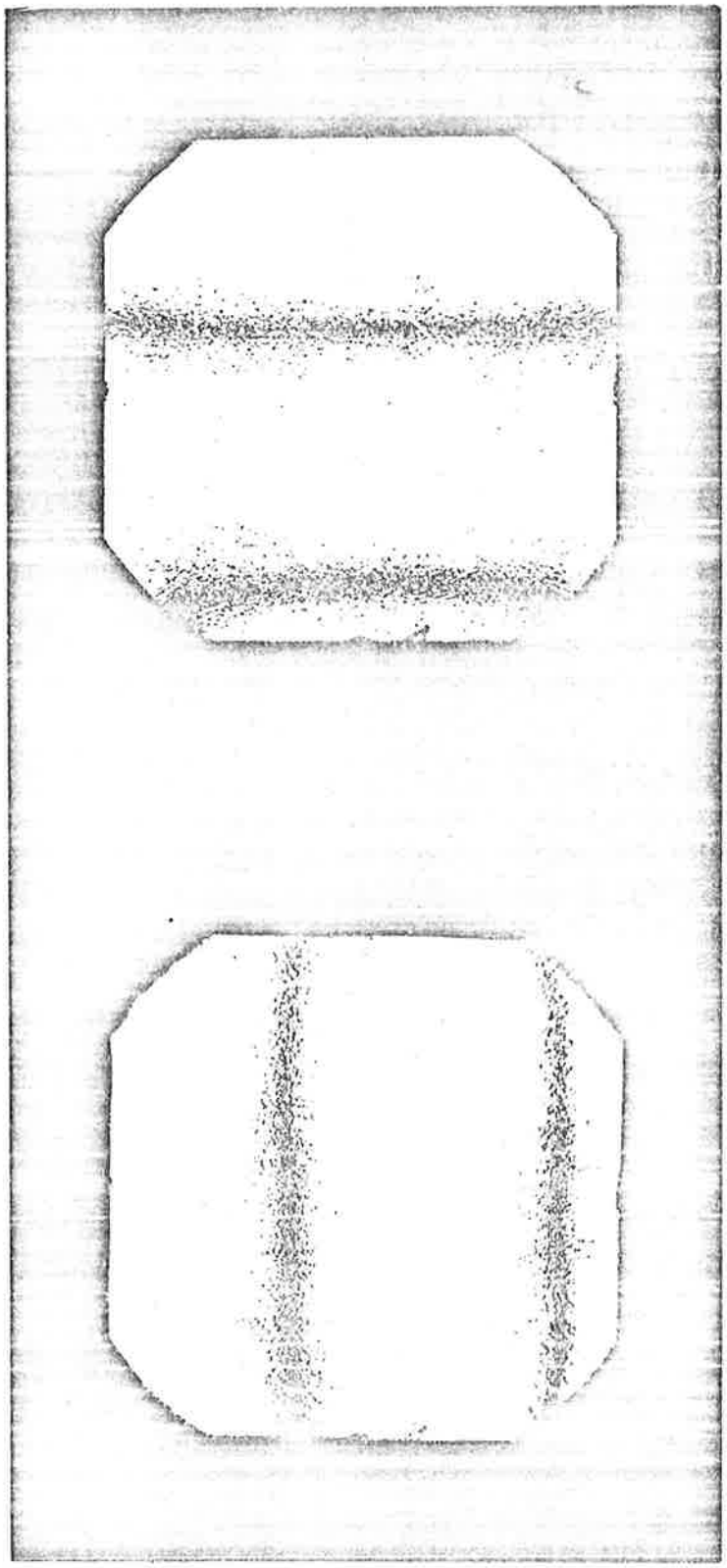

FIG. 12. Fizeau fringes photographed when the FPI plates are tilted slightly relative to one another. The edge-off effect and other distortions are apparent inthe two examples shown.

FIG. 13. Fizeau fringes photographed when the FPI plates are parallel to one another. The two photographs shown were taken at plate spacings differing by approximately 1nm.

can be used to construct a contour diagram of the plate irregularities, similar to those presented by Chabbal (1958). The final estimate of the plate flatness was $\lambda/60$ at λ546nm which implies a defect finesse, N_D of approximately 30.

4.2.2 Coatings

The coatings proposed for use in the FPI consisted of a layer of evaporated silver overcoated with a layer of magnesium fluoride and a layer of cerium oxide. The silver layer provides the high reflection coefficient while the dielectric layers apart from determining the spectral response also protect the silver from deterioration caused by exposure to air. This protection of the silver is so good that no noticeable deterioration has been observed after two years. The characteristics of the four coatings, from which a choice was to be made, are given in Table 2.

TABLE 2

CHARACTERISTICS OF COATINGS PROPOSED FOR USE ON MAWSON INSTITUTE FPI

Coating	Ag Layer (nm)	MgF_2 Layer $\lambda/4$ at(nm)	CeO_2 Layer $\lambda/4$ at(nm)	λ630nm R(%)	T(%)	A(%)
I	40	356	500	96.9	2.2	0.9
II	40	458	594	97.8	1.6	0.6
III	30	458	594	95.7	3.6	0.7
IV	30	356	500	93.9	5.1	1.0

The thickness of the silver, magnesium fluoride and cerium oxide layers is given and the percentage reflection, transmission and

absorption at λ630nm. The reflective finesse and the peak transmission as a function of wavelength are given in Figure 14. It was felt that this type of coating had a number of advantages over the more conventional multi-dielectric coating, recommended by Jacquinot (1960). Referring to Figure 14 it is clear that the coating designated IV has comparable peak transmission and finesse to the dielectric coating consisting of seven alternate layers of zinc sulphide and cryolite. The dielectric coating is only useful over a spectral range of approximately 50nm, while the coating IV has a finesse of greater than 30 and a peak transmission greater than 0.6 over a spectral range of 300nm. This means that the metal coatings will provide for a more versatile instrument capable of studies at any wavelength from 450nm to beyond 800nm. The wide wavelength range of transmission is also required for the operation of the automatic parallelism control, which is described in 4.3. The other advantage of the metal-dielectric coating over the dielectric coating is that the former requires the deposition of only three layers and so is simpler to achieve than the latter which requires seven layers for comparable performance.

From the work on testing plate flatness it was estimated that the defect finesse was 30 and so using Chabbal's criterion that the reflective finesse $N_R = N_D$, the coatings designated IV are obviously the most suitable. These coatings were applied and have $N_R = 50$ and $\tau = 0.7$ at a wavelength of 630nm.

The defect finesse of the étalon is now quite straight forward to measure, using the FPI in its conventional form as shown in Figure 9. The field stop used was 1mm which is sufficiently small so that the aperture function's contribution to the instrumental

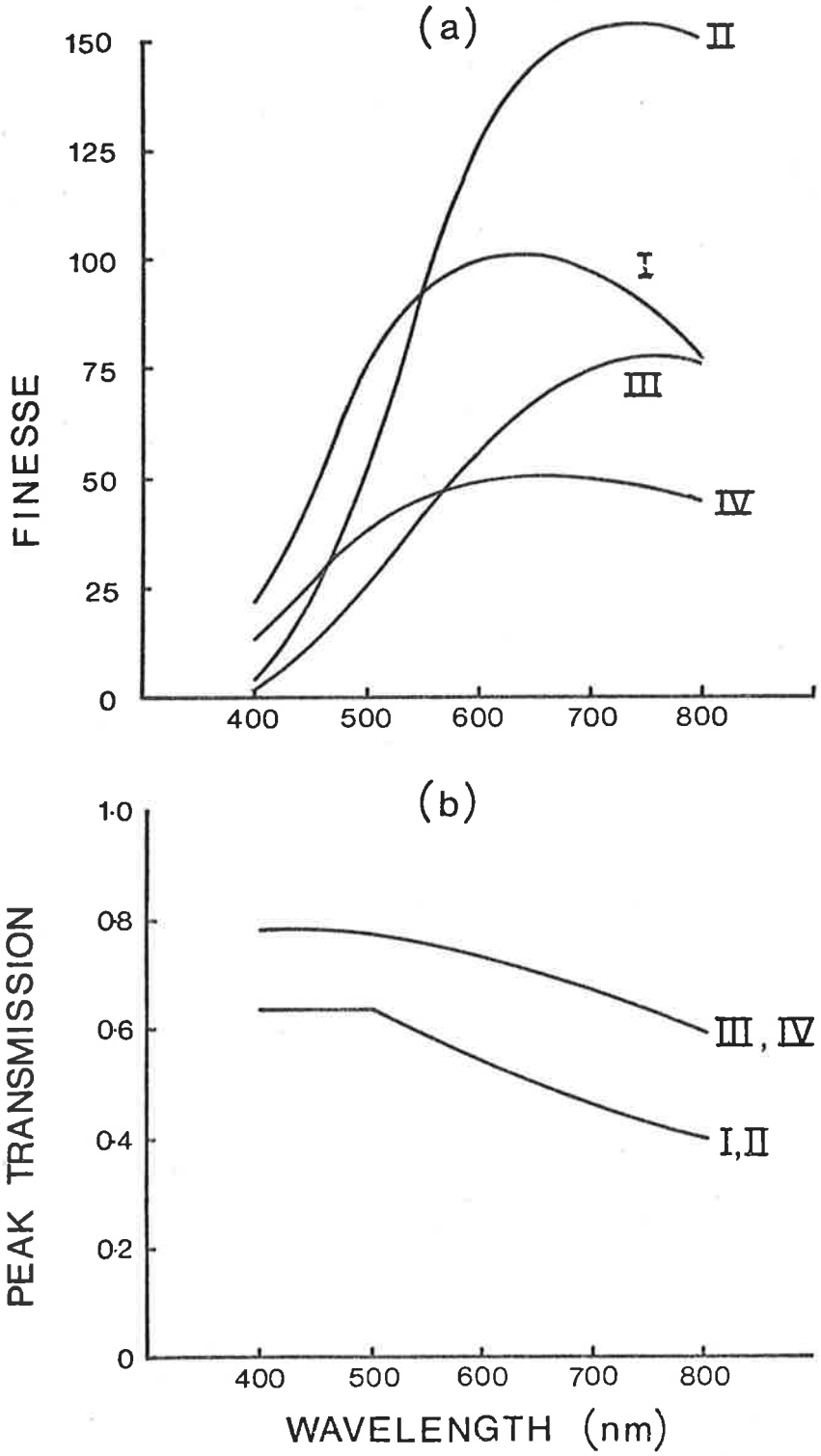

Fig. 14. Illustration of the properties of four different high reflectance coatings proposed for use on the FPI plates. The reflective finesse as a function of wavelength is shown in (a) and the peak transmission in (b).

function is negligible. The FPI plate spacing is also made small (less than 1mm) so that the source function's contribution is also very small. The profile measured by the photomultiplier is now the convolution of the Airy and defect functions. The finesse measured with this arrangement was 16.5. This low value was attributed to variation over the surface of the phase change at reflection, due to only minor coating irregularities of the order of $\lambda/200$ at 546nm (Ramsay, 1968). Lack of time prevented further work in this area, but it is clearly a problem which deserves attention, in order to improve FPI plate quality.

4.3 Parallelism Control

4.3.1 Basic Principles

The automatic parallelism control system used in the Mawson Institute FPI is based upon the Ramsay (1962) design. For the sake of completeness the principles of this system will be outlined.

The operation of the servo loop which controls parallelism of the FPI plates is explained with reference to Figures 15 and 16. The sensing of parallelism is achieved optically along two orthogonal axes designated X and Y. Control about the X-axis only is illustrated in Figure 15, for simplicity. Collimated white light from the source (S), is projected down through the working surfaces of the FPI; after two reflections in the lower plate (P_L)it passes up through the surfaces again and is finally detected at D. The pyramidal surfaces on the underside of P_L are polished at 90° to one another, which ensures that the traverses A to B and C to D of the FPI are parallel.

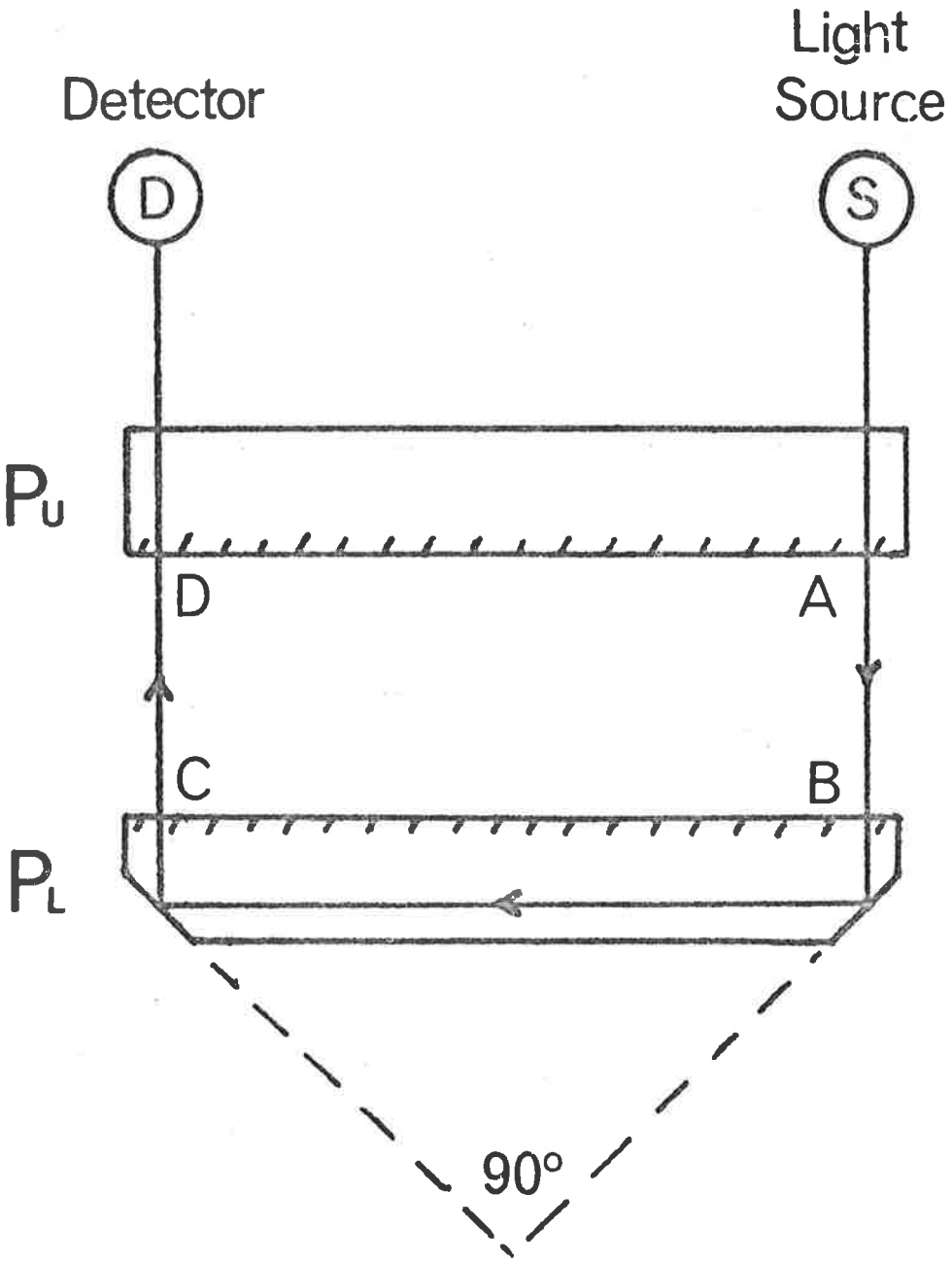

FIG. 15. Schematic diagram illustrating the principle of the Ramsay automatic parallelism control system.

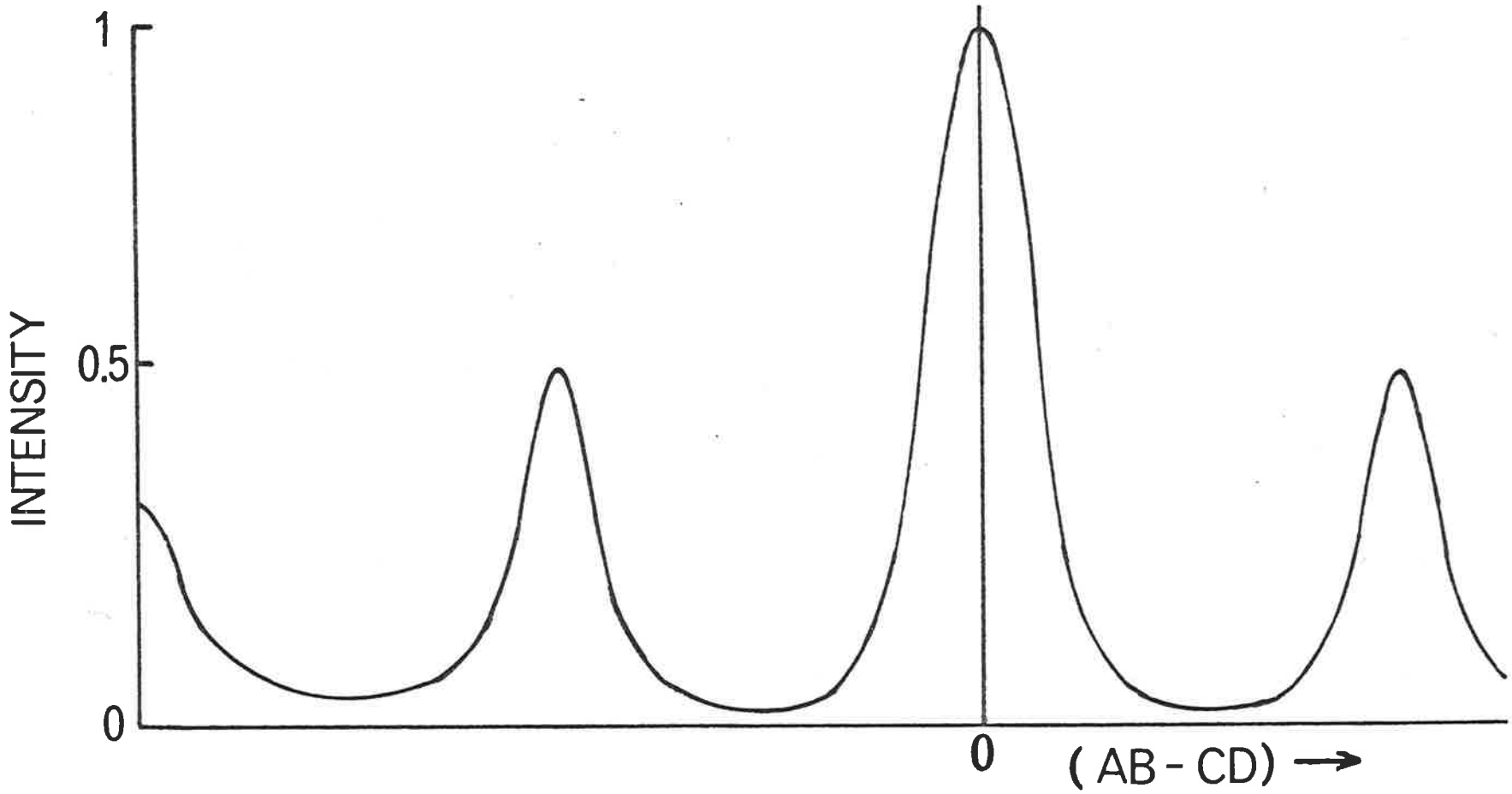

FIG. 16. The superposition of two channel spectra, as a function of the difference in the two FPI's plate spacings, (AB-CD).

The transmission through interferometer AB, is in the form of a channel spectrum. The superposition of two of these spectra, which results from traversing the two interferometers AB and CD, has a large maximum when AB = CD. When this condition is met along both the X and Y axes then the plates are parallel. Tilting the plates away from parallel reveals subsidiary maxima of decreasing intensity as shown in Figure 16. The principal maximum is easily distinguished because its amplitude is approximately two times that of the largest subsidiary.

Referring to Figure 17, the automatic parallelism control maintains the signal from the two detectors DX and DY at a maximum. This is achieved by oscillating the upper plate and then maximising the mean value of the oscillatory signal obtained at the detectors. The upper plate is oscillated about its centre, by applying a sine wave drive to each of the piezoelectric stacks supporting it. As the sine wave drives are shifted 120° in phase relative to each other the centre of the plate remains stationary. The output of the detectors thus contains an oscillatory as well as a DC component and when the oscillation is symmetrical about the peak of a maximum (see Figure 18) then the detector output contains no component at the driving frequency. The oscillation observed will actually be at twice the driving frequency. Any error in positioning will produce a component at the driving frequency, the phase of which indicates the direction of the error. The three possible situations are shown in Figure 18.

The signal from the detector is amplified by a preamplifier and then passed via a bandpass filter to a phase sensitive detector (see Figure 17). This compares the phase of the error signal with a

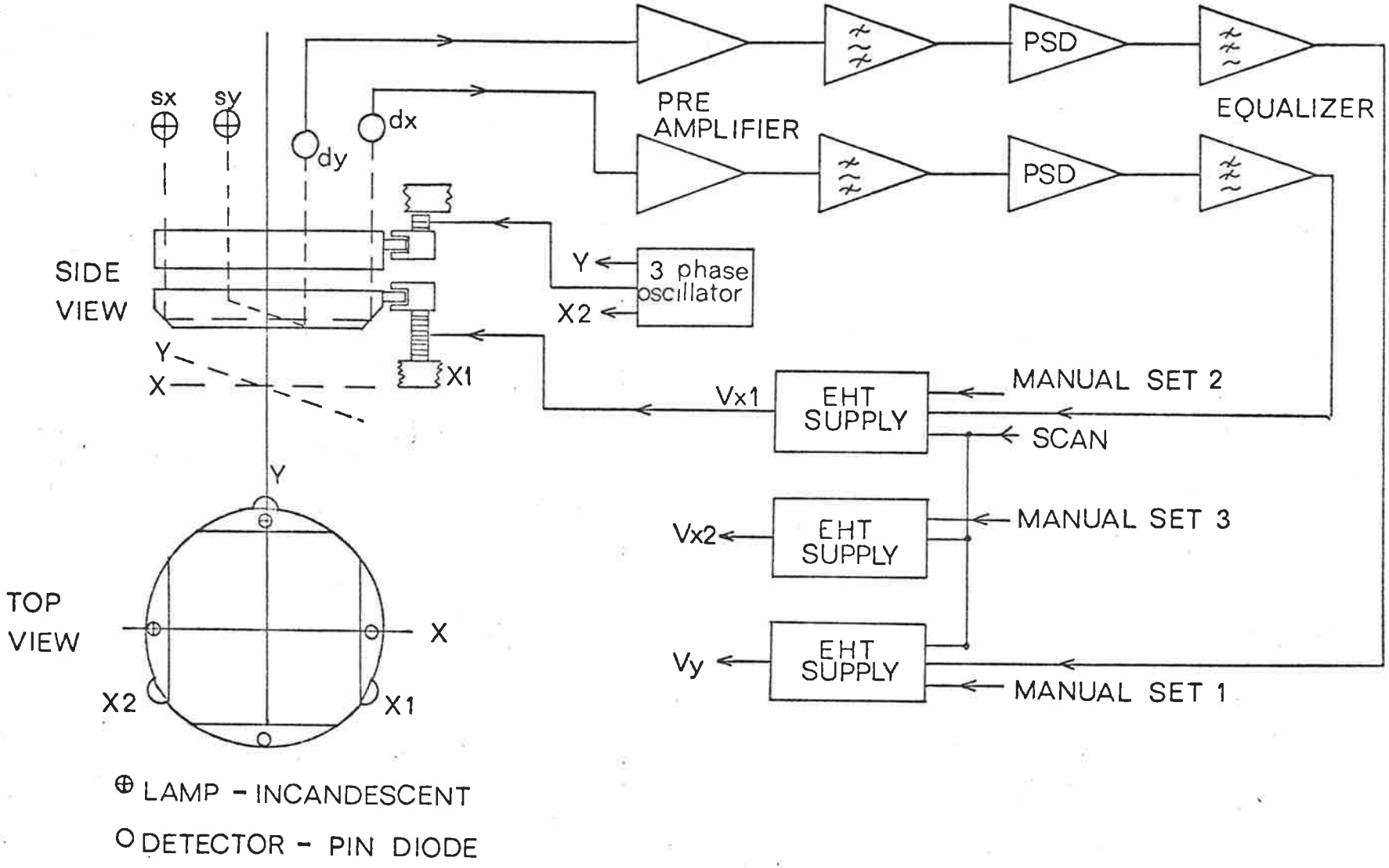

FIG. 17. Block diagram illustrating the operation of the automatic parallelism control.

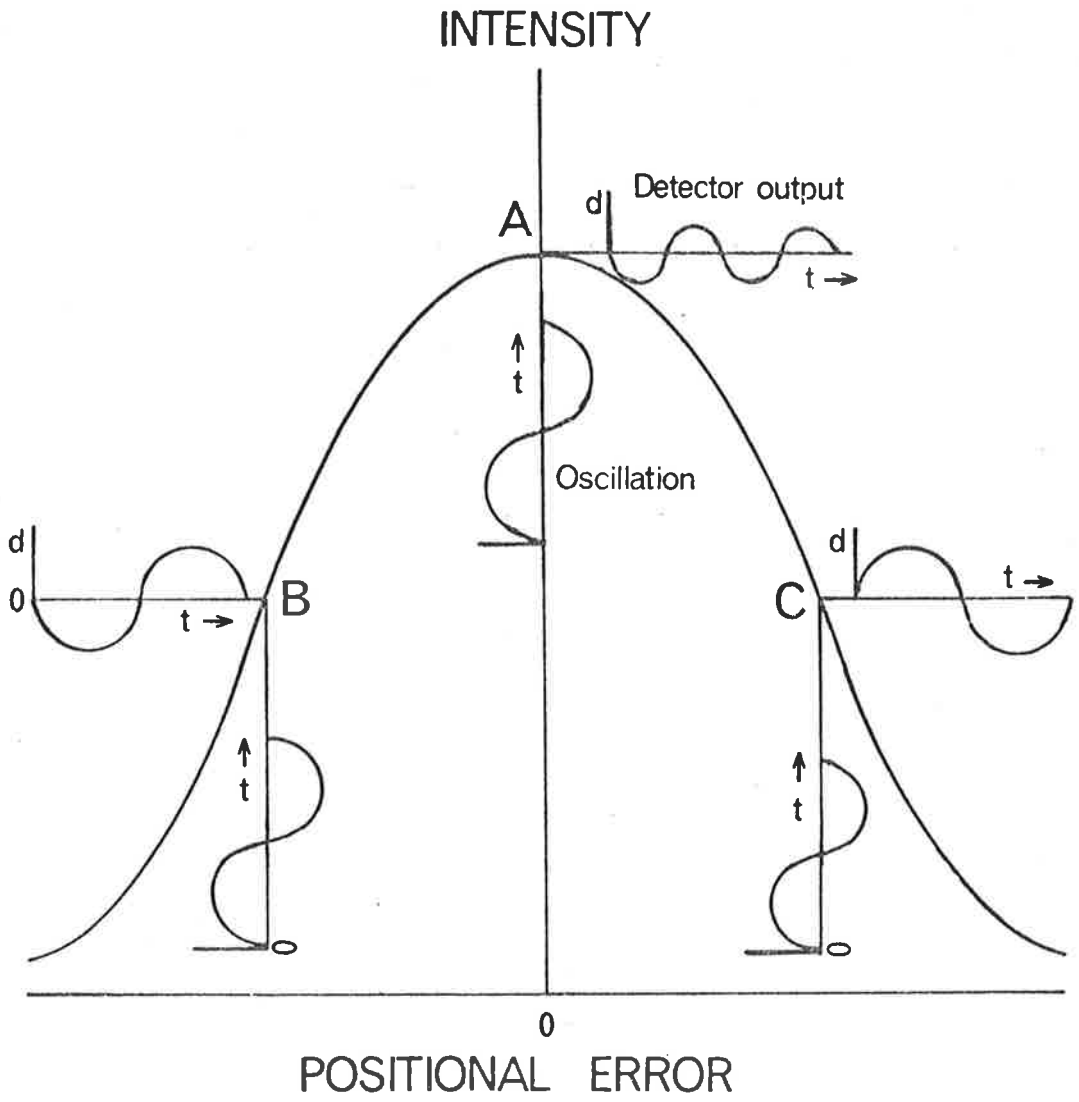

FIG. 18. Sensing of positional errors by application of an oscillating signal. The oscillatory output at position A contains no component at the driving frequency, while the outputs at B and C are at the driving frequency and opposite in phase.

reference and supplies a correction voltage of the appropriate polarity to the 600V supplies, which drive the stacks supporting the lower plate. Feedback between the 600V supplies ensures that the mean plate spacing remains the same when corrections are applied by the parallelism control circuitry. For example, an error along the X-axis is corrected by application of a signal corresponding to half the required correction to stack designated X1 and due to the feedback network, a correction of the same magnitude, but of opposite polarity is applied to X2.

The shaping of the overall response of the loop is achieved with the equalizer circuit, which is placed between the phase-sensitive detector and 600V supplies.

4.3.2 Collimated Light Sources and Detectors

The optical design of the collimated light sources and detectors are illustrated in Figure 19. The lamps were nominally rated at 2 volts, 0.25 amps, but were normally operated below this rating in order to extend their life. The globe is followed by a lens to condense the light on a pin-hole 0.1mm in diameter. The pin-holes were constructed by pricking holes in aluminium foil and then glueing the small piece of foil onto a brass mounting disc. A set of such pin-holes were made with diameters in the range 0.05 to 0.25mm, from which the 0.1mm ones were selected. The pin-hole is accurately positioned at the focus of the objective lens (28mm, f/4) so that a collimated beam of light is produced. In addition to the focussing adjustment, the light sources were constructed so that the globe position could be altered to maximise the intensity of the lamp output.

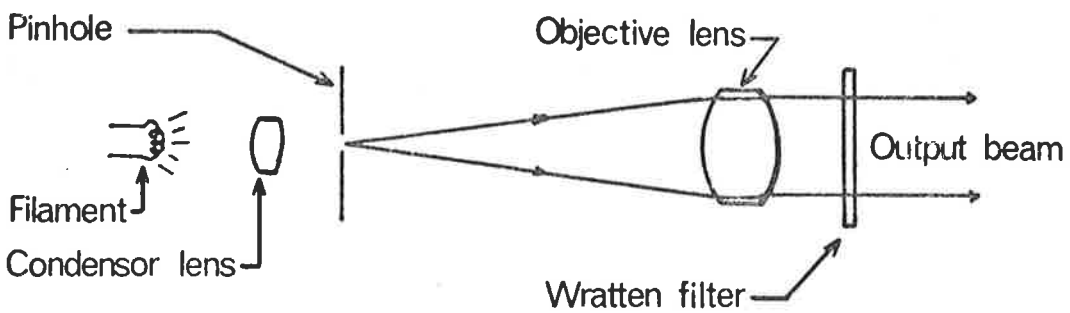

(a) Collimated light source

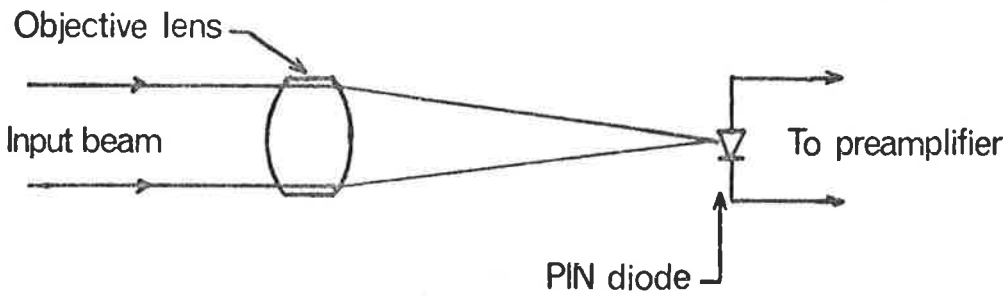

(b) PIN diode detector

FIG. 19. Schematic diagram illustrating construction of (a) the collimated white light sources and (b) the PIN photodiode detectors.

The detector construction consists of an objective lens, the same as used in front of the lamps followed by the PIN diode detector, in the focal plane. It is possible to adjust the position of the diode relative to the lens to maximise the signal output. The PIN diodes used were hp-5082-4200 series, supplied by Hewlett-Packard.

As mentioned in the last chapter a further refinement was required to the lamp-detector system to eliminate background light reaching the photomultiplier tube. This was the addition of a Wratten 87C filter in front of each of the lamps to absorb the spectral region of the lamp output to which the photomultiplier has most sensitivity.

4.3.3 Gain Requirements

The design requirement for the parallelism control was that the errors in parallelism should be less than the flatness defects of the plate surfaces. This means that the servo control errors should be less than 5nm. The maximum scanning range required is one half wavelength at λ630nm (namely 315nm) which implies a DC loop gain of at least 60. A gain of 300 was achieved quite readily without instability setting in.

The electronic circuitry for the automatic parallelism control is described in the Appendix.

4.4 Separation Control

The servo system for control of the separation of the FPI plates is based upon the capacitance displacement transducer, which has already been described in some detail. Details of the

detection electronics are given in the Appendix.

4.4.1 Capacitance Displacement Transducer

The construction of the capacitance displacement transducer is shown in Figure 21. It consists essentially of five stainless steel discs which have been carefully machined and polished so that their thicknesses are accurately matched and equal to 2.54mm. The three discs labelled 1, 3 and 5 have a nominal diameter of 32mm and are separated by stainless steel rings and mica washers, as shown. The two discs 2 and 4 are bolted together with an insulated steel bolt and are spaced apart by a stainless steel spacer and two mica washers. These two discs are supported relative to the other three by leaf springs made of phosphor bronze, which are not shown in the diagram. These springs press against small grub screws with conical tips made of fused silica to ensure electrical isolation between the discs. Electrical contact is made with the discs via rolled copper tubes, which press into holes drilled in the discs. The transducer is encased in a meehanite holder lined with a SRBP tube to provide electrical insulation.

The transducer is mounted relative to the FPI plates as shown in Figure 20. This diagram also illustrates the coupling between the top plate and the capacitance transducer. The invar rod which acts as a push rod on the transducer is clamped to the upper plate support ring by use of a camera shutter cable release. The cable release was chosen because it enables operation of this clamp from outside the étalon chamber. The clamping point can be adjusted to allow compensation for thermal expansion of the metal in the coupling between the plates. This is achieved by adjusting the position of the threaded tube to which the cable release is fixed. This

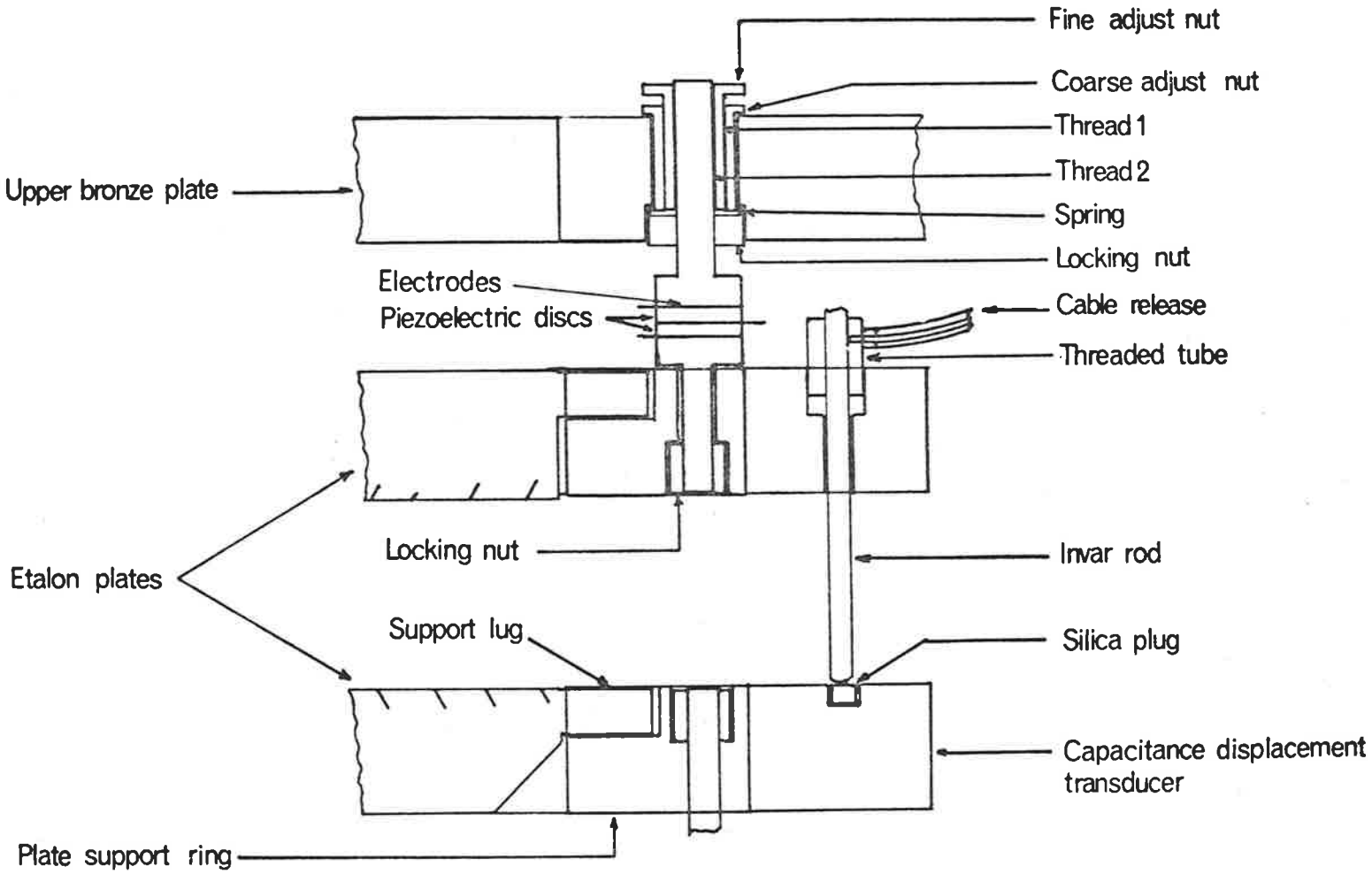

FIG. 20. Illustration of the FPI plate support system. The coupling system between the étalon and the capcitance displacement transducer is shown.

varies the length of steel in the coupling system relative to the length of invar rod, thus changing the thermal expansion characteristics.

The invar rod is insulated from disc number two by a small silica plug with its upper face polished to reduce friction between the rod end and the plug. Movement of one of the étalon plates causes the assembly, consisting of discs two and four to move relative to the other three discs. When this assembly is centrally positioned the inter-disc spacings are nominally 50μm, which corresponds to a capacitance of approximately 150 pF.

4.4.2 The Servo Loop

The electrical equivalent circuit of the transducer is a capacitance bridge as shown in Figure 21. When the invar rod is pushed down capacitances C_{23} and C_{45} decrease while C_{12} and C_{34} increase. With the AC drive voltage applied between disc 3 and discs 1 and 5, this implies that the AC voltage at 4 increases while that at 2 decreases. A differential amplifier detects the change in voltage between 2 and 4 and passes the resultant signal to a band-pass filter which is tuned to the drive frequency of 10 kHZ. The filtered signal is then rectified to produce a DC voltage proportional to the displacement. This voltage is amplified by the inverter stage. There is also provision to manually adjust plate separation by introducing an offset voltage at the input of the inverter stage. The output from the inverter is presented at the input of the equalizer along with the barometer correction and the external scan signal.

The gain requirements for the servo loop are the same as those discussed in Section 4.3.3 for the parallelism control. The gain

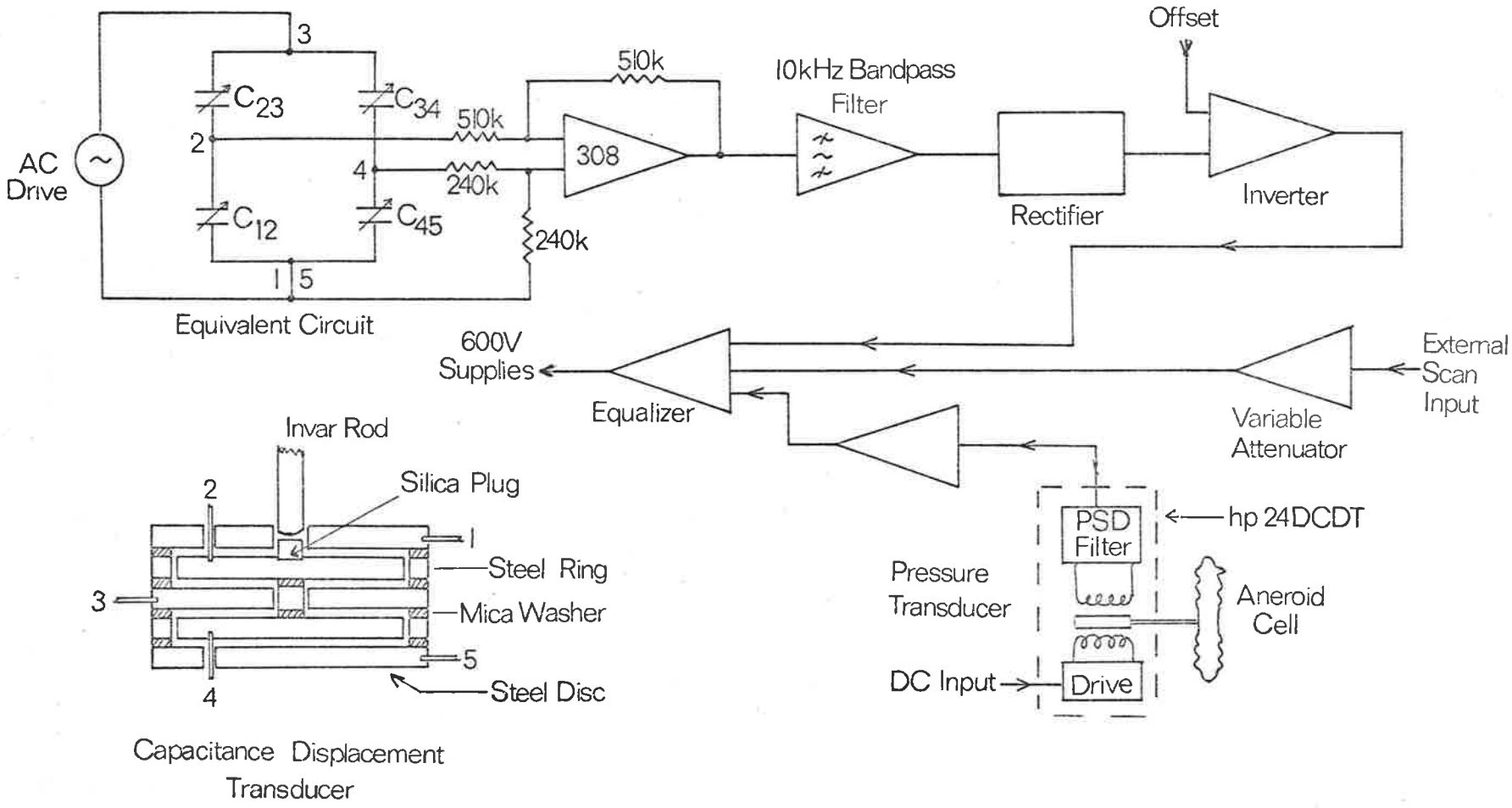

FIG. 21. Block diagram illustrating the automatic separation control of the FPI plate spacing. Schematic diagrams of the capacitance displacement transducer and the pressure transducer are also shown.

of the various stages in the loop were arranged so that without the equ alizer the loop had unity gain. The necessary gain of 100 times was thus introduced in the equalizer circuit.

The transducer is in the balance or so-called null position when the inter-disc capacitances are all equal and the error signal should be at a minimum. The phase of the AC error signal will be opposite on either side of this position. For the servo loop to control about this position would require the use of a precision phase sensitive detector and it was decided that the development of such circuitry would be too time consuming and so the simpler approach of always operating one side of the null position and measuring only the amplitude of the error signal, was adopted.

4.4.3 Barometer

The spacing of the FPI plates during normal λ630nm airglow observations is approximately 10mm. The medium between the plates is air, which will change in refractive index when the atmospheric pressure varies. At a separation of 10mm, a pressure change of 1 kPa (10mb) will alter the refractive index of the air by 2.73×10^{-6}. This is equivalent to a separation change of 27.3nm, which implies that quite small atmospheric pressure variations will be significant. To compensate for such variations a pressure transducer, which for this type of application is usually called a barometer, will be required with a resolution of approximately 5 Pa

A schematic diagram of the barometer design is shown in Figure 21. An atmospheric pressure change causes a deformation of the evacuated aneroid cell. A lever system couples the cell to the Hewlett Packard 24 DCDT-100 displacement transducer, which has been

described in Section 3.4.1. The output voltage from the transducer is directly proportional to the displacement, and hence the pressure change.

The output from the transducer is passed to an amplifier with variable gain, to permit the correct setting of the pressure-voltage coefficient. This gain will need to be adjusted whenever the FPI plate spacing is altered and is provided as a front panel control.

The barometer was placed inside the temperature controlled box which houses the FPI and was found to compensate for atmospheric pressure variations quite satisfactorily.

4.4.4 Scanning the FPI

The interferometer schematic diagram shown in Figure 22 illustrates the interconnection of the electronics for scanning and recording the spectrum. The Nuclear-Data ND-1100 Analyzer System is used as a signal averager. At the start of a scan, counts detected at the averager are added into the first channel of the memory. After a preset time the averager steps to the second channel. The process is repeated for subsequent channels until 128, 256 or 512 channels have been scanned, and then the averager returns to channel one and the sequence is repeated until the signal to noise ratio of the spectrum being recorded is deemed to be satisfactory. As the signal averager scans across the memory it outputs a DC voltage (channel address output) which is directly proportional to the channel number. This signal is applied to the external scan input of the FPI, after some attenuation and so produces a linear variation of the FPI plate spacing.

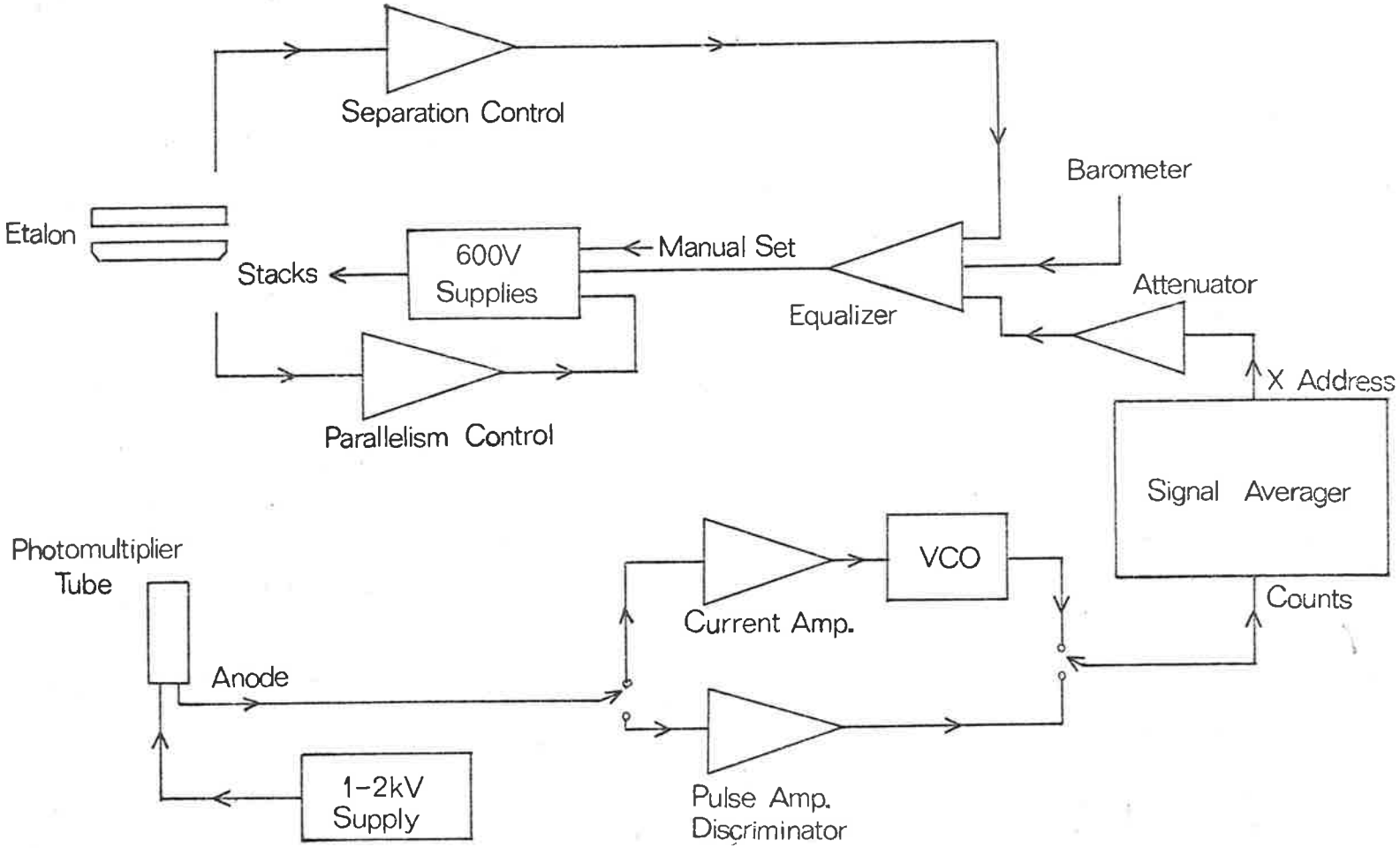

FIG. 22. Block diagram illustrating how the FPI is scanned. The interconnection between the servo controls and the signal averager, which accumulates the signal counts, is shown.

The schematic diagram also illustrates the interconnection of the two control servos while the FPI is being scanned and the two alternative detection systems, which will be fully described in the next chapter. The output from either of these systems, which is in the form of pulses, is applied to the "counts input" of the signal averager.

4.5 Temperature Control

The temperature control system has already been described in some detail in the last chapter and so only a brief summary of its operation and a description of the electronic design will be given here.

The air temperature inside the box enclosing the interferometer is controlled to within 0.1°C by circulating heated air with three paddle-wheel type fans. The mean air temperature inside the box is set at 30°C which is well above the air temperature inside the field station. The commercial air-conditioner unit in the field station is run continuously and maintains the temperature at approximately 20°C.

To maintain adequate thermal stability it was found necessary to provide two other temperature controllers. The first of these is in the form of a small number of turns of electric-blanket heating wire wrapped around the lens-cell. The temperature is controlled by a thermistor embedded deep inside the cell. The second heater also consists of electric blanket heater wire and is wound on the outside of the aluminium barrel enclosing the étalon chamber. The thermistor is embedded in the vertical wall of this barrel. The set-point for both these controllers is 30.5°C and the stability

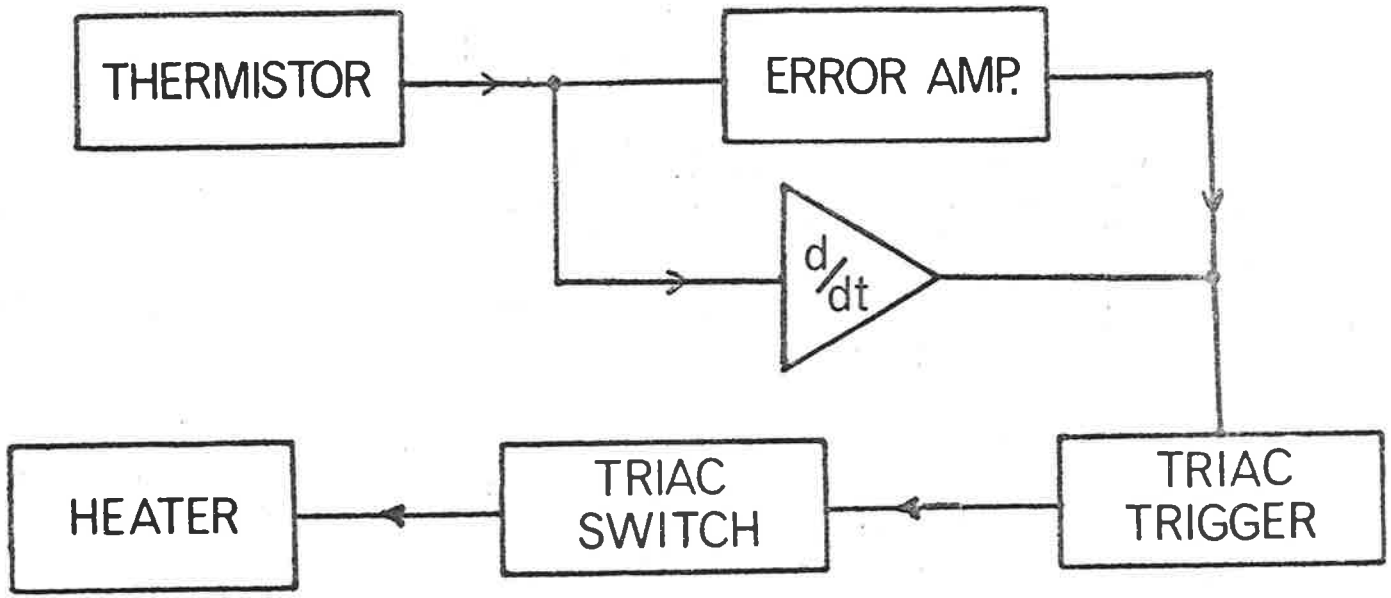

FIG. 23. Block diagram of the temperature control system used in the FPI.

achieved is typically within a few milli-degrees over a period of 24 hours. This stability was verified by monitoring a thermistor placed inside the étalon chamber, to detect air temperature fluctuations.

4.5.1 Basic Principles

A sensing thermistor is placed in good thermal contact with the medium which is to be temperature controlled. The resistance of the thermistor is compared with a selected resistor included in the error amplifier, and if the comparison indicates an error then the current to the heater is switched on or off, depending on the direction of the error. In the temperature range of $\pm$ 0.01°C about the set-point proportional control occurs. This means that as the set-point is approached the heater current is increased or decreased in proportion to the temperature error. In the case of the air temperature controller there is also rate-feedback incorporated into the servo-loop, which in part compensates for the poor coupling between heater and thermistor. The system is shown in block diagram form in Figure 23. The details of the electronic circuitry are given in the Appendix.

CHAPTER 5

DETECTION OF VERY LOW LIGHT LEVELS

5.1 Introduction

In order to study the diurnal variation of the Doppler temperature for the normal λ630nm nightglow emissions it is necessary to contend with intensities as low as 10 Rayleighs (Schaeffer, 1970). For the purposes of the following discussion an emission of this intensity having a Doppler width corresponding to a temperature of 1000K is considered to be incident on the Mawson Institute FPI. If the instrumental profile is centred on the emission line then the light flux at the photomultiplier tube will be approximately 100 photons/second. For a photocathode of the S-20 type, this flux will produce less than 10 pulses/second at the anode. A photomultiplier with a two inch diameter S-20 photocathode, when cooled to -30°C has a residual dark count rate several times this value. Hence it will be necessary to integrate for a period of time long enough not only to reduce statistical fluctuations in the signal, but also in the background produced by the photomultiplier. This chapter is devoted to the endeavours which were made to increase the efficiency of available photomultiplier tubes and at the same time to decrease the dark count rate. The electronic circuitry which was developed to detect the anode current pulses is also described. The investigations were carried out on a number of EMI 9558B photomultiplier tubes which had been used for several years in airglow photometers. During the development of the FPI there were a number of periods of time during which mechanical modifications were being made and it was in this time that the studies of low level light detection were

carried out. When the observations were commenced it became apparent that further improvement could be achieved by using pulse counting detection and also magnetic defocusing and so these modifications were made at a later stage.

5.2 The Photomultiplier Tube

The EMI 9558B photomultiplier tube is a 50mm diameter tube with a 44mm cathode of the S-20 (tri-alkali) type. According to the manufacturer's data the quantum efficiency of this photocathode is 6% at a wavelength of 630nm. The dynode structure is of the venetian blind type, with 11 dynodes having CsSb secondary emitting surfaces. The collection efficiency of this dynode system is such that about one-third of the electrons leaving the photocathode are lost (Coates, 1973).

The EMI 9558 photomultiplier tube has been widely used in applications where the long wavelength response is important, such as in laser studies at λ633nm and in astronomy and airglow studies. Consequently a large amount of published data is available specifically relating to studies on this type of tube. For example Rodman and Smith (1963), Young (1963), Nakamura and Schwarz (1968) and Foord et al. (1969), to name only a few.

The tests described in this chapter were carried out with the tubes operating at their rated sensitivity of 200A/lm, unless specifically stated otherwise. The overall voltage for this sensitivity and the other parameters supplied by the manufacturers are given in Table 3.

The voltage divider chain employed is a standard EMI design called the "linear chain", because the interdynode voltages are

TABLE 3

TEST-TICKET DATA SUPPLIED BY EMI FOR

PHOTOMULTIPLIERS USED DURING INVESTIGATIONS

Serial No.	EHT for 200A/lm	Dark Current (nA) at 20°C	Cathode Sensitivity (μA/lm)
9265	1700	1.0	132
9737	940	1.0	168
9964	1050	0.7	124
10016	1010	4.0	194
11609	1090	1.2	158

all equal. The cathode-first dynode voltage is stabilised using a 150V zener (1N742). For pulse counting operation the last dynode is decoupled to ground and the two previous dynodes decoupled to it.

5.3 Quantum Efficiency Enhancement by Total Internal Reflection

5.3.1 Introduction

The basic principle of this technique for enhancing the efficiency of a photomultiplier tube is illustrated in Figure 24. A small glass prism is optically coupled to the photomultiplier end-window with a drop of oil, enabling the introduction of a light ray into the window, such that the ray is totally internally reflected at both the photocathode-vacuum interface and the window-air interface. The conditions for total internal reflection at these two interfaces are identical if the refractive indices of a vacuum and air are taken as both being unity. If the refractive

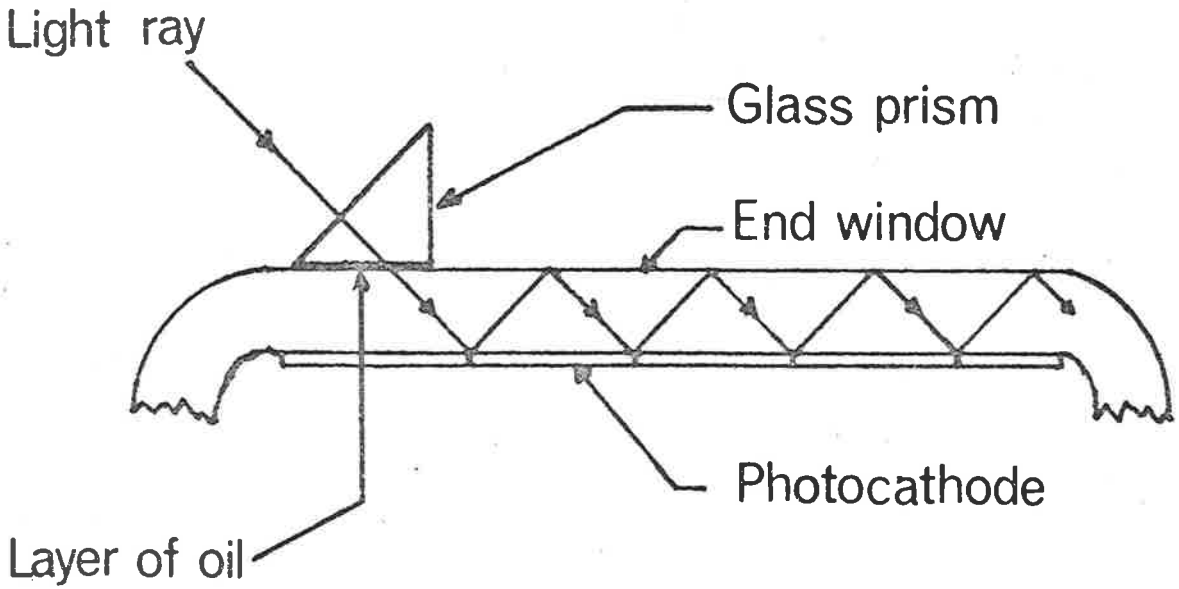

FIG. 24. Illustration of quantum efficiency enhancement by total internal reflection of a light ray in the photomultiplier tube end window.

index of the tube window is n_1, then the ray is totally internally reflected if,

$$\theta_1 \geq \arcsin\left(\frac{1}{n_1}\right) \qquad (5.1)$$

where θ_1 is the angle of incidence at the window-air interface.

For light of wavelength λ630nm an S-20 photocathode absorbs only 20% of the light at normal incidence with 30% being reflected and 50% transmitted (Kondrashov and Shefov, 1964). The introduction of the light into the tube window so that multiple reflections occur will considerably reduce this 80% loss.

This technique appears to have been independently originated at the Air Force Avionics Laboratory (Rambo, 1964) and at the NASA Ames Research Centre (Gunter et al. 1965) and has been subsequently refined such that a quantum efficiency of almost 60% has been achieved at λ400nm, for a selected EMI 9558QB tube, (Jennings et al. 1970). Practical devices for use in existing optical systems have been described by Oke and Schild (1968), Hirschfeld (1968) and by Gunter et al. (1970) and in all cases the improvement in efficiency at λ630nm is at least a factor of two for S-20 photocathodes. For this reason it was decided that the addition of an enhancement device to the Mawson Institute FPI would be a worthwhile exercise, provided it did not require extensive modifications to the existing construction.

5.3.2 Preliminary Measurements

5.3.2.1 Measurements on Photomultiplier Tube

The design of the enhacement device required knowledge

of the refractive index and thickness of the tube end-window. The EMI handbook on photomultipliers states that the window material was borosilicate glass, but does not specify the thickness or refractive index.

The refractive index was measured using a Pulfrich refractometer. It was calibrated using distilled water as a standard. The refractive index was measured at a number of wavelengths with uncertainties estimated to be less than 0.001. The refractive index at λ630nm was determined by interpolation and was taken to be 1.47.

The end-window thickness was measured using a travelling microscope and found to be 3.0mm. The above measurements were carried out for only one sample, however it was considered that these parameters were unlikely to vary much between tubes.

5.3.2.2 Design Considerations

In the Mawson Institute FPI the photomultiplier tube has its photocathode centred on the optic axis of the output optics, which deliver an f/2 beam. As stated earlier, the enhancement device was to be introduced without extensively modifying the existing design and should, therefore accept an f/2 beam.

The first two devices considered were original in design and are illustrated in Figure 25. For the design in (a), theoretical consideration revealed that approximately 80% of the f/2 beam would make two transits through the end-window. It was decided not to proceed with construction of a prototype because it was felt that better designs were available, which would be easier to build.

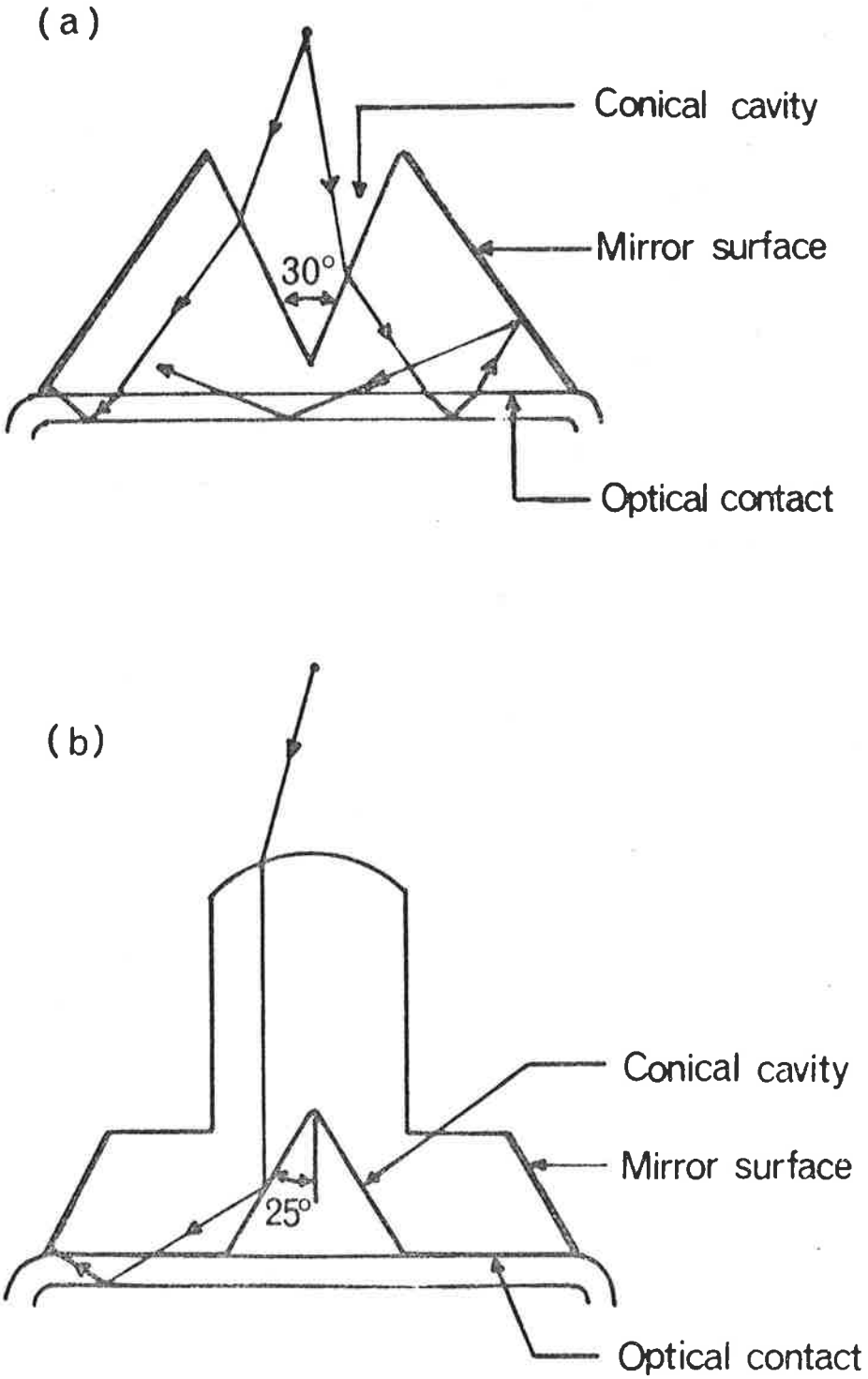

FIG. 25. Two designs of enhancement device which both give two internal reflections in the tube end-window.

A prototype of the design in Figure 25(b), was constructed from perspex. This material was chosen because it was fairly simple to machine and polish to the desired shape. Considerable difficulty was encountered in depositing a mirror surface on this material and this was one reason for discarding this design. The prototype was used with a number of 9558's and the best enhancement achieved at λ630nm was approximately 1.75 times. This is certainly a significant gain, but the results reported by other experimenters were considerably better than this, and so it was decided to search for a better design.

5.3.3 Hirschfeld Cone

The next device which was considered and eventually utilised in the FPI, was based on a design suggested by Hirschfeld (1968) and so will be called the Hirschfeld cone. The basic principles are indicated in Figure 26(a). A truncated cone with its smaller face in optical contact with the tube window, has a collimated beam of light incident upon it. The maximum diameter of the base of the cone, ω, is dependent on the thickness of the tube window ℓ,

$$\omega = 2\ell\tan\theta \qquad (5.2)$$

where θ is the angle of incidence at the window-photocathode interface. The usable portion W of the entrance window of the cone is given by

$$W = 2\omega\cos\theta \qquad (5.3)$$

assuming the refractive index of the cone and the tube window are the same. This is a reasonable assumption for a cone of perspex, which has a refractive index of 1.490 at λ630nm. In equations (5.2) and (5.3) the value of θ can be assigned by using equation

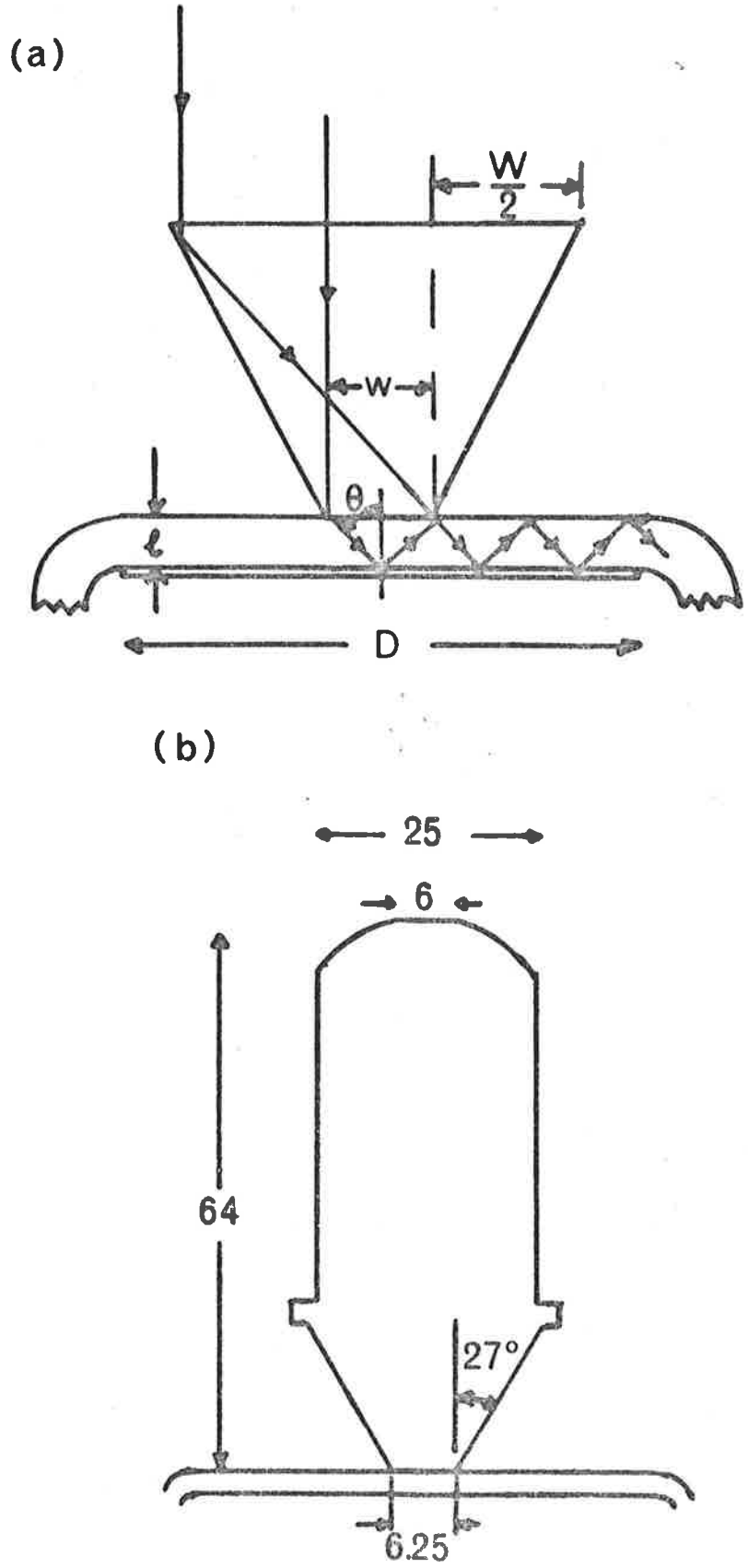

FIG. 26. The Hirschfeld cone. The basic principles of the device are illustrated in (a). The modified Hirschfeld cone used in the Mawson Institute FPI is shown in (b), where the dimensions given are in mm.

(5.1) and so the maximum values of ω, W are determined. Hirschfeld (1968) has considered the case of an uncollimated beam with an angular range $\Delta\theta$ in air. This is reduced in the tube window to $\Delta\theta^1$ given by

$$\Delta\theta^1 = 2 \arcsin \left(\frac{\sin \Delta\theta/2}{n_1}\right) \qquad (5.4)$$

Equations (5.2) and (5.3) now become:

$$\omega = 2\ell\tan(\theta-\Delta\theta^1/2) \qquad (5.5)$$

and

$$W = 2\omega \frac{\tan \theta/2}{\tan(\theta+\Delta\theta^1/2)-\tan\theta/2} \qquad (5.6)$$

The central portion of the beam will pass through the base of the cone and so will not be enhanced. This has been called the unenhanced percentage U and is given by:

$$U = 100(\omega/W+\omega)^2 \qquad (5.7)$$

The modified Hirschfeld cone used in the FPI is shown in Figure 2.6(b). The dimensions were computed using an angle of incidence in the window of 55° and window thickness of 3mm, which allows 2 to 3 bounces at the photocathode, while an earlier prototype allowed 3 to 4 bounces at 47°. The lens surface on the top of the device ensures that the beam is approximately collimated and so $\Delta\theta^1$ is small. The results obtained for three 9558's are tabulated in Table 4.

The enhancement was found to be independent of the photomultiplier overall gain setting. A further refinement to the lens surface was made to reduce the unenhanced percentage. The

TABLE 4

TABULATION OF THE ENHANCEMENTS OBTAINED AT λ630nm FOR THREE EMI 9558B PHOTOMULTIPLIERS USING MODIFIED HIRSCH-FELD CONES

Photomultiplier Ser. No.	Enhancement 3-4 bounces at 47°	2-3 bounces at 55°
9265	1.85	1.9
9737	1.9	1.9
11609	2.25	2.25

central area of the lens was polished flat over a diameter equal to ω. For the 9558 serial number 9265, this increased the enhancement to 2.1 times. With this refinement it was estimated that the unenhancement percentage was less than 20%.

Having established the feasibility of obtaining a two-fold improvement in the effective quantum efficiency, the device illustrated in Figure 26(b) was installed in the FPI.

5.4 Reduction of Dark Current

5.4.1 Temperature Dependence

It is well known that cooling a tube with an S-20 photocathode will greatly reduce the dark current, with dependence as shown in Figure 27, for tube number 10016. The dark current is not reduced significantly below -30°C and it has been reported in some cases to increase with further cooling (Rodman and Smith, 1963). The residual or non-thermal component that remains is non-Poisson in character, having a variance much greater than the mean count rate.

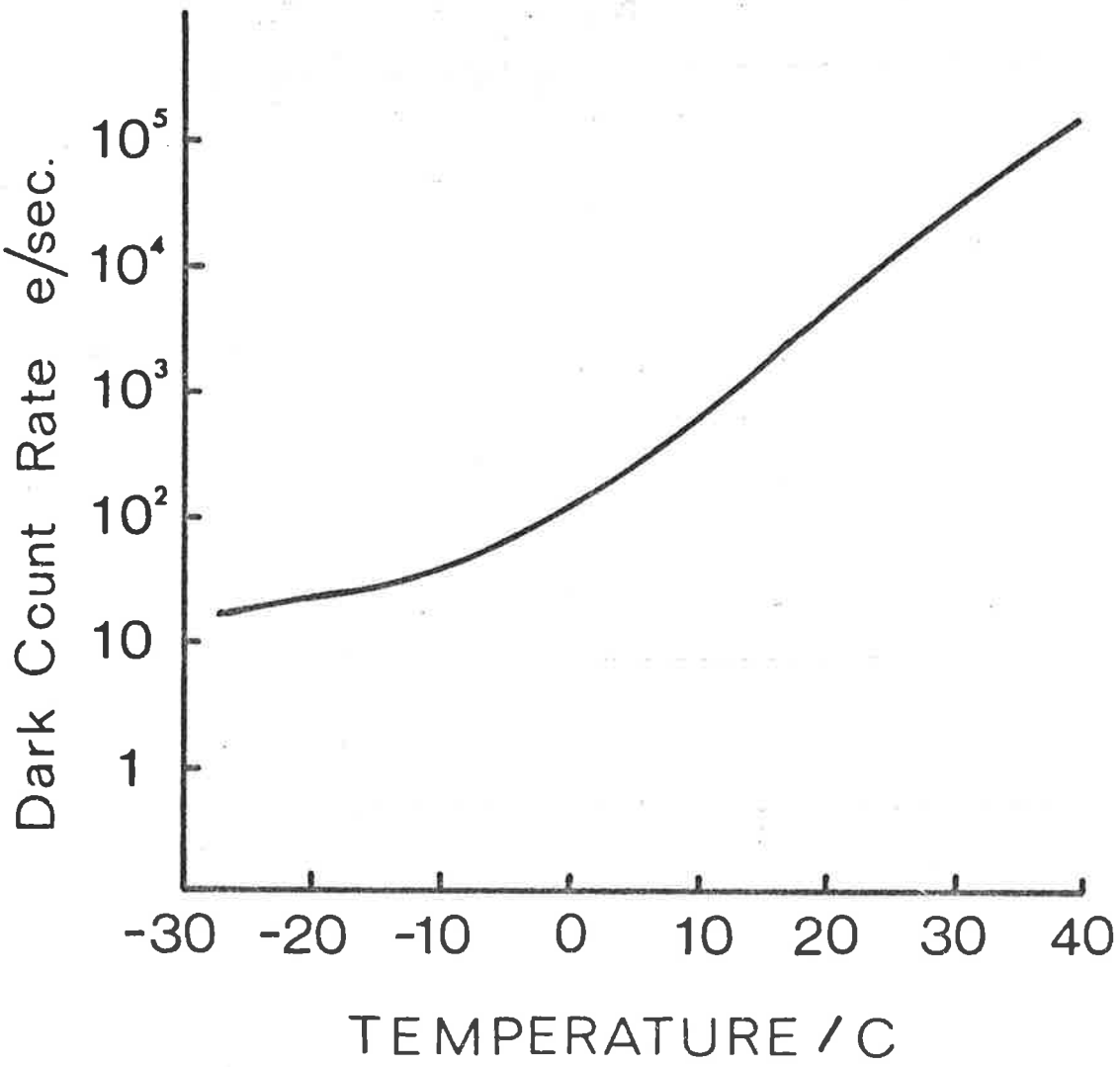

FIG. 27. The dark count rate in electrons/sec, as a function of temperature for the photomultiplier tube EMI 9558B, serial number 10016.

The temperature dependence of overall tube sensitivity is a somewhat more contentious issue. The measurements of Young (1963) indicate that the anode response of two 9558's increased by approximately 50% when cooled to -30°C for a wavelength of 630nm. Nakamura and Schwarz (1968), however, have measured a six to seven times reduction in anode sensitivity for the 9558 they tested. It is clear that differences between individual tubes must be very significant and so tests were carried out on the tube that was to be used in the FPI. The results obtained for the tube 10016 are in agreement with those of Young (1963). Cooling to -30°C increases the anode sensitivity at λ630nm by approximately 40%, relative to the room temperature value.

For the particular 9558 to be used in the FPI it has thus been shown that cooling is highly advantageous in reducing the dark current and also increasing the overall tube sensitivity.

5.4.2 Magnetic Defocusing

After observations had been commenced it was found that the residual dark count rate of the cooled photo-multiplier was typically several times greater than the peak signal count rate. The technique of dark current reduction by using magnetic defocusing was considered even though it would negate some of the signal improvement achieved by use of the Hirschfeld cone. The reason is apparent from Figure 28, which illustrates the principles of magnetic defocusing. A short solenoid is placed around the outside of the photomultiplier tube adjacent to the photocathode. The passage of a current through the solenoid produces a magnetic field between the photocathode and first dynode, as shown.

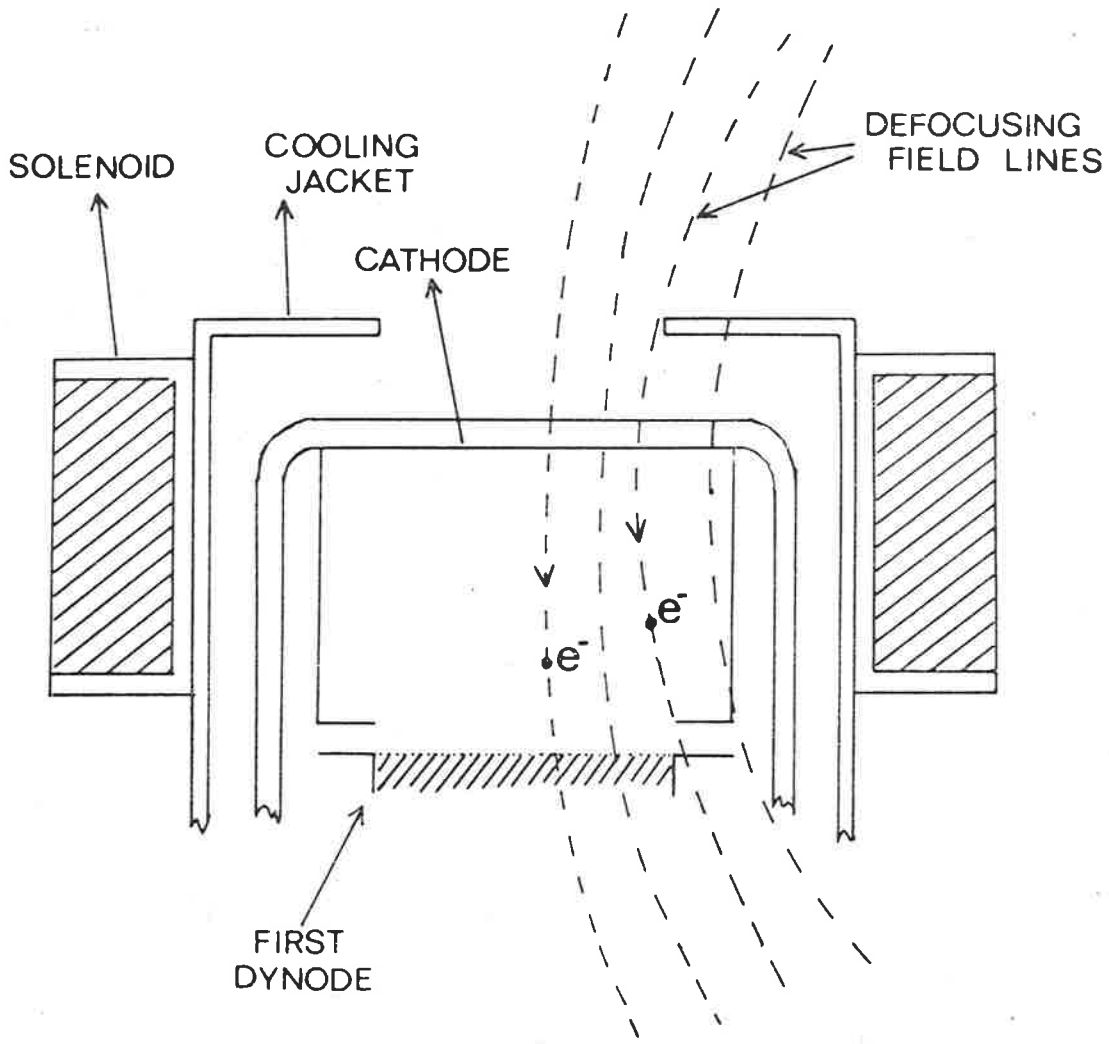

FIG. 28. Magnetic defocusing for reducing the dark current of an end-window photomultiplier tube with venetian blind dynode structure.

Electrons leaving the outside of the cathode are directed away from the first dynode and so are not multiplied while those from the centre of the cathode are not deflected. If the light to be detected is directed to the central area of the photocathode then there will clearly be an increase in the signal count to dark count ratio. The first experimental results published on this technique appear to be those of Farkas and Varga (1964), who reported an increase in the signal-to-noise ratio of at least an order of magnitude for a CVP 150 type photomultiplier. Subsequent results have been reported by Frommhold and Feibelmann (1967) and Topp et al. (1969) who verified the work of Farkas and Varga, in each case using EMI 9558's. A most thorough investigation of magnetic defocusing again applied to a 9558 has been published by Knight et al. (1968). They experimented with three different field geometries, all of which increased the signal-to-background ratio. A more interesting result was the effect the defocusing had on the dark count pulse height distribution, in eliminating a greater number of large pulses than the small ones. This means that the difference between the pulse height distribution for light and that for dark counts is greater and so use of a lower level discriminator will further increase the signal-to-background ratio.

The authors of the above publication have been mainly concerned with the use of magnetic defocusing as a substitute to cooling the tube and so have given little indication of the effect of defocusing on a cooled tube used in the pulse counting mode. Frommhold and Feibelmann (1967) have reported that the reduction in dark current at dry ice temperature is somewhat less than at room temperature and the results of Topp et al. seem to imply that

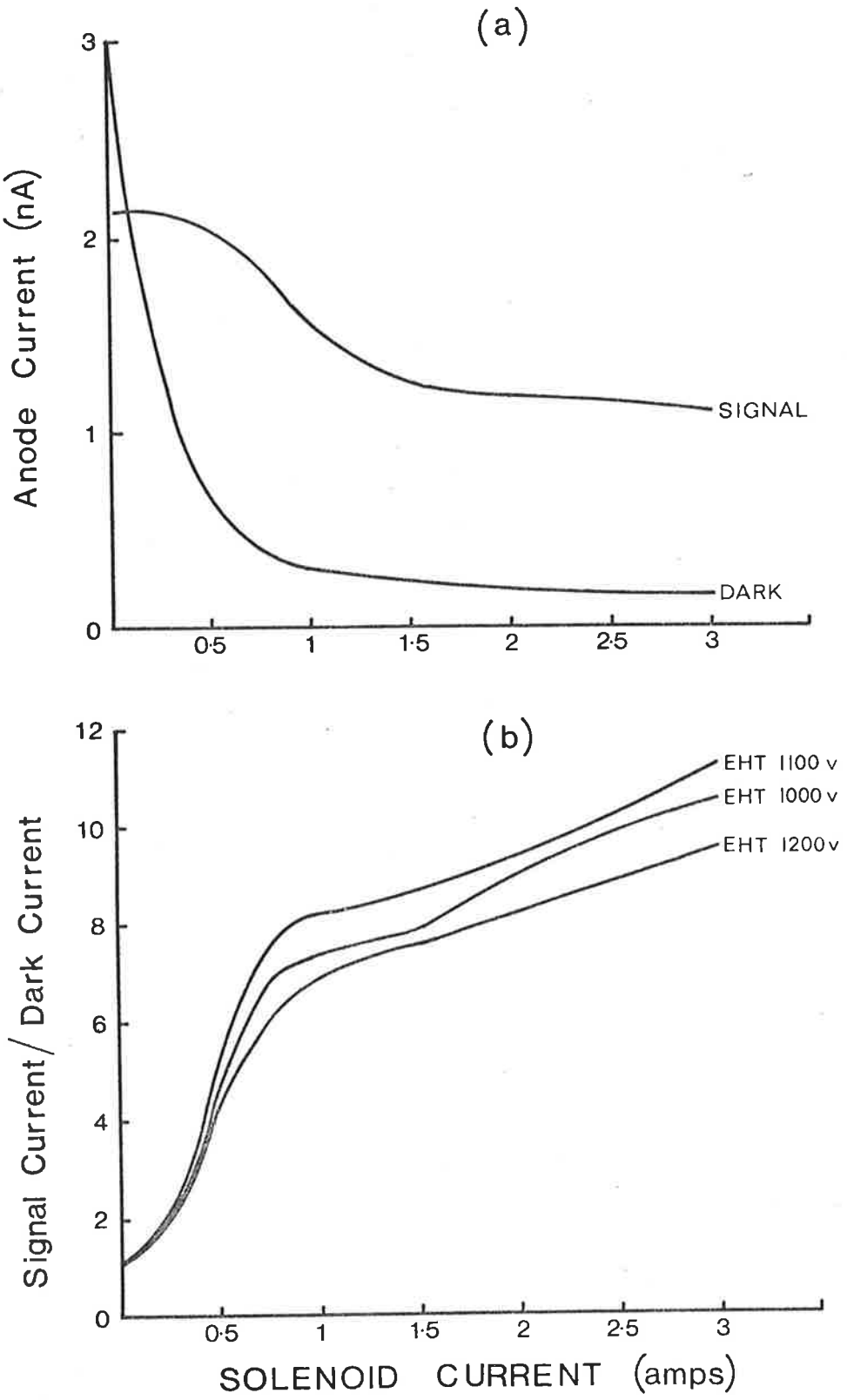

FIG. 29. The variation of signal and dark current as a function of coil current for tube number 9964 is shown in (a). The variations of the ratio of signal to dark current as a function of coil current for three different overall voltages applied to the tube are shown in (b).

this is also the case for the dark count rate. It was therefore not apparent from the literature whether the reduction in dark counts for a cooled tube would be sufficient to offset the loss in signal suffered and so increase the signal-to-noise ratio (SNR).

A solenoid was constructed of approximately 100 turns of 1.5mm diameter copper wire over a former length of 30mm. The Hirschfeld cone delivers all the incident light into the central 12.5mm diameter of the photocathode and so initial tests (which were done without the Hirschfeld cone) were carried out with the rest of the cathode masked off. The variation of signal and dark current at 20°C, as a function of coil current, for 9558 serial number 9964 are shown in Figure 29(a). The variation of the ratio of signal to dark current as a function of coil current for three different overall voltages applied to the tube are shown in Figure 29(b). They are all normalised for a ratio of unity at zero coil current. The improvement in the ratio of signal current to dark current was essentially the same when the tube was cooled to -30°C. At the time when these investigations were being carried out, the pulse counting detection system was in use and so the chief interest surrounded the improvement that would be achieved in the SNR for a cooled tube in pulse counting mode.

The ratio of the dark count rate for zero coil current to that for a current of 0.75 amps, as a function of temperature is shown in Figure 30, for tube number 10016. The reduction of dark count rate is not as great when the tube is cooled and it appeared at this stage that there would be little increase in SNR, because a coil current of 0.75 amps caused the loss of approximately 40% of the signal.

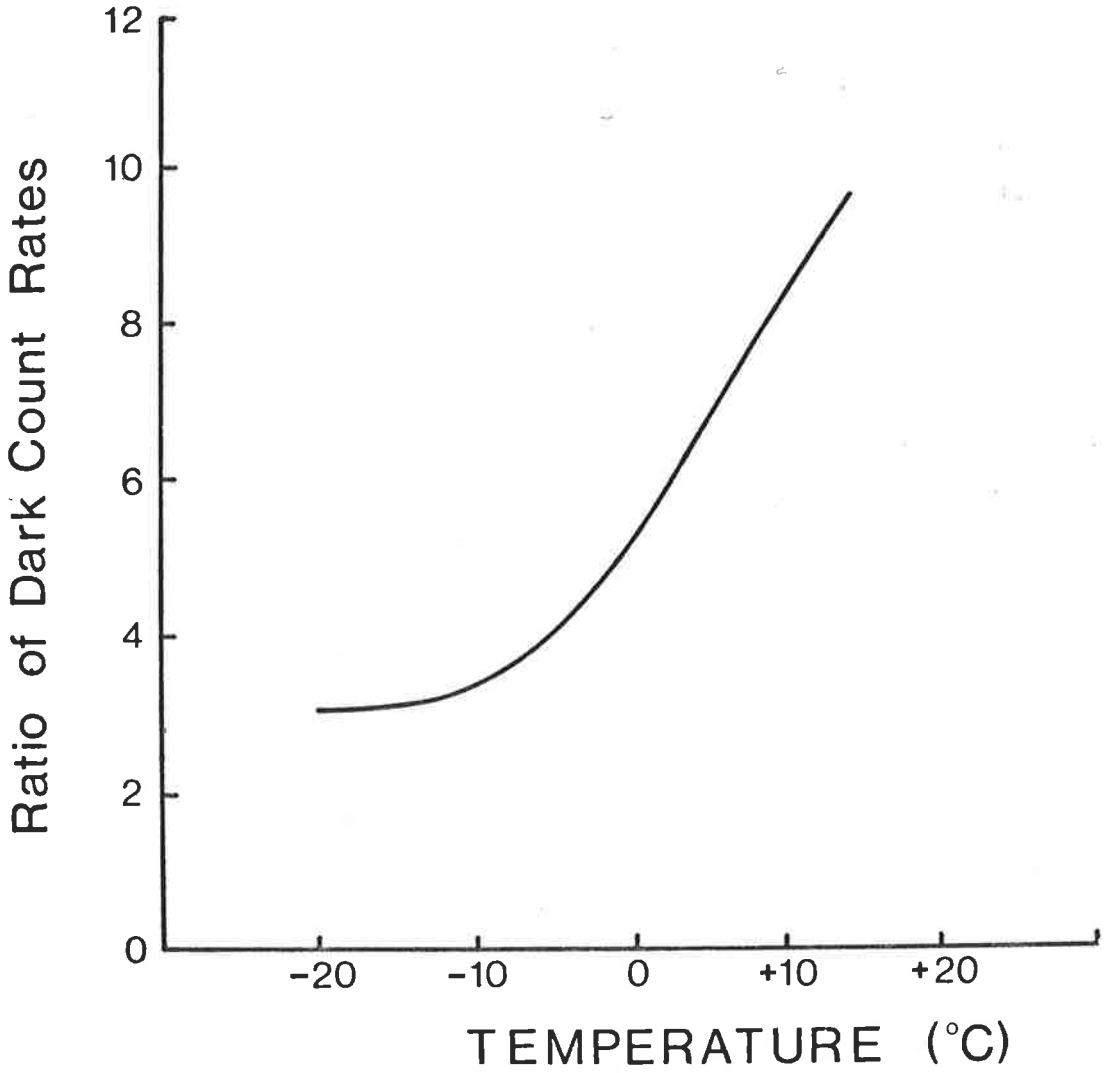

FIG. 30. The ratio of the dark count ratio for zero coil current to that for a coil current of 0.75 amps is shown as a function of temperature, for tube number 10016.

Further testing revealed that an improvement in SNR of a factor of two was obtained for signal levels of the same order as the dark count rate. This improvement was greater than would be expected from the increase in the ratio of signal count rate to dark count rate. The test involved taking 512 samples of the dark counts each over a time interval of 800 msec. A Poisson distribution with mean value equal to the sample mean was computed. The experimental and Poisson distribution were then plotted on the same graph as shown in Figure 31(a) and (b). Clearly neither of the experimental distribution is a very good approximation to a Poisson distribution. However, the statistics measured with the magnetic defocusing on are obviously a much closer fit. This conclusion is confirmed by the finding that the variance was reduced 10 times for only a four times reduction in the mean. This test was repeated for different time intervals (10 sec and 100 msec) and yielded results very close to those shown in Figure 31 (a) and (b). The non-Poisson nature of the residual dark counts has been observed previously by Rodman and Smith (1963) and by Gadsden (1965). However, the improvement with reduction in the effective photocathode area by magnetic defocusing does not appear to have been reported.

The most plausible explanation put forward for the non-Poisson statistics is that correlated after-pulsing is taking place due to the formation of positive ions in between the cathode and first dynode (Foord et al. 1969). However, no experimental verification of this theory was attempted.

An improvement of a factor of two in SNR was felt to be sufficient to warrant modifying the photomultiplier chamber to enable the use of a defocusing coil.

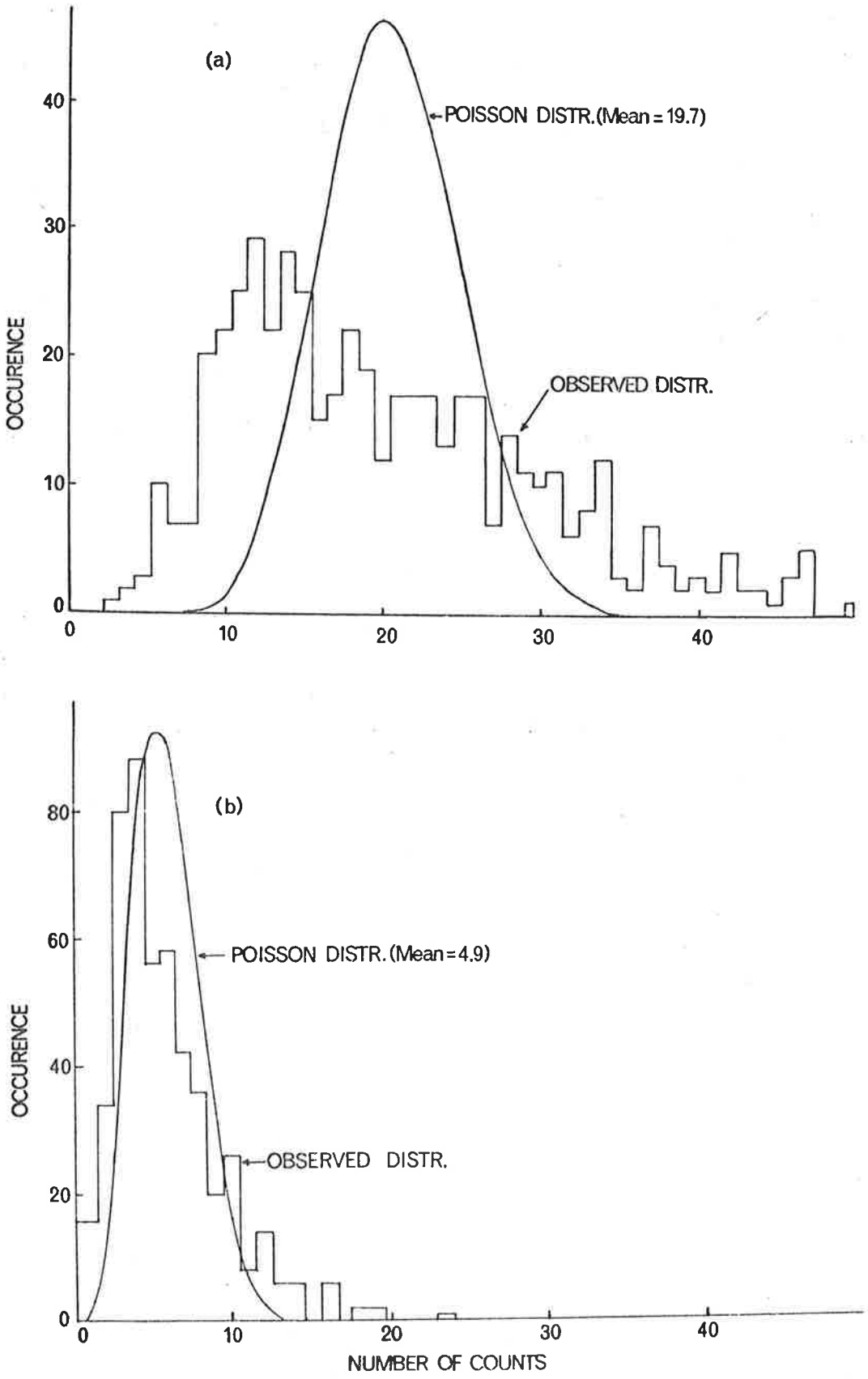

FIG. 31. The occurrence of the number of photomultiplier counts recorded in an 800ms time interval, for EMI 9558B number 10016, at -30°C. A poisson distribution with mean value equal to the experimental mean is also shown. (a) without magnetic defocusing (experimental mean = 19.7 and variance = 111.5); (b) with magnetic defocusing, coil current = 1 amp, (experimental mean = 4.9 and variance = 12.4).

5.4.3 Electrostatic Shielding

Further attempts were made to reduce the dark current of the photomultiplier tube by the use of electrostatic shielding. These were inspired by a paper published by Davies (1972). He reported that the dark current of a number of tubes including a 9558 had been reduced by more than two orders of magnitude at room temperature. This was achieved by painting the glass walls of the tube with silver paint and maintaining the coating at cathode potential. All electrical connections to the tube were made directly to the base pins by soldering on the dynode resistors and signal leads.

These measures were applied to the 9558 number 9265, which had a dark current of 1nA at a gain of 200A/lm, at a temperature of 20°C. The dark current and the tube sensitivity were found to be unaltered by this treatment. The non-thermal dark current of the tube was also measured before and after treatment and found to be unchanged.

In conclusion, it was found that although the instructions given by Davies (1972) were closely followed, that no reduction in dark current was achieved for the particular tube under test and so the decision was made to pursue more promising refinements to the detection system, such as pulse counting, which is described in the next section.

5.5 Detection Systems

5.5.1 Analogue Detection

The initial airglow observations were made using an existing analogue detection system, which was later replaced by pulse

counting circuitry developed for this application. The analogue amplifier used was constructed for use in the airglow photometers and had sufficiently good stability for use with the much lower signal currents provided by the FPI.

The operational amplifier used was a Fairchild Instrumentation ADO-24 which was connected as a trans-resistance stage so that output voltage was proportional to input current. The gain and bandwidth of the unit were switch selectable with dynamic ranges of 1000 and 10 respectively. The gain was set for airglow measurements so that the full scale output of 1 volt corresponded to an input current of 1nA and the bandwidth chosen was 25 Hz.

The output from the amplifier was fed to a voltage controlled oscillator which provided 20 KHz full scale for a 1 volt input. The pulses delivered by the oscillator were then counted by the signal averager.

The SNR obtained with analogue detection was rather poor because of the effect of large current bursts. The slow response of the amplifier implies a slow recovery from the effects of such bursts and hence serious degradation of the SNR when the signal current is less than or comparable with the dark current. This problem is overcome with pulse counting where every pulse above the lower level discriminator setting is given an equal weighting. For the typical airglow signal levels an order of magnitude improvement was achieved by replacing the analogue system with pulse counting.

5.5.2 Pulse Counting

The electronics for the pulse counting detection system are described in the Appendix. It consists of a preamplifier (50 dB gain) and provides for use of both upper and lower level discrimination.

A ratemeter was constructed which converts the average pulse rate presented at its input into a DC voltage. This was necessary for recording the FPI output on a chart recorder and for visual checking of dark and signal levels, by use of a panel meter.

Attempts were made to measure the pulse height distributions for dark counts and for signal counts. Integral pulse height distributions were obtained by using the channel address voltage out of the signal averager operating in multi-channel scaling mode. This means that the lower level threshold voltage was directly proportional to the channel number in which the counts were stored. The distributions for dark and signal counts were very similar in shape and so it was not possible to decide from these measurements the optimum setting of the lower level threshold. Differentiations of these distributions yielded very noisy results which were also of little use.

It was decided therefore, to measure the SNR as a function of lower level discriminator setting, for tube number 10016, cooled to -30°C. The average value of the dark count rate, D was obtained by making 128 measurements of the number of counts in a 2.5 second interval, for the tube in the dark. The tube was then illuminated and the procedure repeated to obtain the mean signal plus dark count rate (S+D), and its standard deviation σ_{S+D}. The mean signal rate, S was determined by subtracting the two means. The signal-to-noise ratio was then determined from the relation,

$$SNR = S/\sigma_{S+D} \qquad (5.7)$$

Figure 32 illustrates the variation of SNR with lower level

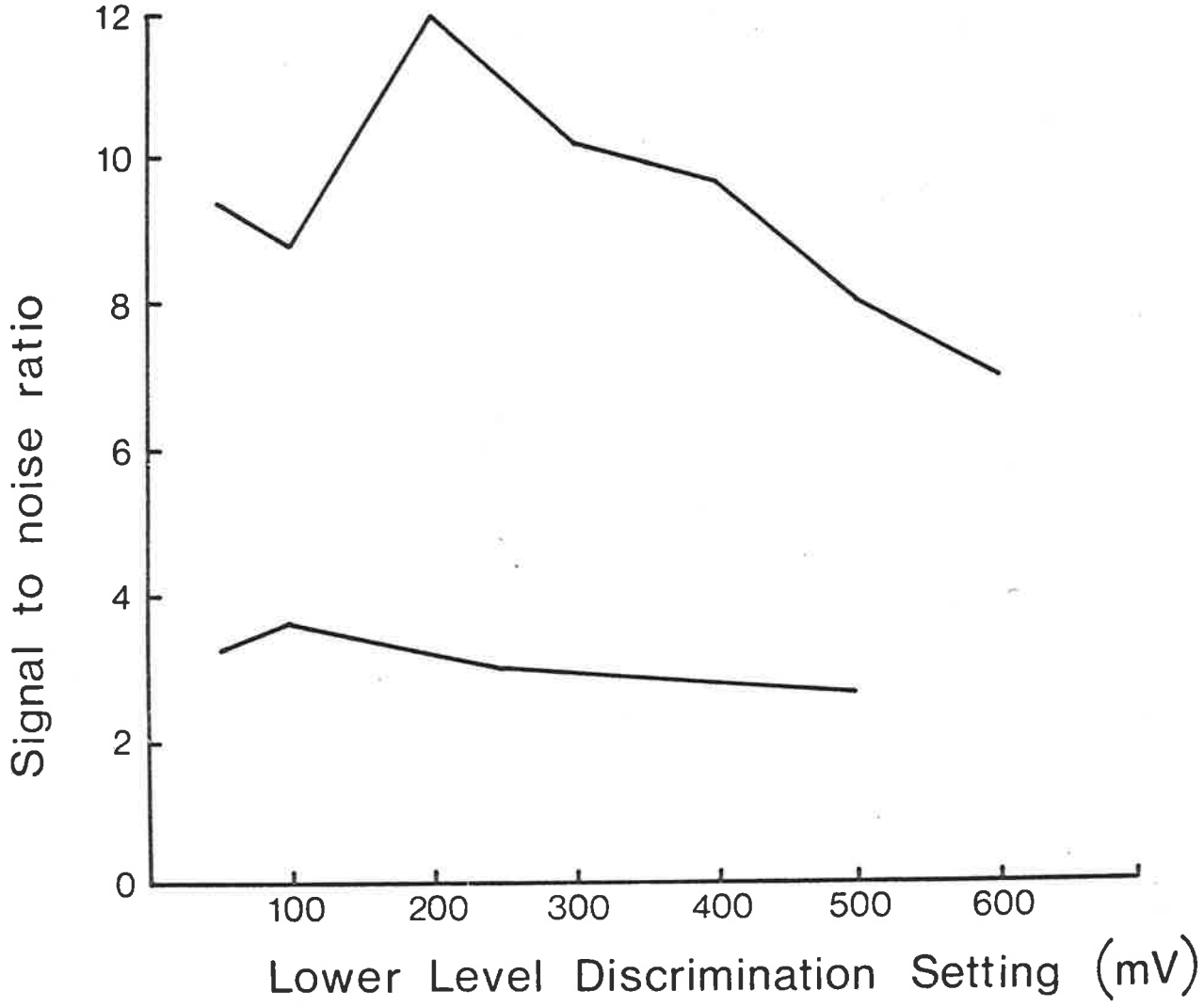

FIG. 32. The signal to noise ratio as function of lower level discriminator setting, for 9558 number 10016 used in pulse counting mode.

discriminator setting for two signal levels. For signal levels much greater than the dark count rate,

$$SNR \simeq S/\sqrt{S} = \sqrt{S} \qquad (5.8)$$

This dependence explains the steady decrease in the SNR above a discriminator setting of 200 mV, in the case of the upper graph in Figure 32. From these results a lower level discriminator setting of 150 mV was chosen.

5.6 Photomultiplier Chamber

The photomultiplier chamber shown in Figure 33 illustrates the provision of all the refinements described in this chapter. It consists of a series of concentric tubes. The outermost tube which is made of black-loaded fibreglass has an aluminium lid screwed on its bottom and a brass flange on the top, for coupling to the FPI body. The photomultiplier and cooling jacket are mounted from the base of a second fibreglass tube which slides inside the first one. This permits focusing of the modified Hirschfeld cone with respect to the output lens of the FPI. The cooling jacket is made of copper and has eight turns of 6.25mm copper tube silvered-soldered onto it. The upper half of this jacket has a machined finish to facilitate the positioning of the defocusing solenoid, as shown The Hirschfeld cone is held onto the photomultiplier by a cap constructed from synthetic resin bonded paper (SRBP), through which is mounted a thermocouple to sense the temperature of the air near the photomultiplier end-window. The lens on top of the Hirschfeld cone is positioned on the optic axis by sliding into another SRBP tube, which also holds the chamber's entrance window and an aperture. This aperture is

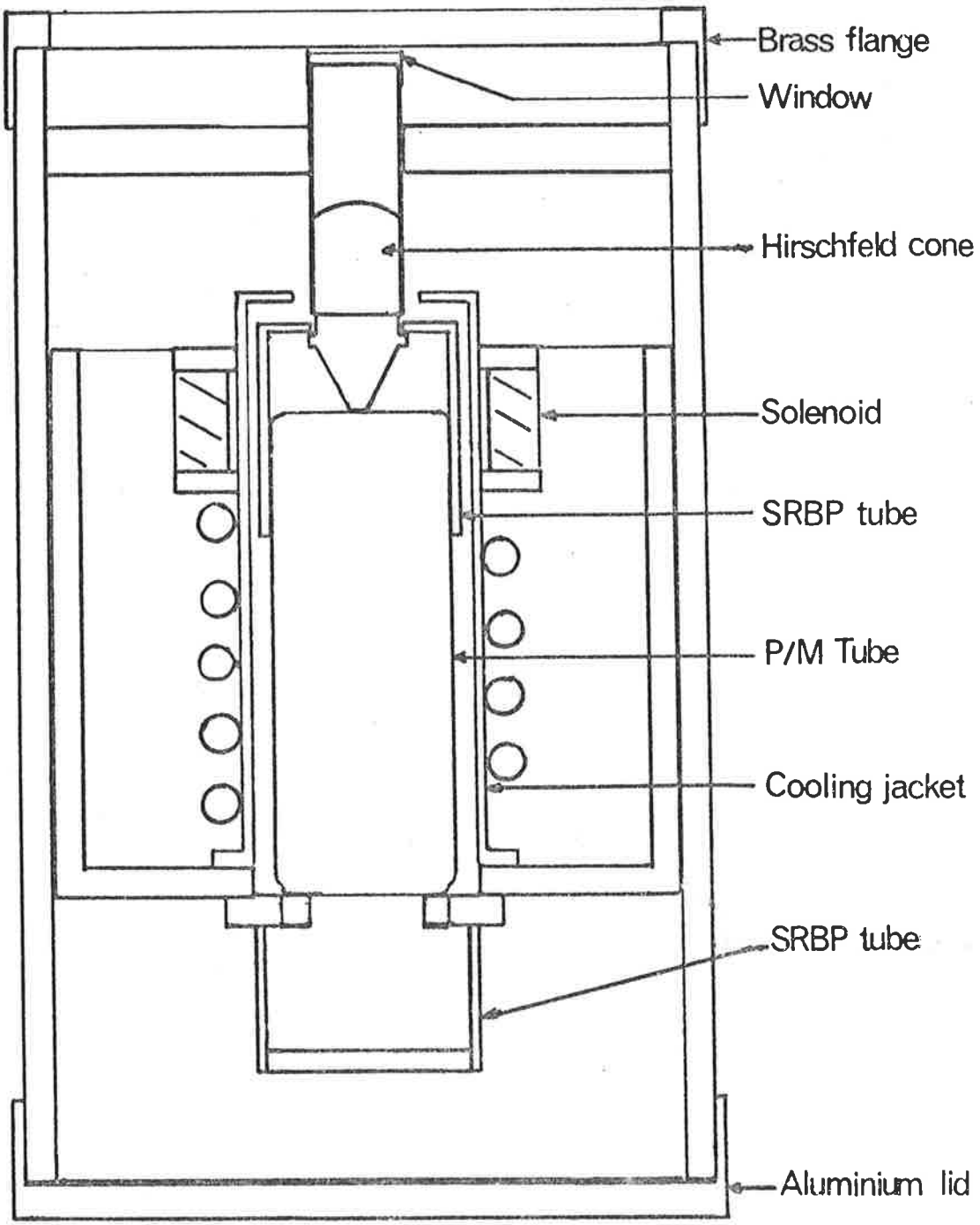

FIG. 33. Illustration of the construction of the photo-multiplier chamber.

to reduce the likelihood of any stray light being scattered into the photomultiplier chamber.

The resistors for the EHT divider chain are soldered directly onto the pins on the under-side of the tube socket and the detection electronics are mounted on the outside of the chamber adjacent to the tube base.

To reduce the effect of external magnetic fields the two outer fibre-glass tubes are lined with layers of mu-metal.

5.6.1 Shutter Control

The shutter for the photomultiplier chamber is mounted just above the entrance window and is of the iris diaphragm type, which was salvaged from an old camera. The shutter has been modified so that it can be electrically operated using a solenoid and push rod. It was originally operated pneumatically and this mode of operation was retained as a stand-by in case the electro-mechanical control failed.

Details of the electronics for operating the shutter are given in the Appendix.

5.6.2 Cooling System

The system for cooling the photomultiplier is illustrated in the schematic diagram in Figure 34. The refrigerator unit is based upon a 1/4 H.P. compressor which is connected to the cooling coils by a flexible coupling. The cooling coils are completely immersed in a reservoir of methanol-water mixture which can be cooled to below -50°C without freezing. The reservoir is

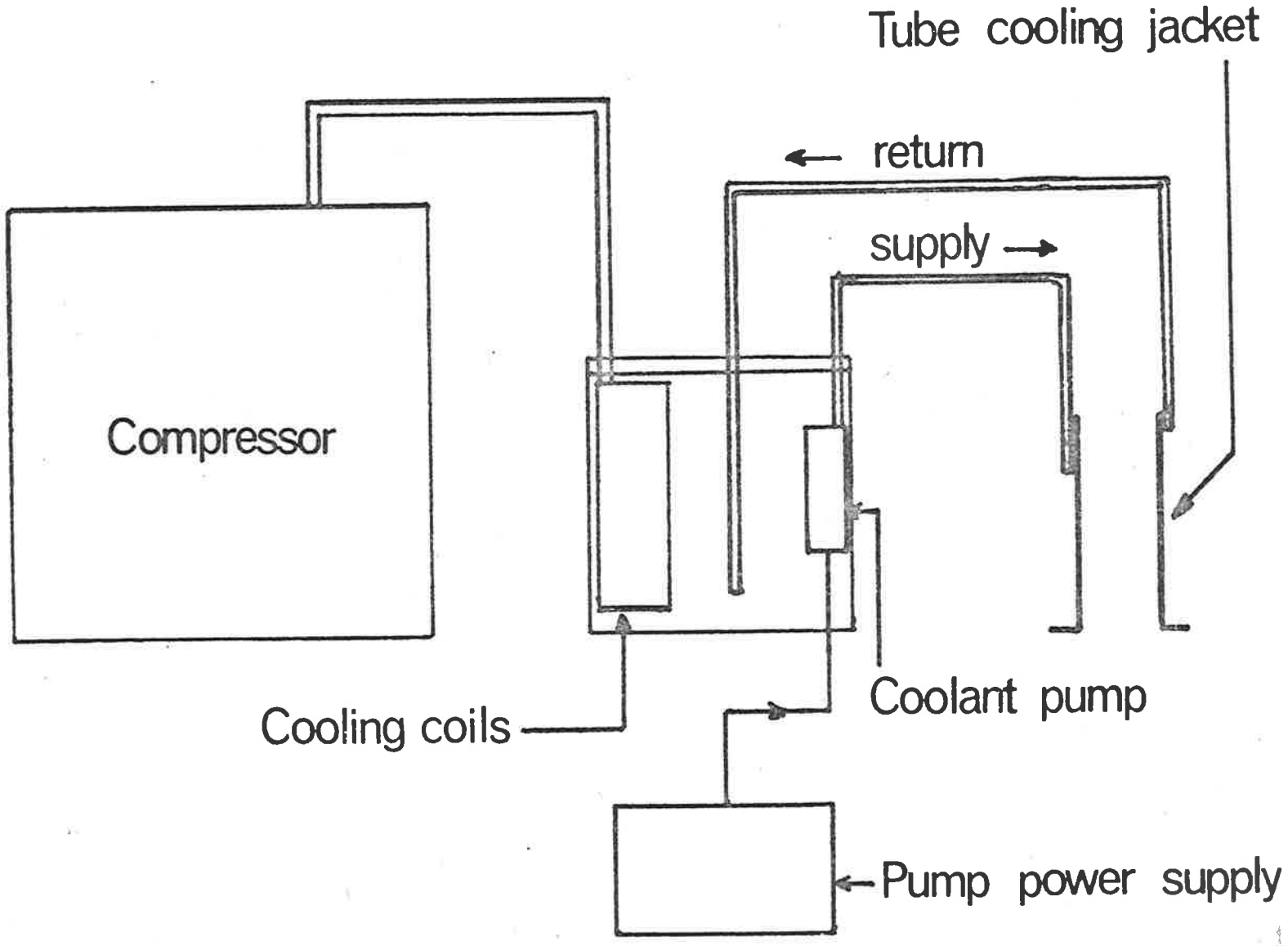

FIG. 34. Schematic diagram of the cooling system for the photomultiplier tube.

constructed from stainless steel and is enclosed in a wooden box, lined with 5cm thick polystyrene foam.

Also immersed in the reservoir is a small circulating pump which was originally designed for use as a boat bilge pump. The pump required 12 volt DC, 1 amp for operation; a power supply was built to meet this requirement. The coupling between the pump and the copper tubing on the photomultiplier cooling jacket was made with 7mm silicone rubber tubing. This tubing remains flexible at low temperatures, which is essential to minimise the transmission of vibrations to the FPI.

The cooling system was capable of circulating coolant liquid at a rate of 250 ml per minute and holding the temperature of the photocathode below -30°C.

5.7 Concluding Remarks

It has been found that for very low light levels such as are encountered in the mid-latitude airglow, the SNR of a cooled EMI 9558B can be improved by nearly two orders of magnitude by the combined use of pulse counting instead of current detection, quantum efficiency enhancement by total internal reflection and magnetic defocusing.

It is felt that a further improvement could be achieved by the use of a more sophisticated photomultiplier tube, such as the ITT FW 130. This tube has an S-20 photocathode of very small effective area (nominally 2.5mm diameter). When cooled to -30°C the dark count rate is less than 1 count per second and this residual dark count closely obeys Poisson statistics (Oliver and

Pike, 1968). This indicates that a reduction in the noise of approximately 3 times would be achieved by replacing the 9558 by an FW 130. At the low signal levels normally encountered this would imply an increase in the SNR by a similar amount.

CHAPTER 6

OPERATIONAL PROCEDURE AND ANALYSIS OF THE RESULTS

In this chapter a description will be given of how the FPI is operated and calibrated. The technique for analysis of the results will also be presented. Finally, a summary of the operating characteristics of the FPI is given.

6.1 Selection of the Order of Interference

The selection of the order of interference required careful consideration of a number of factors. The first of these involves the compromise between the light gathering power and the resolving power of the FPI. A sufficiently large light gathering power is required to enable the measurements of the λ630nm line profile to be achieved in a reasonable period of time. On the other hand, the instrument must have sufficient resolving power to obtain a certain accuracy in the determination of the line profile width and peak position. Since the resolving power X light gathering power product is a constant for a particular FPI, a compromise must be made. Chabbal (1953) claims that the optimum operating condition is achieved when the width of the source and instrumental profiles are equal. This necessitates some knowledge of the source function width and this is reasonably well known from results published by other workers. The plate spacing chosen was approximately 10mm. This spacing permits measurement of the doppler width of the λ630nm line corresponding to temperatures in excess of 2000°K.

The fine setting of the order of interference was determined by two factors. The first of these involved the consideration of

the effect that the hydroxyl lines near λ630nm may have on the apparent width and position of the oxygen line. This problem has been discussed by Armstrong (1969) and he has suggested a solution which involves careful selection of the order of interference. The order chosen satisfied Armstrong's condition, which will be fully described when the results are discussed in Chapter 7. The second factor determining fine setting of the plate spacing was the relative positions of the peaks of the different spectral lines that were normally studied. In particular, it was convenient if the mercury 198 line at λ546.1nm and the λ630nm oxygen line occured about 0.25 of an order apart. This situation enables routine calibration of the FPI to be made between night sky observations without the need to make any plate spacing adjustments.

The actual setting of the plate spacing to the chosen value is a complicated procedure which will only be outlined here. The coarse setting is achieved by use of the micrometer and push rod coupled to the lower FPI mounting plate. The resolution obtainable is only $\pm$ 0.01mm and this measurement may also be subject to some zero-error. This error arises from the procedure used to set the zero of the micrometer by use of the sodium doublet at 589.0 and 589.6nm. These two lines when viewed through the FPI, overlap about every 1000 orders, that is every 0.3mm in spacing. The first overlap occurs at 0.3mm and the FPI spacing is adjusted to give this situation and the micrometer zero is then set relative to this known plate separation. This operation is most readily carried out by observing the interference fringes by eye, which implies that the FPI will be at room temperature. When the

temperature control is turned on and thermal stability has been reached, some expansion in the coupling between the micrometer and FPI plate occurs. This was found to introduce a zero-error of approximately 0.03mm. This operation could not be carried out near the operational separation of 10mm because the width of the sodium lines is so large that overlapping of orders would occur.

The actual movement of the lower plate is achieved by use of the electric motor drive which provides for adjustment to separations of up to 100mm. The circuitry for powering the motor has provision for variable speed drive and also over-travel protection using two micro-switches.

To establish the plate separation that has been set by use of the micrometer requires the use of at least three spectral lines. The relative positions of the fringes of the oxygen lines at λ630nm and λ557.7nm, the mercury line at λ546.1nm and the He-Ne laser line at λ632.8nm were used in this case. These positions used in conjunction with the micrometer reading, readily yield a unique value of separation to within 1nm. The order of interference used for measurements at λ630nm was 32,094.

6.2 Calibration

The calibration of the FPI falls into two phases:firstly the determination of the instrumental profile to enable temperatures to be calculated and secondly the routine separation check. The first of these is carried out periodically and involves the use of both a mercury isotope lamp and a He-Ne laser. The second is carried out about every two hours during observations and utilises the mercury lamp.

6.2.1 Mercury Lamp and He-Ne Laser

A small glass tube containing 2mg of the mercury 198 isotope and argon at 0.26kPa pressure, was obtained from the C.S.I.R.O. National Standards Laboratories. A 160 MHz oscillator to power the lamp was built with a maximum power output of approximately 200mW. This was found to be sufficient power to maintain the discharge, but a high voltage impulse was required to start the lamp. This is far less than other workers have reported because transformer oil was used as the coolant rather than water. The λ546.1nm line was isolated by use of a narrow band interference filter. This line has been extensively studied and the results of Bruce and Hill (1961) and Terrien et al. (1957) were chosen to assign a value to the line width. A value of 0.54 pm was used for the line width to determine the instrumental profile. The mercury lamp, electronics and interference filter were all mounted in a conveniently sized box to allow easy manipulation of the assembly for routine calibration purposes.

The He-Ne laser used is a Metrologic model 360 with a nominal 1.5mW (maximum) output. This was used because the wavelength of the laser line at λ632.8nm was very close to that of the red oxygen line. Comparison of instrumental widths at the mercury and laser wavelengths verified that there was very little difference. For this reason the instrumental profile obtained with the mercury lamp were used in the data analysis. The laser was not used for the routine checking of separation because of doubt about its wavelength stability.

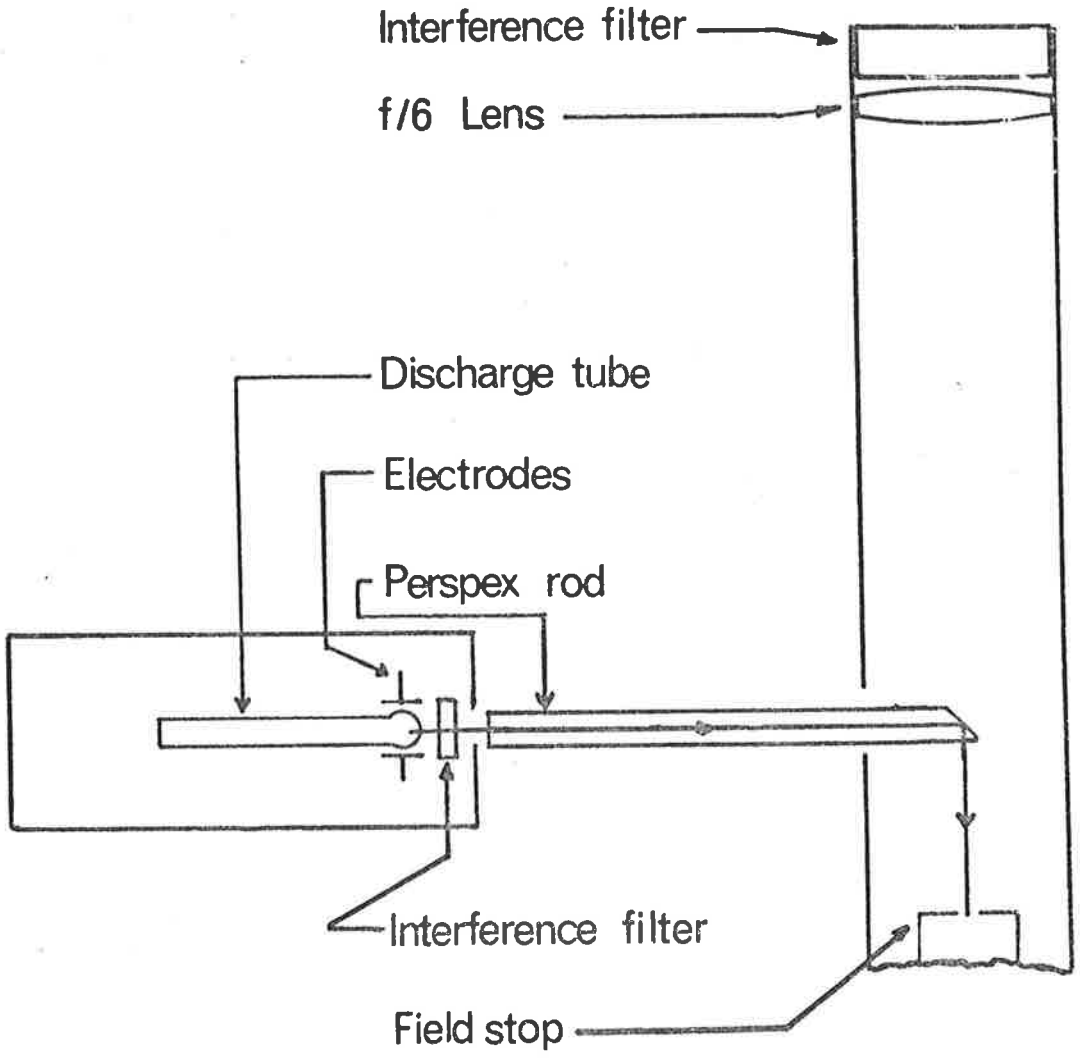

FIG. 35. Schematic diagram of the calibration procedure using the mercury lamp.

6.2.2 Procedure

The procedure for routine calibration with the mercury lamp will be described. The technique for introducing the mercury light into the FPI is illustrated schematically in Figure 35. The light passes through a perspex light pipe and is turned through 90 degrees to be incident on the field stop. The light pipe is poked through the hatch in the periscope and a hole in the side of the FPI main body-work. This arrangement was necessary to avoid the need to remove the λ630nm filter each time a calibration was made. For separation checking it was only necessary to scan through one mercury peak and this was achieved by scanning over approximately 130nm. This scanning range was made to correspond to the first 128 channels of the signal averager, which left the second half of the memory (256 channels) free for storing the airglow scan. If a scan over two mercury orders was required then one simply used the full 512 channels of the averager.

6.2.3 Results

A scan through two orders of the λ546.1nm line is shown in Figure 36. This was made with the FPI in its normal operating condition and indicates an overall finesse of 11.1, when the contribution due to the finite line width is taken into account. This is sufficient for the proposed nightglow measurements and compares favorably with other interferometers reported in the literature (e.g. Roble, 1969).

The recorded function was deconvolved with a gaussian function with half-width of 0.54pm, this being taken as the mercury line contribution. The resultant instrument function was then used for analysis of the airglow results.

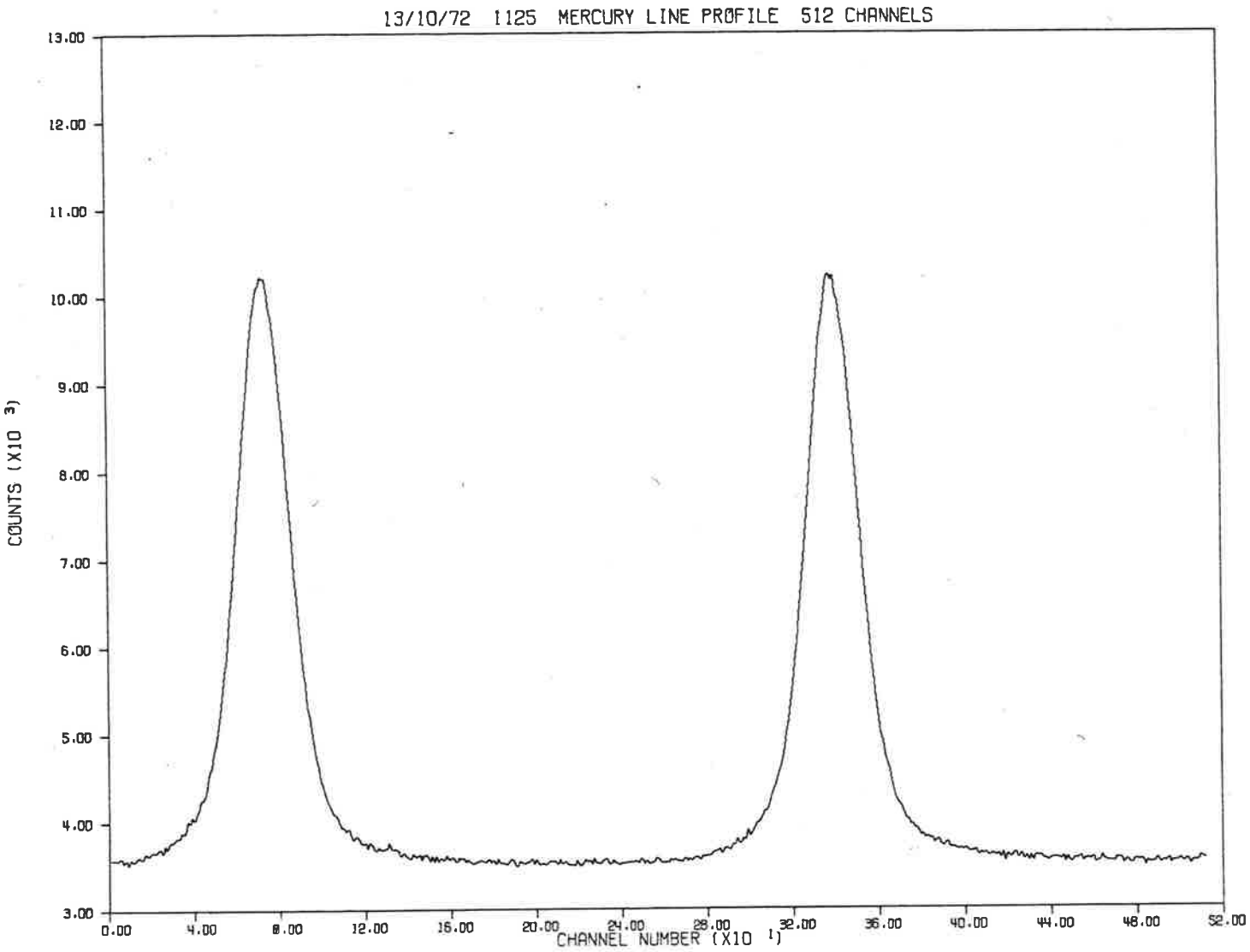

FIG. 36. A scan through two orders of the mercury 198 line, shown as a function of channel number of the signal averager.

6.3 Collection of Results

The airglow λ630nm profiles were routinely recorded at the Mount Torrens field station on every clear night from August 1972 until October 1973. Work is commenced shortly before local sunset when the equipment is switched on and preparation made for the initial calibration. The electronics for the servo controls and the temperature controls are allowed to run continuously and so only the coolant and high voltage for the photomultiplier need be activated.

The hatch in the field station roof is opened and the periscope placed in position. The mercury lamp is then positioned in readiness for the calibration. When the photomultiplier tube temperature is stabilised the calibration is carried out. The separation and parallelism controls may require minor adjustment at this stage.

After the calibration run twilight measurements are made, usually consisting of four measurements made at 50 or 70 degrees zenith angle and azimuth angles 0, 90, 180, 270. The λ630nm emission is usually enhanced during this period and so the averaging time for each measurement is short, typically 15 minutes. This series of measurements is followed by a calibration check to see that the separation control has not drifted. The whole procedure is then repeated with calibrations at two-hourly intervals. The post-midnight λ630nm intensity is usually low and necessitates long accumulation periods, often up to two hours in duration. The particularly long measurements need to be treated with caution because of the possibility of contamination from hydroxyl emissions.

During the progress of a measurement one can check the signal to noise ratio (SNR) that has been achieved by displaying the signal averager memory on an oscilloscope. When the SNR is deemed to be acceptable then the results can be recorded in either of two modes. The first of these is storage on paper tape using a Teletype Model 33. This method is quite slow and very noisy and so the second method which involves recording on magnetic tape is normally used. The cassette recorder used is an International Computer Products Model PI70, which permits data transfer at a rate 10 times faster than the Teletype. During 1973, when the analysis of the results was being carried out the University of Adelaide's facilities for paper tape reading were inoperable and the magnetic tape cassette reading facilities were still in the developmental stage. This situation necessitated the use of the ICL computer in Adelaide to copy the data onto a magnetic tape for analysis on the University's CDC 6400 computer.

6.4 Analysis of Results

A number of computer programs were written to manipulate the data into analyzable form and then to carry out the analysis to obtain doppler temperatures and winds. The manipulating programs were mainly written by the author, but the analysis technique and associated computer programs were all developed by the author's co-worker Mr. P.A. Wilksch. Only a summary will be presented here.

6.4.1 Manipulation of the Data

The data on magnetic tape received from ICL has first to be decoded into a form which is compatible with the CDC 6400. The

software to carry out this operation was developed by Mr. L.A. Kiek, of the University Computing Centre.

The decoded data must then be edited to remove any spurious points or "housekeeping" comments that may have been recorded on the original paper tape. Headings are then inserted before every data block, giving the following information:

(i) date and times of scan start and finish;

(ii) scan duration;

(iii) wavelength under study;

(iv) zenith and azimuth angles;

(v) number of data points in block;

(vi) code indicating detection mode and range settings;

(vii) code indicating that the particular scan may be peculiar in some way.

This information was all in numeric form and in the same format as the data, which made the reading of the labelled data very straight forward.

The data was divided into large blocks representing observations over periods of approximately three months. These large blocks each contained approximately 250 airglow and calibrate scans. To read sequentially through a data block of this size on the computer occupies many seconds of the control processor's time and since long computer jobs are given very low priority, it was decided that a more efficient data retrieval system was necessary.

6.4.1.1 Indexed Sequential Filing System

This type of file can only be created and manipulated on the magnetic disc of the computer, but can be stored on magnetic tape when not in use. An indexed sequential (IS) file is a mass storage file of records stored in logically sequential order that can be accessed randomly by key or sequentially by position. Each scan has a key, which in this case was made to be the heading information described above. This file structure was particularly useful for randomly accessing any desired scan from within the large data blocks, in less than a second of central processor time.

6.4.2 Analysis Technique

The analysis technique used to reduce the airglow data differs from those used by previous workers in this field (Hernandez 1966, 1970; Hays and Roble, 1971 and Feibelman et al. 1972). The main difference being that no attempt is made to assume an analytical form for the instrument function. The instrument function of the Mawson Institute FPI was measured using the mercury lamp and was illustrated in Figure 3.

The function recorded by the FPI is the convolution of the instrument function, I and the source function, G. The deconvolution process required to obtain the source function is performed by use of the Fourier transform. If the Fourier transform of the function I is denoted by F(I) then,

$$F(G * I) = F(G) \cdot F(I)$$

It is clear that the Fourier transform of the source function can

be obtained by dividing the transform of the recorded function by the transform of the instrument function.

The use of this technique of reduction has only been made practical by the advent of the Fast Fourier transform (FFT). The application of the FFT to restoration of astronomical data has been reviewed by Brault and White (1971).

The data reduction method will be described with reference to the schematic diagram in Figure 37. The raw data and the instrument function, I are "inputted" and then transformed to obtain F_i(data) and F_i(I) respectively. The notation F_i(I) is used for the transform of I because it is a discrete Fourier transform. F_i(I) is divided into F_i(data) and F_i(signal) is the result. The power spectra of the functions are shown in each case. Filtering of the data is carried out during the last step by only computing the first 5 to 15 components of F_i(signal) and setting the rest to zero. This is analogous to the method of filtering used by Roble (1971). The number of components used is determined by a test on the SNR of the original data. Brault and White (1971) have discussed the problem of restoring spectra which include noise and also illustrate how a simple restoration without filtering leads to disastrous noise amplification. It was found that even with very heavy filtering that noise amplification was still a problem in the low SNR data obtained from the airglow. Consequently it was decided not to carry out a transform on F_i(signal), but to perform the fitting on F_i(signal) directly. This necessitates the assumption that the source function is gaussian, which has been verified by Zwick and Shepherd (1973).

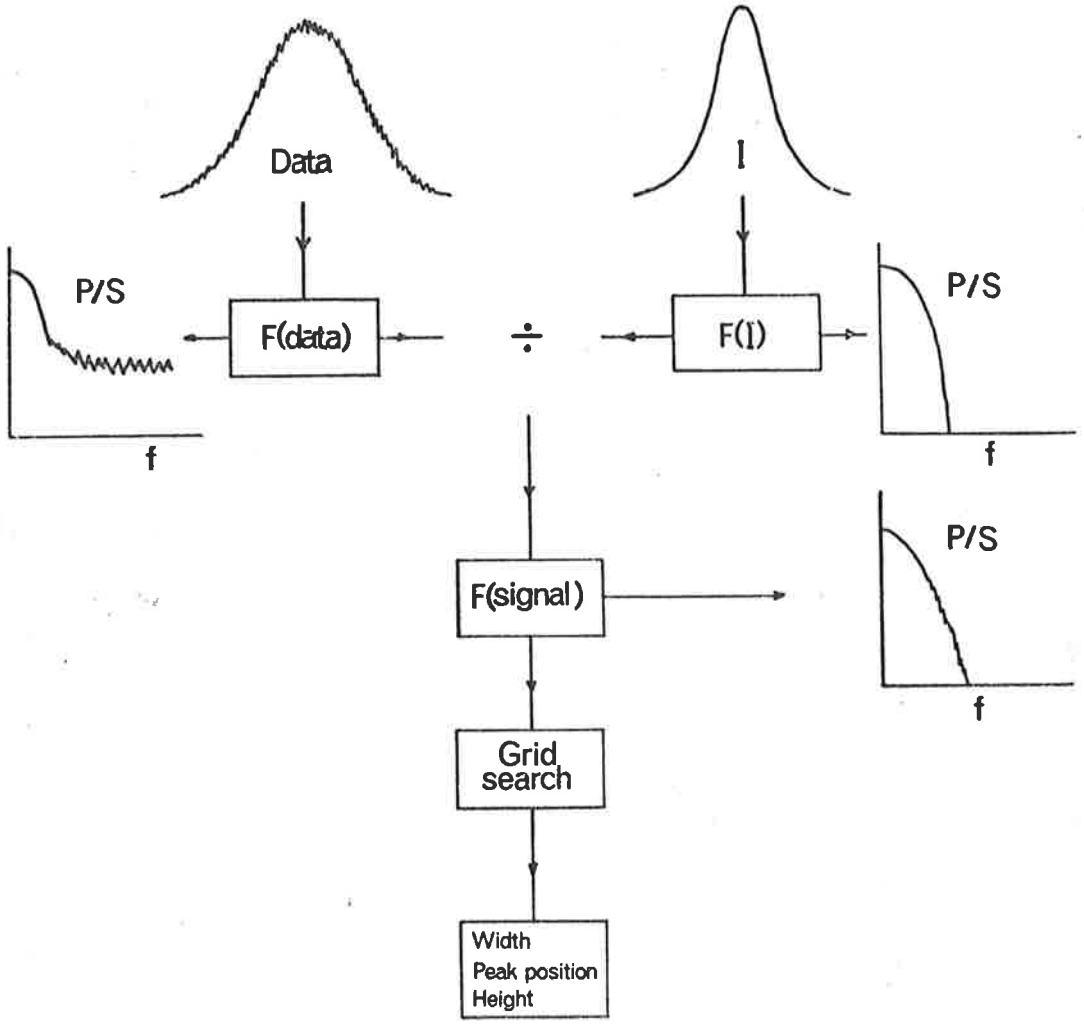

FIG. 37. Block diagram illustrating the analysis of the results. P/S indicates the power spectrum and F the Fourier Transform.

A least squares fit to a gaussian curve is carried out on F_i(signal) using a grid search technique. There are three variables to be determined; the width, peak position and height of the gaussian curve. It is assumed that these are independent of one another and the search performed for each variable in turn. The fitting is achieved by minimising the chi-squared function,

$$\chi^2 = \sum_i k_i (F_i(\text{signal}) - g_i)^2 \qquad (4.2)$$

where g_i is the assumed gaussian curve and k_i is a term determined by two factors. The first of these factors is an estimate of the standard deviation of F_i(signal), which is determined from the average power in the high frequency components, where the spectrum is dominated by noise, under the assumption that the noise is independent of frequency. This term is, therefore a constant for all F_i(signal). The second factor determining k_i is a weighting function which decreases in value as i is increased. This discriminates against the higher frequency components which are noisier and hence less reliable. A normalised form of the chi-squared function, χ^2_ν is obtained by dividing by the number of degrees of freedom, ν which is the number of frequency components used minus the number of variables. As stated above there were three variables in this case. The expected value of χ^2_ν is unity. Minimising 4.2 will in practice yield values of χ^2_ν which are distributed about unity and any large deviation from this value indicates that the function F_i(results) is not purely gaussian or that an incorrect estimate of the noise has been made. In general the values obtained from the λ630nm line profiles were close to unity; but quite large deviations were encountered in some of the twilight measurements because of the sloping background. Bevington (1969) discusses this method of least squares

fitting in chapter 11 of his book and he also considers the problem of determining errors. Following the analysis of Bevington the uncertainty in any one of the three variables is given by the change in that variable required to increase the minimum value of χ^2 by 1.

The computer programs to carry out this analysis were written by Mr. P.A. Wilksch for use on the University of Adelaide's CDC 6400 computer. The output from these programs gave not only temperature, peak position and intensity, but a large number of other parameters including χ^2_ν, background counts, signal power and the results at the end of each iteration. In practice it was found that convergence to the correct width and intensity was fairly slow, because these variables are not completely independent. The convergence to the correct peak position was very rapid because this variable is quite independent of the other two. The average central processor time to analyse one line profile was approximately one second, indicating that this is a very efficient method of analysis.

Details of the results will be presented in Chapter 7.

6.5 Operational Characteristics

The interferometer has now been fully described and a summary of its operational characteristics is given in Table 5, for study of the [01] λ630nm atomic oxygen emission line.

TABLE 5

OPERATIONAL CHARACTERISTICS OF THE MAWSON INSTITUTE

FABRY-PEROT INTERFEROMETER AT λ630nm

1. Etalon

(a) Supports - Stacks of piezoelectric discs
Upper FPI plate - Two disc stack
Lower FPI plate - Ten disc stack,
coefficient : 4.5nm/volt
Range of movement : 300nm

(b) Plates Fused silica
Thickness : 25.4mm
Diameter : 150mm
Clear aperture : 150cm^2
Spacing : 10.110mm
Parallelism: automatically controlled to better than 5nm
Separation: automatically controlled to better than 1nm for a bandwidth of 2Hz

(c) Coatings Silver : 30nm
Magnesium Fluoride : λ/4 at 356nm
Cerium Oxide : λ/4 at 500nm
Reflection coefficient : 93.9%
Transmission coefficient : 5.1%

2. Finesse and Peak Transmission

	Finesse	Peak Transmission
Reflective (A)	50	0.72
Defect (D)	17.5	0.32
Etalon (A*D)	16.5	0.23
Aperture (F)	15.5	0.8
Instrument (A*D*F)	11.1	0.18

3. Input Optics

(a) First lens: Single Component 150mm, f/6
(b) Interference filter Bandwidth: 0.35nm
Transmission: 47%
(c) Field stop. Diameter: 4mm
(d) Objective lens. Three component 900mm f/6.

TABLE 5 Continued:

4. Output Optics

(a) Output lens: Single component 300mm, f/2.
(b) Hirschfeld cone. Lens surface 15mm, f/1.
Quantum efficiency enhancement: 2 times

5. Photomultiplier

EMI 9558B Serial Number 10016.
Cathode sensitivity 194μA/ℓm
at gain to produce 200A/ℓm
Temperature: -30°C
Dark counts: 6 sec^{-1}
Standard deviation of dark
counts/second: 4

6. Recording of Data

(a) Signal averager

Nuclear Data Model 1100
Number of channels used: 256
Scan duration: 10 sec

(b) Teletype Model 33

Recording rate: 256 channels
of data in 3.4 mins.

(c) Digital Cassette Recorder

International Computer Products
Model PI 70
Cassette: Philips type
Recording rate: 256 channels
of data in 20 secs.

CHAPTER 7

THERMOSPHERIC TEMPERATURES AND WINDS

7.1 Introduction

In this chapter the kinetic temperatures and neutral winds measured with the Mawson Institute FPI, from the Mount Torrens field station, will be presented.

Measurements made by other workers using the same technique will be reviewed and compared with the Mount Torrens results. Comparison will also be made with measurements obtained by other methods, for example incoherent scatter radar.

7.2 Review of Earlier Observations

7.2.1 FPI Measurements

7.2.1.1 Temperatures

The FPI appears to have first been applied to the study of the aurora by Babcock (1923). The aim of his investigation was primarily to determine the wavelength of the green oxygen line at λ557.7nm. After Babcock's pioneering effort very little use of the FPI in airglow studies was reported until the 1950's when renewed interest became apparent. This was due to the work of Jacquinot and Dufour (1948) and Chabbal (1953), in carrying out extensive experimental and theoretical studies of the instrument. The advent of photomultiplier tubes and later the S20 photocathode, made accurate measurement of line width feasible. The results obtained using photographic detection have since been shown to be very dubious, particularly for the dayglow measurements attempted by Jarrett and Hoey (1963). The first width measurements on the [OI] λ630nm line were reported by

Cabannes and Dufay (1955) and Phillips (1955), in each case using photographic detection. The first usage of a photoelectric FPI was reported at the same time by Armstrong (1955), in the study of the [oI] λ557.7nm line. This paper was followed over the next few years by a spate of reports from Armstrong (1959), Mulyarchik (1959), Wark (1960), Nilson and Shepherd (1962), and Turgeon and Shepherd (1961). These measurements dealt mainly with auroral and airglow λ557.7nm measurements because these sources were much brighter than the corresponding λ630nm emission. The observations referred to so far were mainly of a preliminary nature and have been included for historical interest.

The first systematic λ630nm airglow observations were made by Jarrett et al. (1964), with a 70mm clear aperture, pressure scanned FPI. They reported pronounced temperature variations throughout the night and attributed this to the patchiness of the λ630nm emission layer.

Bens et al. (1965) attempted to measure the width of the red line in the day glow by use of a double-étalon FPI. They claim that the temperature deduced is in excess of 1200°K. Satellite observations of the day glow λ630nm line width using a spherical FPI have been reported by Blamont and Luton (1972). The aperture of this instrument is 2mm, which is too small to permit night airglow observations.

Investigation of the diurnal variation of the apparent thermospheric temperature and comparisons with empirical models (Jacchia, 1965 and 1970), have since been carried out by Biondi and Feibelman (1968) and Feibelman et al. (1972). These results are of particular interest and will be discussed in more detail when the Mount Torrens

data is presented.

The use of a FPI to study the SAR arc of October-November, 1968 has been reported by Hays et al. (1969), Roble (1969) and Roble et al. (1970). They concluded that there was no measurable neutral gas temperature increase within the arc. Hernandez (1972) in studying the SAR arc of March 8-9, 1970 reports a 100K temperature increase within the arc which is much larger than that predicted by Roble and Dickinson (1970). He attributes this to the peak emission of the λ630nm line being somewhat elevated to near 500km. Measurements made when the peak emission was near 400km, show no temperature variation and this is consistent with Roble's theory and results. Armstrong and Bell (1970) also measured temperatures during the October 1968 magnetic storm and have compared these with the results of Hays et al. (1969). Marked differences between these two sets of results are apparent for which Armstrong and Bell have not ventured to give an explanation, because they may be due to instrumental effects.

7.2.1.2 Winds

Very little work has been reported on the doppler shift of the λ630nm line because of the very stringent stability requirements on the instrumentation. A preliminary measurement was made by Biondi and Feibelman (1968) which indicated an eastward wind of 400ms^{-1} just after sunset. This wind is in the same direction, but considerably larger than those observed by Armstrong (1969), who detected a number of winds during 1968. There have been no other reports of winds in the airglow, but Hays and Roble (1971) made measurements of winds in a SAR arc and in an aurora. They observed southward winds with velocities between 250 and 400 ms^{-1}.

These results represent the whole of the published work on doppler shifts of the λ630nm line and there is clearly a need for more work in this area.

7.2.2 Measurements by other Methods

7.2.2.1 Satellite Observations

The neutral winds in the thermosphere have been deduced from slight changes in the inclination of satellites' orbits to the equator (King-Hele, 1964 and King-Hele et al, 1970). The results indicate that the upper atmosphere at 250km rotates faster than the earth by approximately 100m/s, in an eastward direction. As Armstrong (1969) points out, this eastward rotation is an average result and so comparison with winds deduced from doppler shifts of λ630nm should be treated with caution. He concludes that there is no obvious conflict between the results.

The decay of perigee height of satellites due to atmospheric drag can be used to determine average density scale-heights. (King-Hele, 1962). The temperatures can be deduced under the assumption that diffusive equilibrium exists. Once again these are average results and hence of limited value for comparison with doppler temperatures.

7.2.2.2 Chemical Releases

Temperatures can be deduced by measurement of the thermal broadening of resonance lines of chemical impurities released during twilight from rockets. (Blamont and Lory, 1964). Study of contaminant releases can also give information about winds in the upper atmosphere (Kochanski, 1964 and Bedinger, 1970).

These measurements are very limited in quantity, but do represent direct measurement of temperature and wind, as distinct from the mean values obtained from satellite observations.

7.2.2.3 Thomson Scattering

Incoherent scatter radar measurements of electron and ion temperatures and motions have been reviewed by Evans (1969, 1972).

Direct comparisons between the radar and doppler temperatures made by Hays et al. (1970) and Cogger et al. (1970) indicated agreement to within the uncertainties of measurement. This is a very encouraging result for both radar and FPI users and has been used by Cogger et al. (1970) to caste doubt upon Langmuir probe electron temperature measurements made by Carlson and Sayers (1970).

This measurement technique is superior to the doppler method in being capable of better time resolution and also 24 hour operation, which has not yet been achieved with an FPI. On the other hand, the radar installation is much more complex and expensive than the FPI.

7.2.2.4 Michelson Interferometer

The wide-angle Michelson Interferometer mentioned in Chapter 2 (Hilliard and Shepherd, 1966) has been recently applied to the study of λ630nm auroral emission by Zwick and Shepherd (1973). They emphasize that this technique is not useful when λ630nm intensities are less than 200 rayleighs because of the contamination from the hydroxyl lines. The temperature values presented range from 810 to 1440K which will be shown to be consistent with those presented later in this chapter.

Zwick and Shepherd (1973) report that the O'(D) atoms appear to be thermalized before emission and claim that a 5 percent non-thermal component would have been detectable. This is an important conclusion because it has been assumed throughout this work that the oxygen atoms are thermalized before emission.

7.3 Results Obtained at Mount Torrens

Observations on the λ630nm line in the night airglow were made from August 1972 until September 1973. The observing site was at Mount Torrens (an elevation of 590m) near Adelaide, at geographic coordinates 34° 52.2'S, 138° 56.6'E. The local topography is ideal for nightsky studies, providing a clear horizon in all directions and freedom from background due to city lights.

In addition to the FPI at the field station, there were two twin-channel photometers (Schaeffer, 1970) and a three-component flux-gate magnetometer. The photometers were used to monitor the intensity of the two atomic oxygen lines λ630nm and λ557.7nm.

The procedures for collection of results and calibration of the FPI have been described in Chapter 6.

7.3.1 Contamination by Hydroxyl Emissions

The possibility of contamination of the λ630nm measurements by the hydroxyl emissions has already been briefly referred to in Section 6.1 when the selection of the order of interference was discussed. Armstrong (1969) carefully considered this problem for the three hydroxyl lines in the 9-3 band at 628.76nm ($P_1(2)$), 629.87nm ($P_2(3)$) and 630.68nm ($P_1(3)$). These wavelength values are

those quoted by Chamberlain (1961) and are based on theoretical work of that author and observations made by Kvifte (1959). Armstrong (1969) asserts that only the $P_1(3)$ line is important and that its effect can be minimised by careful selection of the order of interference. The operating order is chosen so that the λ630nm and the $P_1(3)$ line are separated by more than 0.25 of an order. Armstrong (1969) chose an order of 17,500 which corresponds to a free spectral range of 0.036nm. Assuming that the oxygen line wavelength is well known, this implies that the wavelength of hydroxyl $P_1(3)$ line needs to be known with an accuracy of better than $\pm$ 0.01nm. The higher order of interference chosen for the Mawson Institute FPI necessitates an even more accurate knowledge of this wavelength. It is felt that the uncertainties in Chamberlain's values of the wavelengths are greater than the limits mentioned above. This implies that choice of the order of interference using the $P_1(3)$ and $P_2(3)$ wavelengths given by Chamberlain, would be pointless. This is not a serious problem, however because both the $P_1(2)$ and $P_1(3)$ lines are greatly attenuated by the interference filters used. The $P_2(3)$ line, however is passed by the interference filter. It has an intensity of about 2 Rayleigh according to Zwick and Shepherd (1973); citing a private communication with E.J. Llewellyn. This implies that measurements made when the λ630nm line was less than about 20 rayleighs, could be suspect.

A report of measurements of the wavelength of the hydroxyl lines $P_1(3)$ and $P_2(3)$ by Hernandez (1974) was received by the author

at the time of writing this thesis. The values given for the $P_1(3)$ and $P_2(3)$ lines are 630.6837 ± 0.0009nm and 629.7992 ± 0.0004nm respectively. At the order of interference used for the observations presented here the $P_2(3)$ line would be displaced by approximately 0.2 of an order at λ630nm. This means that the choice of order was somewhat fortuitous and that contamination from the $P_2(3)$ line will be insignificant.

7.3.2 Kinetic Temperatures

The atomic oxygen line at λ630nm results from excitation of the atom to the ^1D level. The mean lifetime of this level is 110 seconds which ensures that at the time of emission the oxygen atoms are in thermal equilibrium with the surroundings. The temperatures determined from the doppler broadening of the λ630nm line are therefore representative of the F region.

The line profile shown in Figure 38 is representative of those obtained in the twilight. It was recorded on 29 May 1973 and indicates a temperature of 800 ± 20K and a 110 ± 25ms^{-1} eastward component of the wind. A line profile obtained later in the same night is shown in Figure 39 and reveals a temperature of 800 ± 50K and an eastward wind component of less than 30ms^{-1}. The latter profile took nearly 10 times longer to accumulate because of the low intensity of the λ630nm emission in the early morning hours during winter. These results are typical of those obtained in the latter part of the observation program after all the refinements had been made to the detection system.

7.3.2.1 Diurnal Variation

The diurnal variation of the thermospheric temperature has been

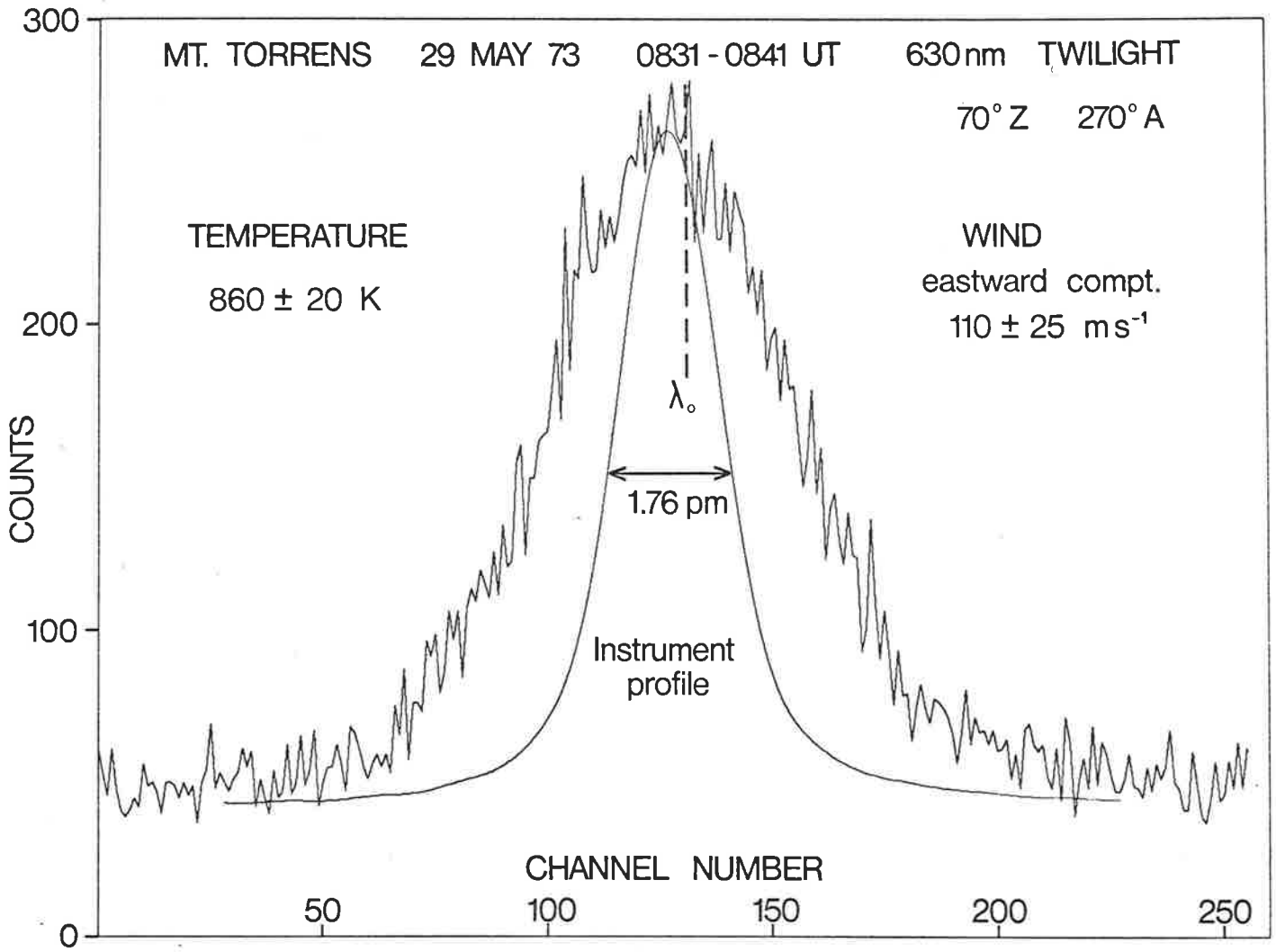

FIG. 38. A λ630nm line profile obtained during twilight and the instrument profile are shown. The λ630nm line is displaced from the zenithal position, λ_o and indicates an eastward wind of 1100ms^{-1}.

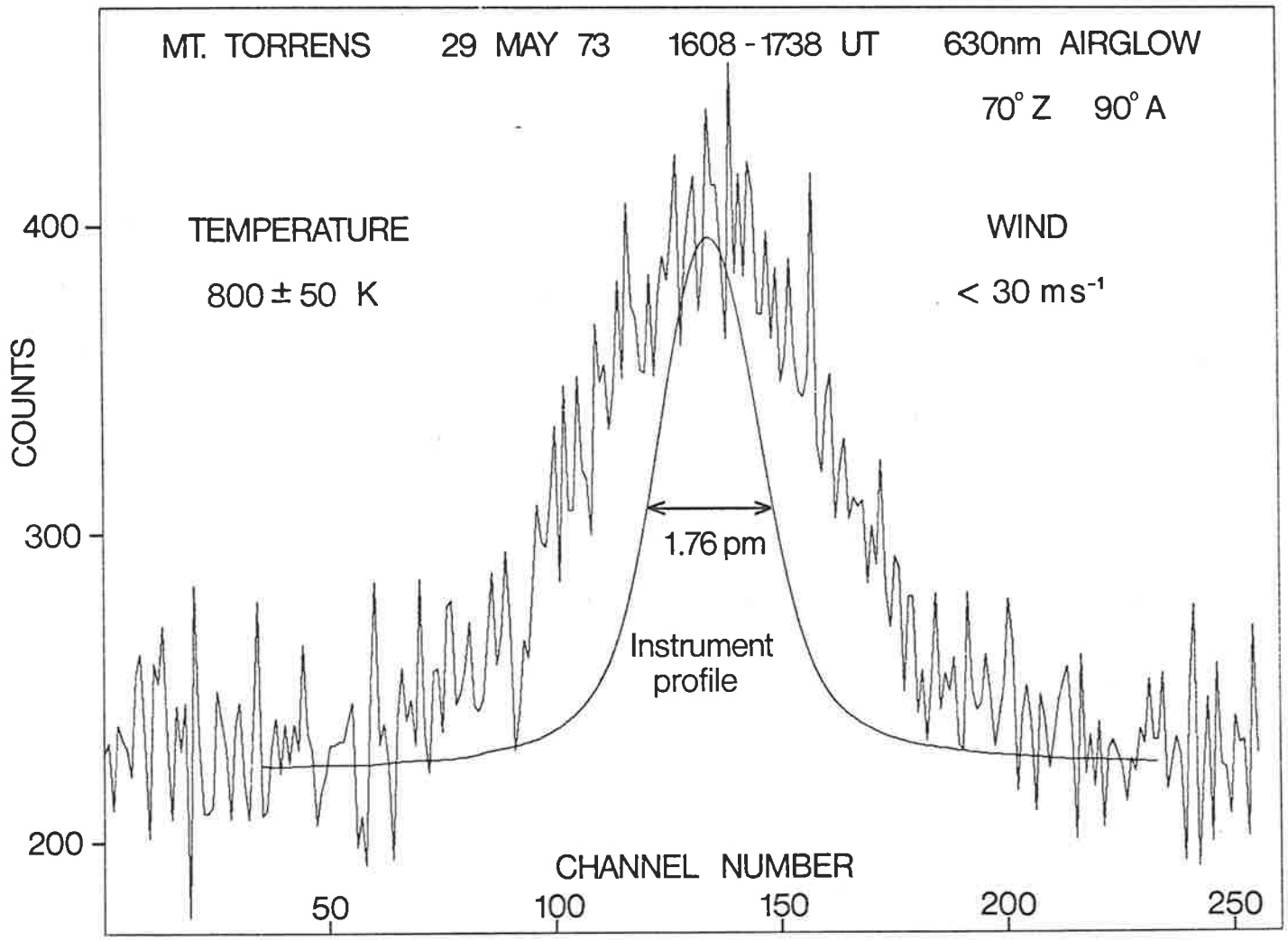

FIG. 39. A λ630nm line profile obtained in the early morning hours during the winter. The emission intensity was very low and required a long averaging time, namely 90 minutes.

the subject of both experimental and theoretical study for a number of years. Observations using Thomson scattering (McClure, 1971) have yielded much data on this subject. Feibelman et al. (1972) have also reported some results obtained from Fabry-Perot interferometer studies of the λ630nm line. They have compared these with the temperatures calculated using Jacchia's (1970) model. The agreement is found to be rather poor, but no modification to the model was suggested.

Figure 40 illustrates the temperature variation as a function of time during a magnetically quiet night at Mount Torrens. Local midnight is at 1430 UT and is marked on the graph. The letters N,S,E,W enclosed in circles indicate observations to the north, south etc; the vertical lines represent the uncertainty in the measurement and the horizontal lines represent the length of time for the observation. From this graph, it is clear that the uncertainty in the temperature varies throughout the night from as little as ± 20K for twilight measurements, to ± 60K for early morning results. In an attempt to illustrate that this result is characteristic of all the data obtained, the temperatures obtained to the north of Mount Torrens over a 10 month period are all plotted as a function of universal time (Figure 41). The decrease in temperature after sunset is quite apparent and the minimum temperature appears to occur at approximately 1700 UT. These gross features of the diurnal variation are quite consistent with other observations (McClure, 1971 and Feibelman et al, 1972) and with the models (Jacchia, 1970).

The rapid change of temperature in the post-sunset period reported by Feibelman et al. (1972) is not observed in the Mount Torrens data. The maximum rate of change observed is approximately 100K/hr which is considerably less than the 200K/hr reported by

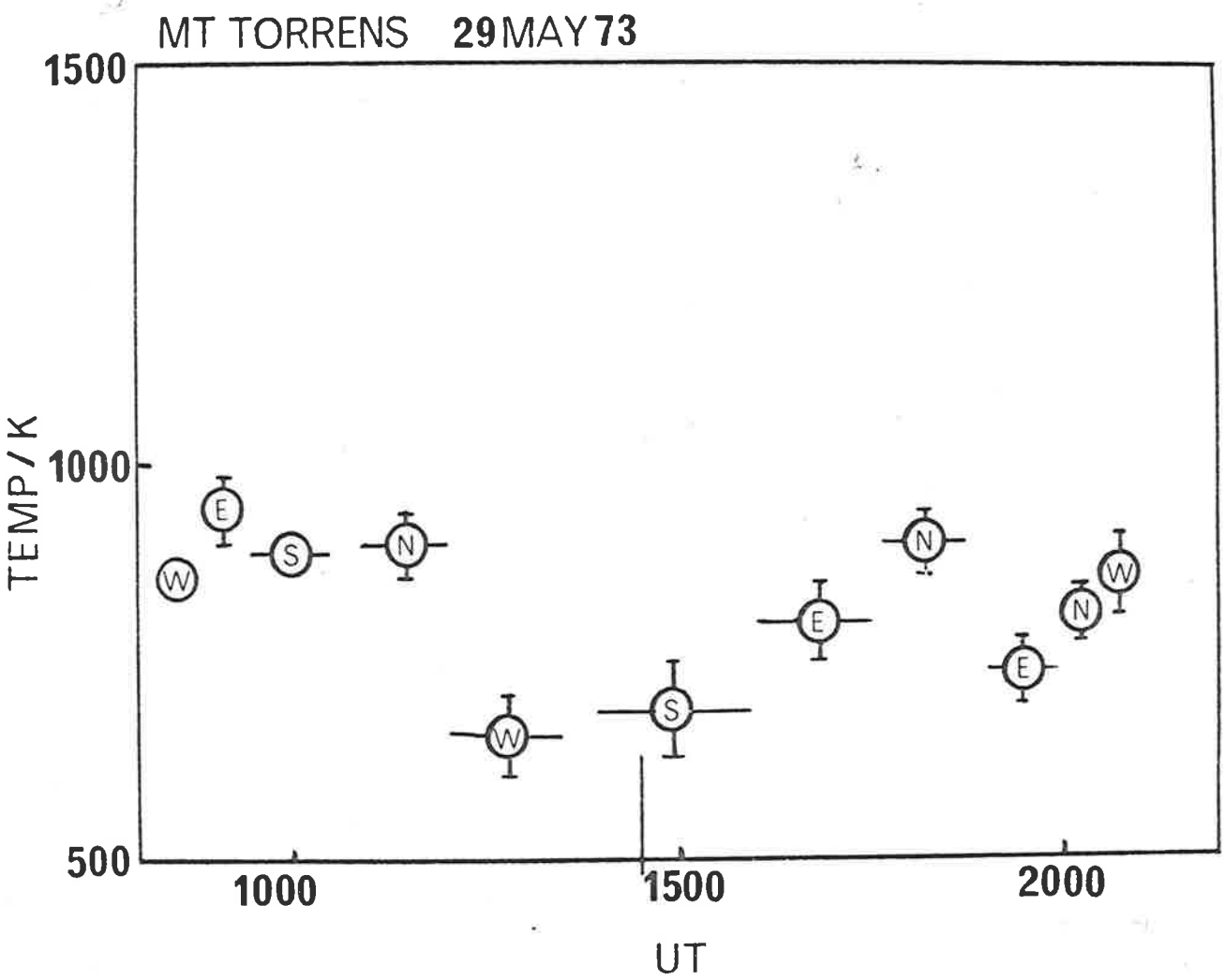

FIG. 40. Doppler temperatures observed from Mount Torrens on the night of 29 May 1973. The letters, N,S,E and W refer to the azimuthal direction of observation being to the north, south, etc. The measurements were all made at a zenith angle of 70°.

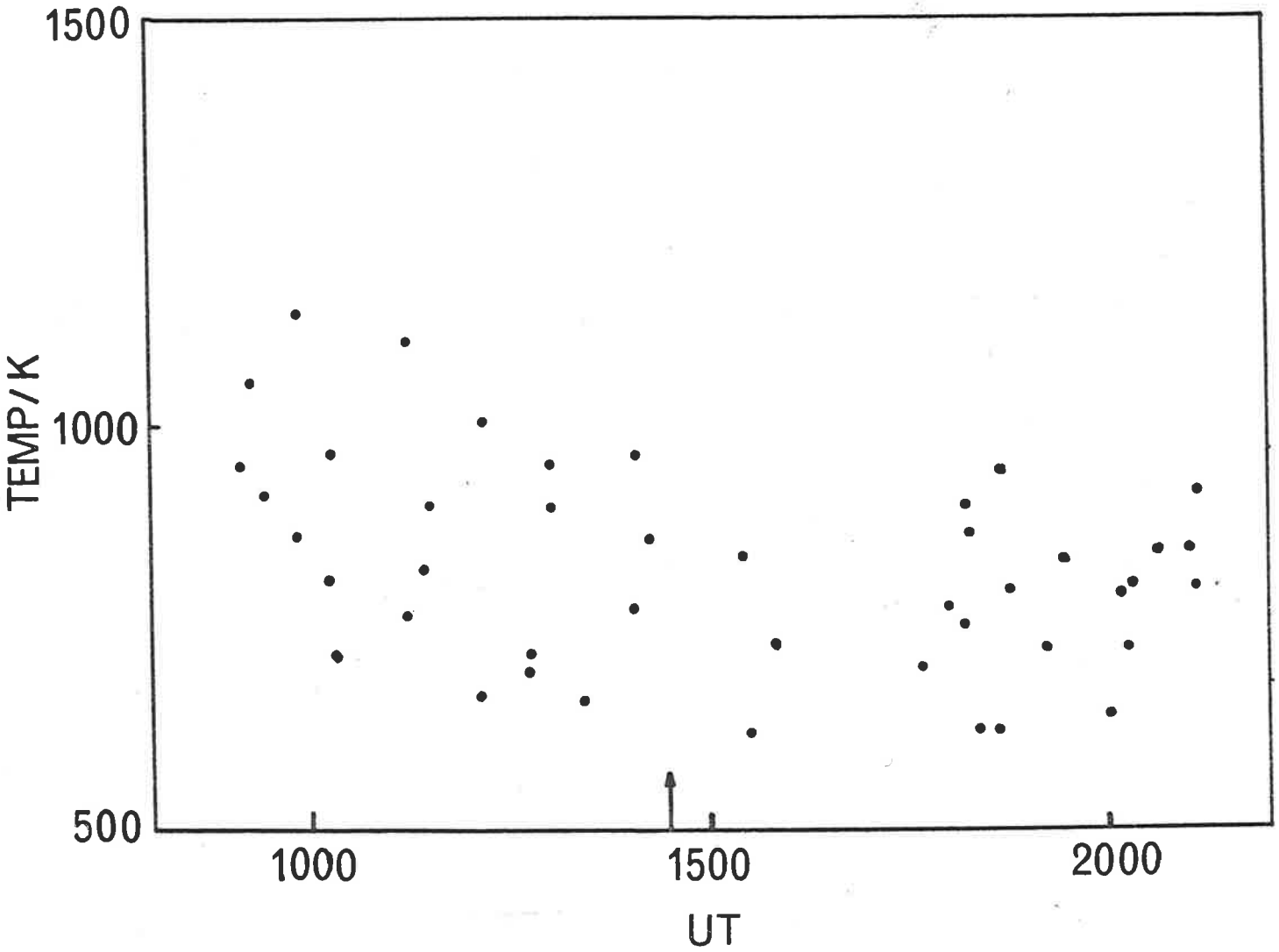

FIG. 41. Diurnal variation of λ630nm doppler temperatures measured to the north of Mount Torrens at a zenith angle of 70°. These results were obtained during the period December, 1972 to September, 1973 when the magnetic activity was low. The arrow on the time axis indicates local midnight.

Feibelman et al. (1972). It is agreed, however, that the 30K/hr predicted by the Jacchia model is too small.

7.3.2.2 Dependence on Magnetic Activity

The dependence of the thermospheric temperature on the level of magnetic activity has been the subject of extensive study. The level of magnetic activity is usually indicated by the magnitude of the K index (Rostoker, 1972). A strong correlation between the thermospheric temperature and K index has been observed. A number of moderate magnetic disturbances occured during the observations which enabled this conclusion to be reached.

The doppler temperatures for 23 February 1973 shown in Figure 42 are a good illustration of the temperature enhancements obtained during a magnetic disturbance. K indices from Toolangi (near Melbourne) for this night ranged from 4+ to 6- . The magnetometer at Mount Torrens indicated sudden commencements at 1200 and 1600 UT, each of which was accompanied by enhancements in the temperature.

Comparison of this night with 29 May 1973, shown in Figure 40 dramatically illustrates the dependence of temperature on the level of magnetic activity.

The limited value of the geomagnetic indices for the study of individual events has been pointed out by Rostoker (1972). For this reason, the dependence of temperature on K index will be shown by use of a body of data collected on a large number of nights. Temperatures measured to the south from Mount Torrens, in the period December 1972 to September 1973 are shown in Figure 43 as a function of K index. A similar form of illustration has been used by Trutse and Yurchenko (1971), for temperature measurements made in the aurora. Their results

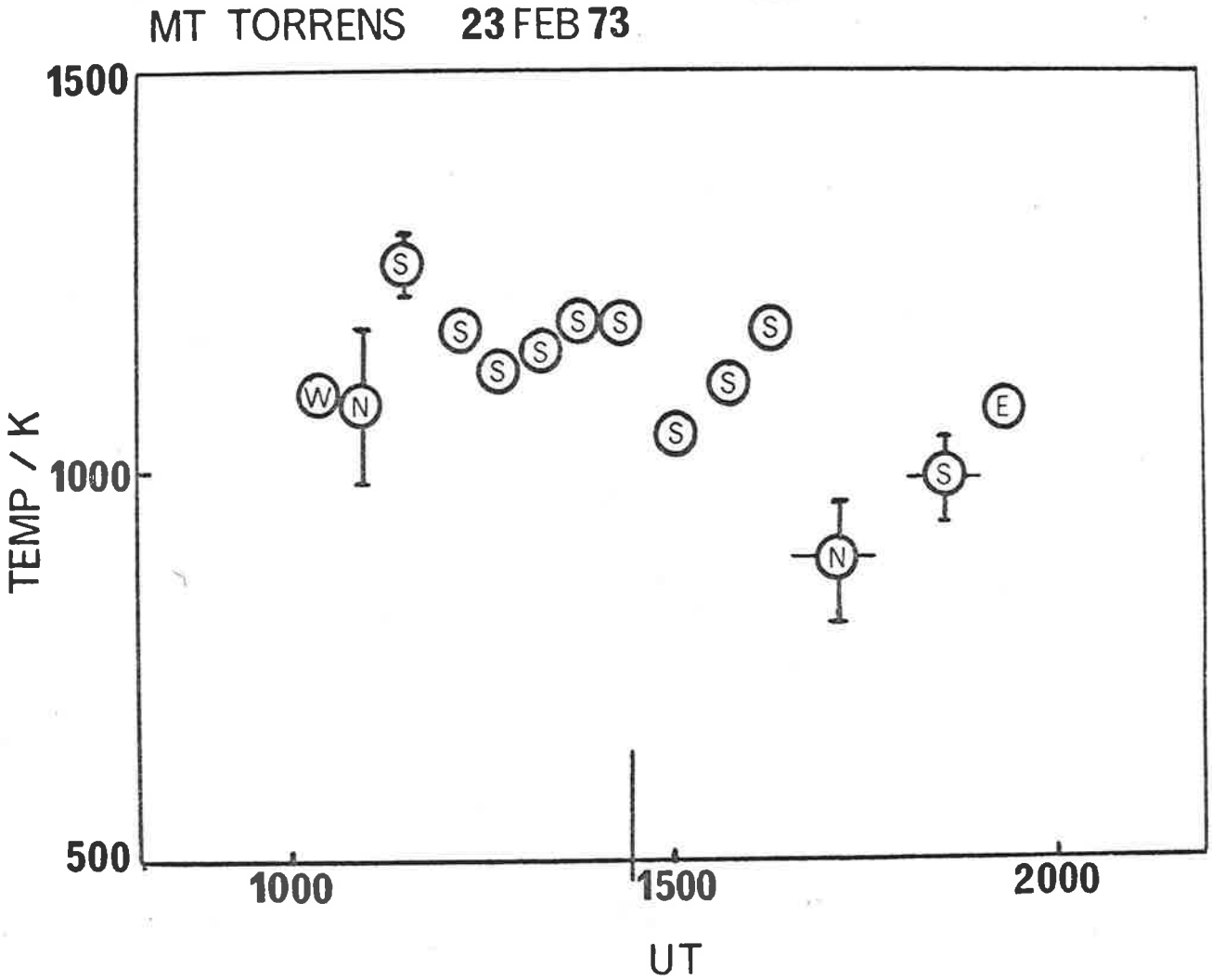

FIG. 42. λ630nm doppler temperatures during a magnetic disturbance, on the night of 23 Feb 1973.

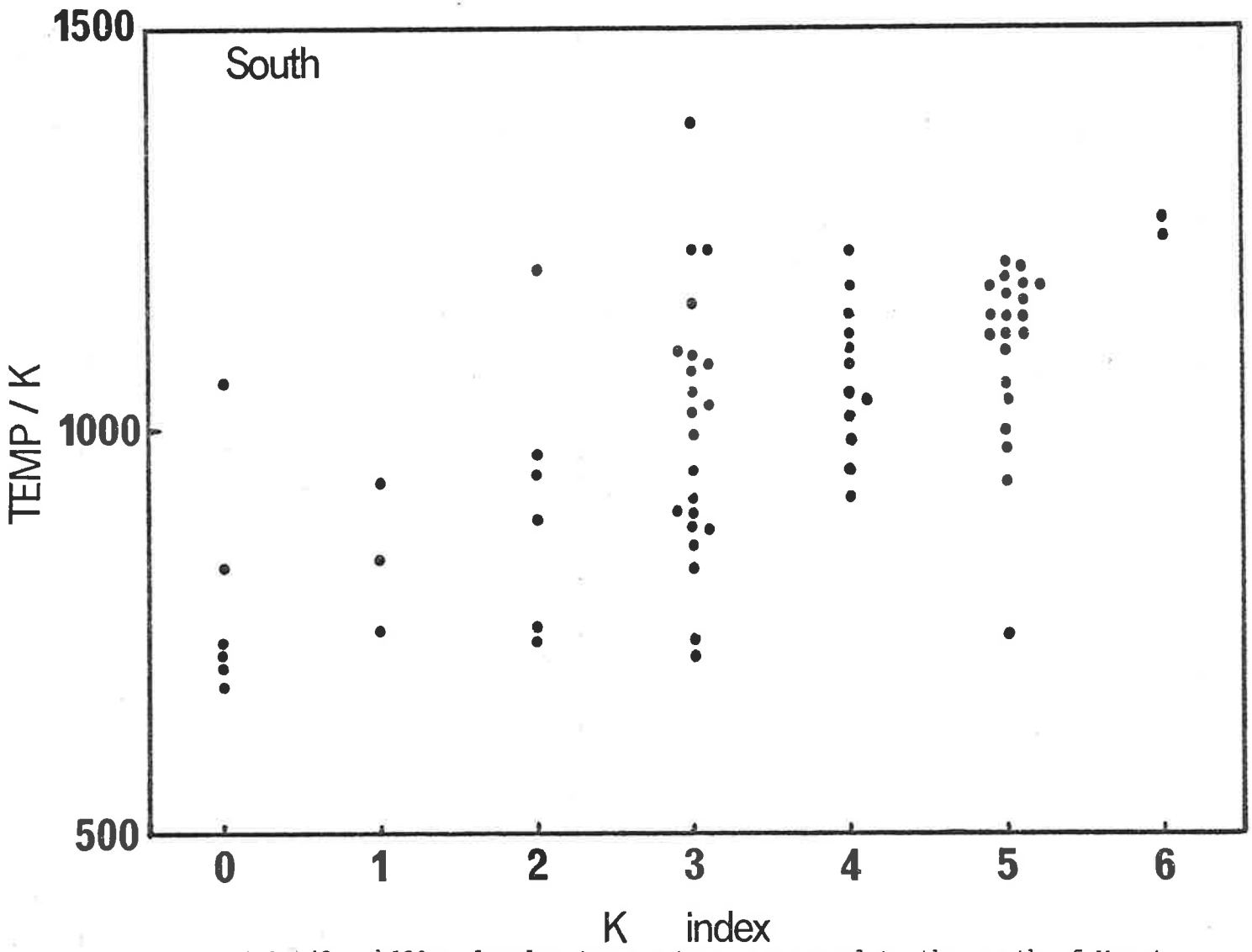

FIG. 43. λ630nm doppler temperatures measured to the south of Mount Torrens as a function of K index (Toolangi).

are in good agreement with those shown in Figure 43.

7.3.3 Neutral Winds

The neutral wind measurements made from Mount Torrens during the period from August 1972 to September 1973 represent the largest body of data obtained by this technique. The only other significant results published are those of Armstrong (1969) which cover a period of four months during 1968. Hays and Roble (1971) have reported wind measurements made during two magnetic storms.

The results will be divided into two groups for the purposes of presentation; the first being those obtained during periods of low magnetic activity and the second will consist of those obtained during magnetic disturbances. The periods of magnetic disturbance were distinguished by λ630nm intensity enhancements in the south and were also correlated with increases in the K index to 4 or more.

7.3.3.1 Diurnal and Seasonal Variation

The study of the diurnal variation of the neutral wind is carried out using data obtained during periods of low magnetic activity. The winds are presented in two groups, the meridional (north-south) component and the zonal (east-west) component. Each line profile obtained yields a measure of one of these components because the directions of observation were restricted to north, south, east and west. Observations made in the zenith were carried out periodically and it was assumed that these measurements represented the line profile with negligible doppler shift. The vertical component of the wind has been reported to be only a few ms^{-1} (Dickinson et al, 1968) which supports this assumption.

The zonal and meridional wind components measured during periods of low magnetic activity are shown in Figure 44(a) and (b) respectively, as a function of universal time. These results were obtained on 20 nights in the period December 1972 to September 1973. As for the kinetic temperatures, the uncertainties in the wind measurements are quite variable. Typically, the uncertainties range from $\pm$ 10ms^{-1} when the λ630nm intensity is enhanced, to $\pm$ 50ms^{-1} during periods of low intensity.

The meridional component in Figure 44(b), indicates a pronounced diurnal variation. The wind is equatorward for most of the night, with some evidence to suggest that it reverses to poleward during the day. The variation is consistent with previous observation and models of thermospheric wind systems. Armstrong (1969) presents a number of measurements of the meridional component, mainly in the time interval 1500 to 2000 UT. They are predominantly equatorward and rarely exceed 100ms^{-1} in magnitude. This is in good agreement with the corresponding results shown in Figure 44(b).

The zonal component is predominantly eastward in the post-sunset period changing to westward in the morning. From 1200 to 1800 UT there is roughly equal probability of eastward or westward winds. If the data in this time interval is masked out then the result is very similar to that presented by Armstrong (1969). It was felt that the lack of systematic behaviour of the data during the 1200 to 1800 UT interval may be due to a seasonal variation of this component of the neutral wind. The zonal wind component in this time interval was, therefore graphed as a function of the time of the year, as shown in Figure 45. This representation clearly indicates that the winds are predominantly westward in summer, reversing

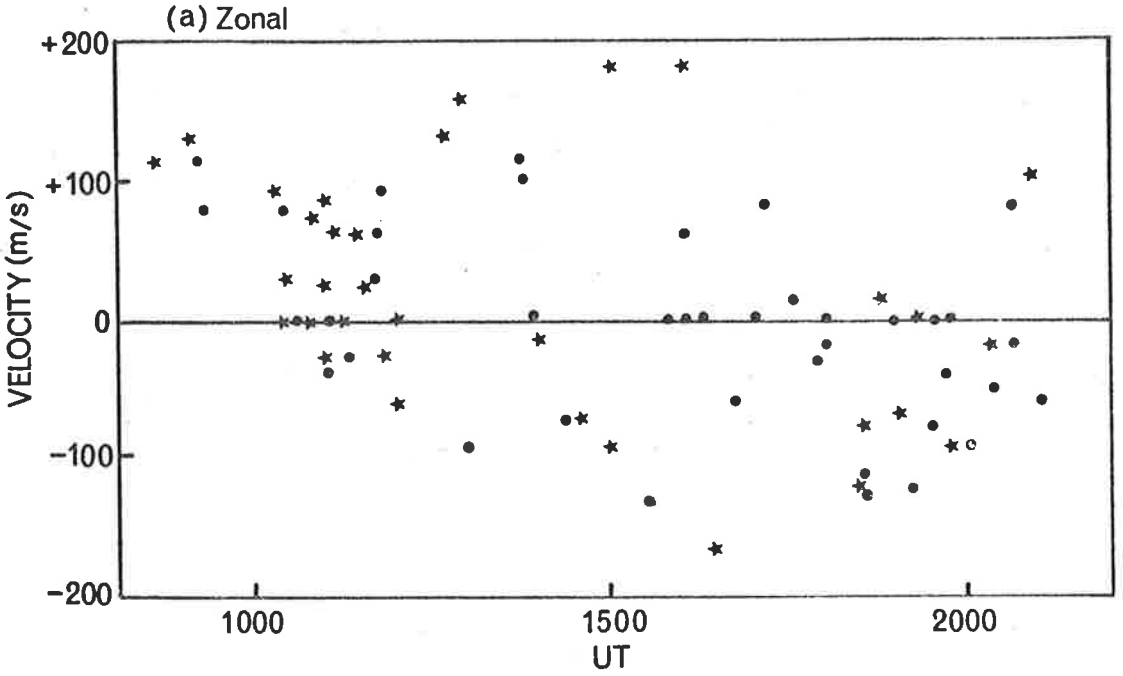

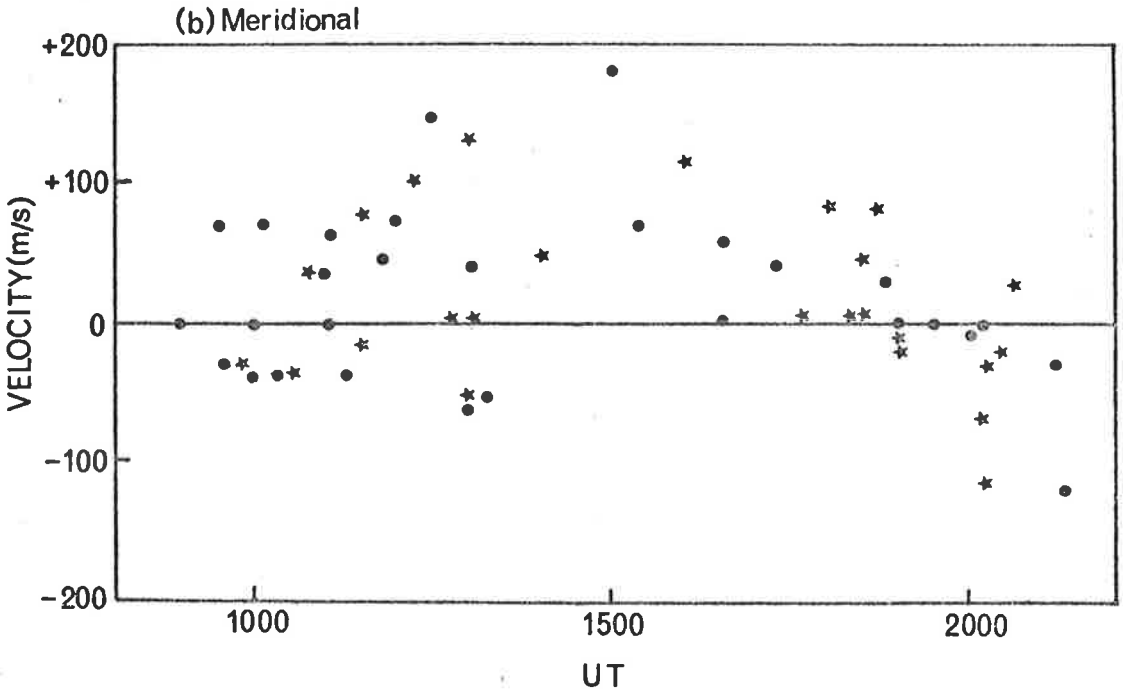

FIG. 44. Neutral winds as a function of universal time, during periods of low magnetic activity. The observations were made at a zenith angle of 70°. (a) Zonal component, deduced from measurements in the east (•) and west (*). Positive velocities are eastward. (b) Meridional component, deduced from measurements in the north (*) and south (•). Positive velocities are northward (equatorward).

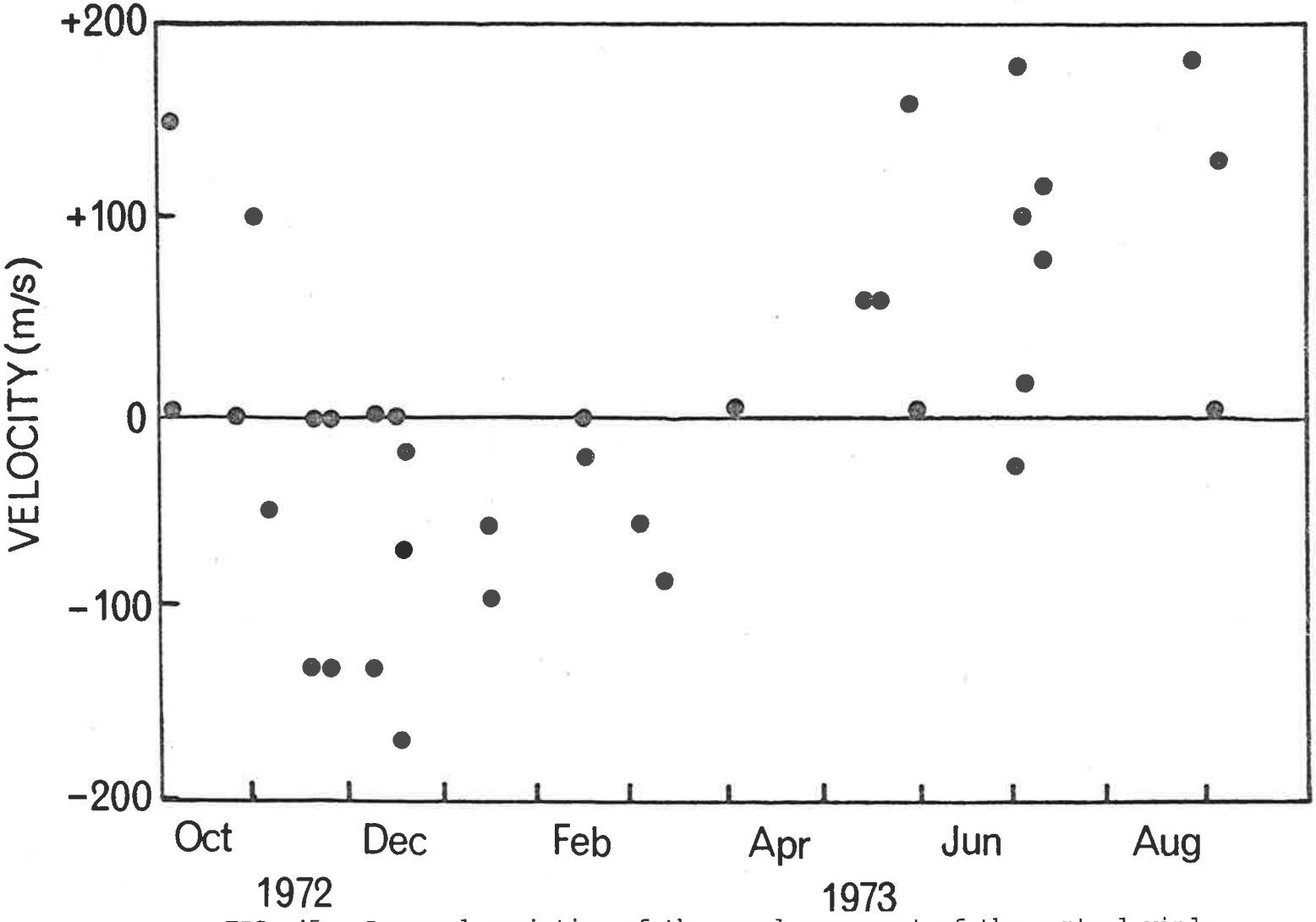

FIG. 45. Seasonal variation of the zonal component of the neutral wind. The zonal component measured in the time interval 1200-1800 UT is shown as a function of the time of the year.

to eastward in winter. The diurnal variation of the zonal component of the wind is apparent when the results for summer and winter are graphed separately, as shown in Figure 46 (a) and (b). In the summer months the post-sunset eastward winds are very short-lived and after 1200 UT the wind is predominantly westward. In the winter the evening eastward winds continue throughout the night and show some evidence of reversal to westward at about 1900 UT.

The same presentation was also used for the meridional component and is shown in Figure 46(c) and (d). This component does not appear to have any obvious seasonal variation. The observations during the winter months extend over a longer time interval and therefore show more evidence of the day-time poleward winds.

It was not possible to establish the diurnal behaviour of either component, during equinoctial months because of the lack of data during these periods.

7.3.3.2 Winds During Magnetic Disturbances

During the 12 months of observation there were 12 nights which have been classed as being magnetically disturbed. These all occured in the summer months from December 1972 to April 1973.

The zonal and meridional components of the neutral wind measured on these nights, as a function of universal time are shown in Figure 47(a) and (b), respectively.

It is of interest to compare the measurements of the zonal component with those shown in Figure 46(a), showing the diurnal variation in the summer. The diurnal pattern in the two cases is very similar, except that for the magnetically disturbed nights, the

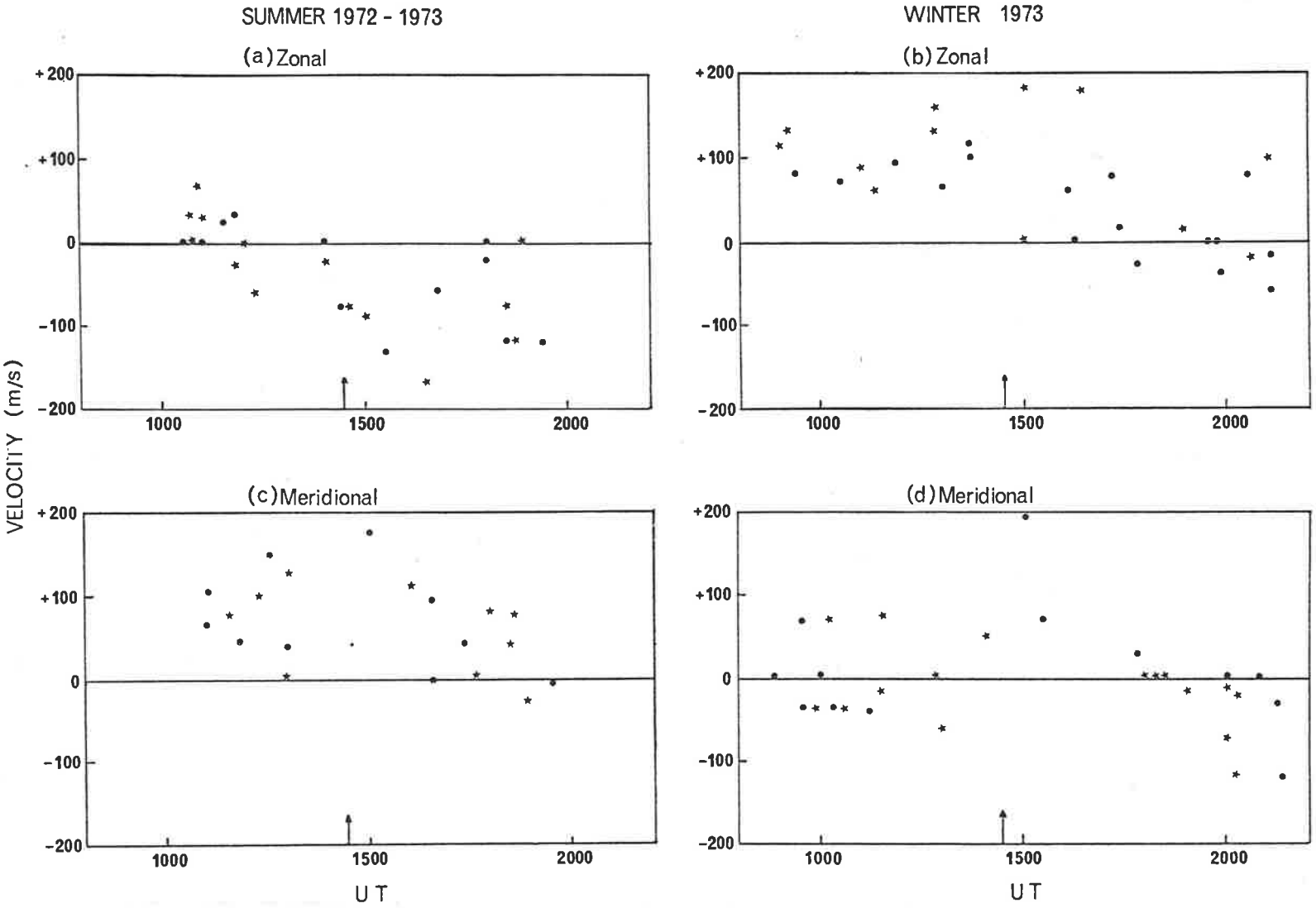

FIG. 46. Diurnal variation of the neutral wind as measured from Mt. Torrens is shown for Summer 1972-1973 and Winter 1973. The winds were measured at a zenith angle of 70°. In the West (*) and in the East (•) for (a) and (b). In the North (*) and in the south (•) for (c) and (d).

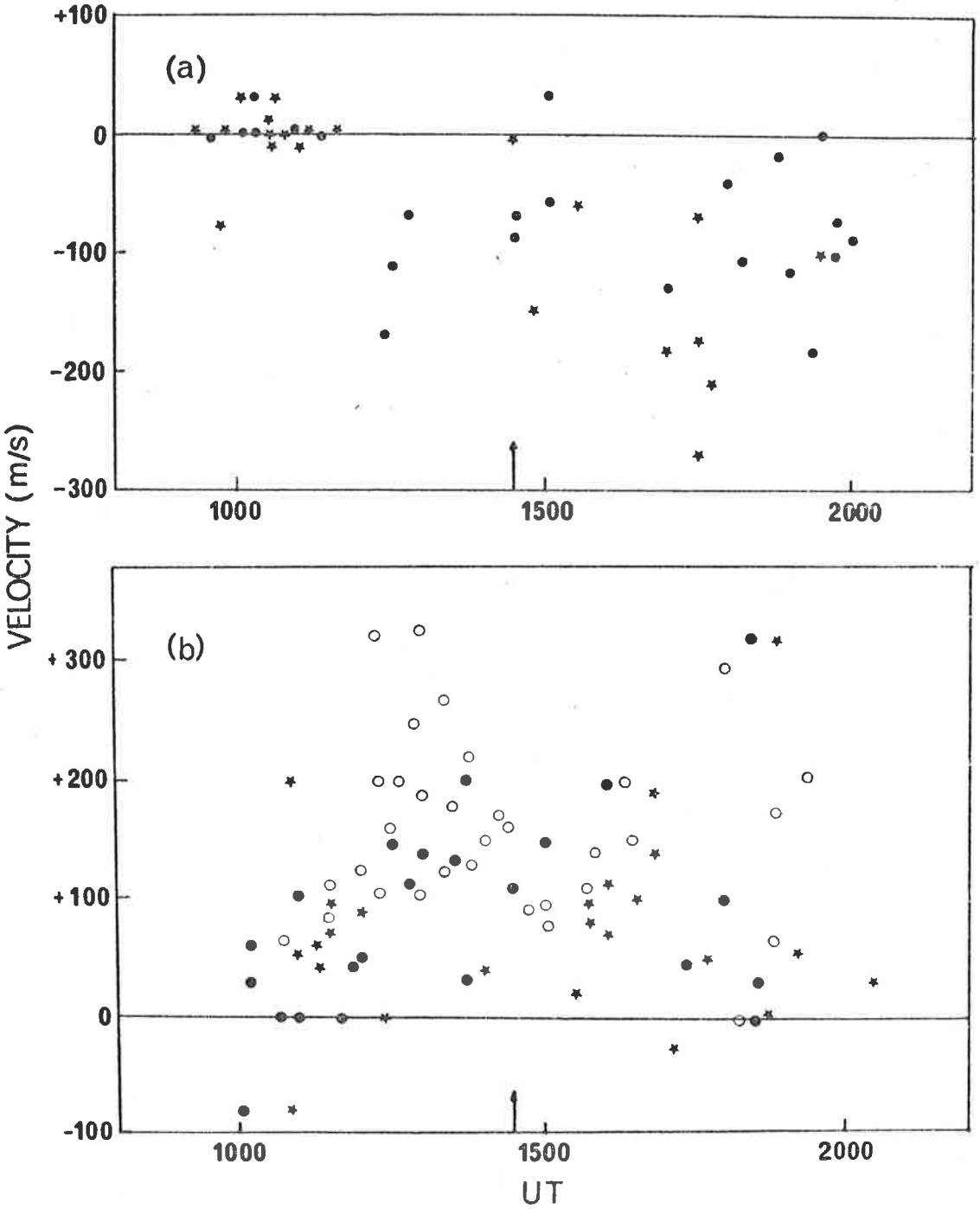

FIG. 47. Neutral winds during periods of magnetic disturbance. (a) Zonal component; positive velocities are eastward. Measurements in the east are denoted (•) and in the west by (*) and all were made at a zenith angle of 70°. (b) Meridional component; positive velocities are northward and measurements in the north were made at a zenith angle of 70° and denoted by (*). Measurements made in the south were at either of two zenith angles, namely 70°, denoted by (•) or 85°, denoted by (0).

evening eastward winds do not seem to occur. This could be explained by a slight intensification of the westward component during these periods. This intensification is certainly apparent during the latter part of the night.

During the periods of magnetic disturbance, the enhancement of the λ630nm emission is greatest to the south of Mount Torrens. For this reason a much larger body of data has been achieved for the meridional component as shown in Figure 47(b). Comparison of these results with those in Figure 46(d), clearly demonstrates the large enhancement of the meridional component of the neutral wind during periods of magnetic disturbance. The meridional component was usually greater than $100ms^{-1}$ equatorward and was occasionally observed to exceed $300ms^{-1}$. These results are in reasonable agreement with those of Hays and Roble (1971) for the aurora of May 14-15, 1969. They did observe a somewhat larger maximum velocity of $450ms^{-1}$ and also attempted one measurement of the zonal component and reported that no wind was observed. Hays and Roble (1971) conclude that their wind measurements are indicative of a bulk mass motion out of the auroral zone. The measurements made by the author support this conclusion and also confirm that the winds extend over a wide range of latitude. This is apparent from the results for December 13, 1972 shown in Figure 48.

The zonal wind component for this night is initially quite small, but soon after sunset a westward component appears and this persists for the rest of the night. The meridional component which is approximately $100ms^{-1}$ equatorward until 1400UT then shows a steady increase to $320ms^{-1}$ in the morning twilight. During this increase both the north and south measurements show equal doppler shifts

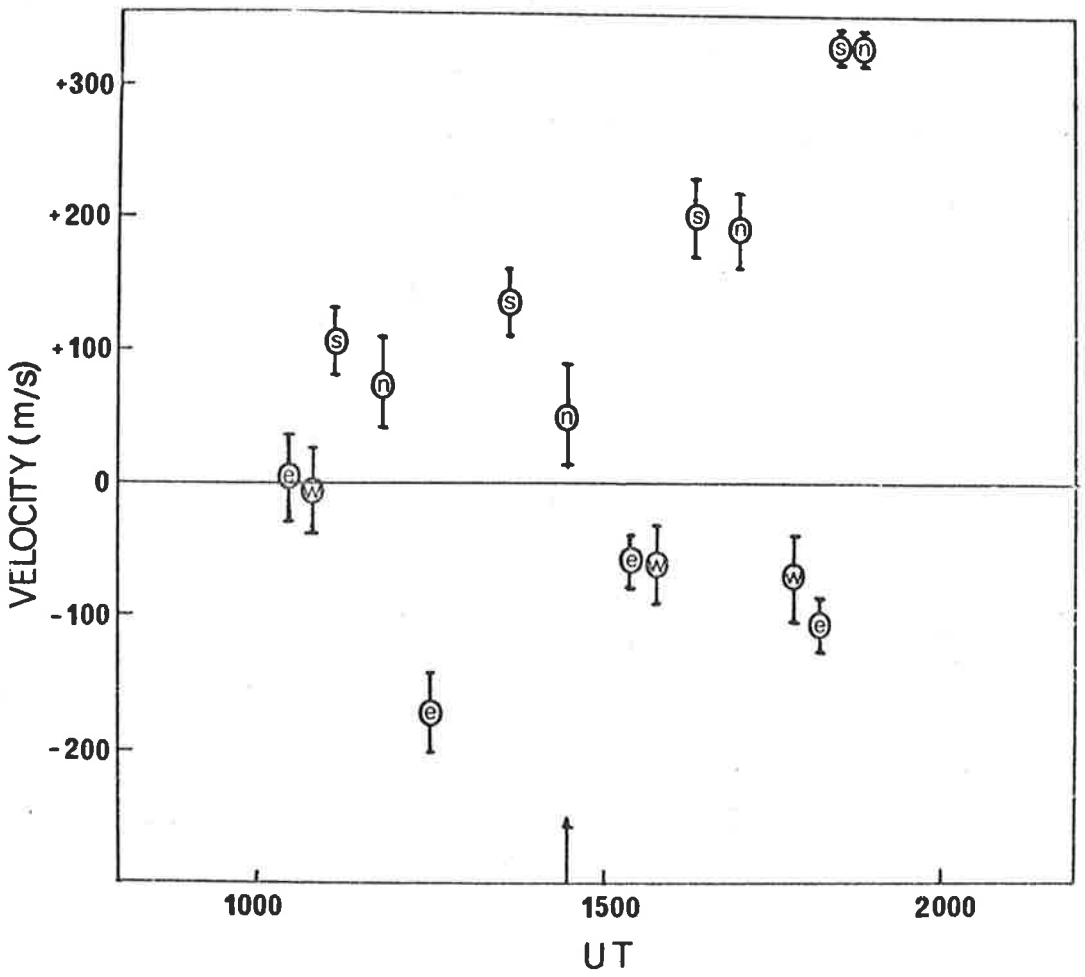

FIG. 48. Neutral winds measured from Mt. Torrens on the 13 Feb 1973. Positive velocities are either northward or eastward. The meridional components are denoted by the letters n or s, referring to measurements made in either the north or south respectively. The zonal components are denoted by the letters e or w, referring to measurements made in either the east or west respectively. All data was obtained at a zenith angle of 70°.

relative to the zenithal λ630nm position. This confirms that the latitude extent of the wind is at least from zenith angle 70°S to 70°N at Mount Torrens.

Some measurements of neutral winds during periods of magnetic disturbance have been made by other methods. De Vries (1972) has reported very high winds of up to 1000ms^{-1} obtained from accelerometer data of the satellite-borne LOGACS experiment. (Low-G Accelerometer Calibration System). Meriwether et al. (1973) have measured winds by tracking chemical releases from rockets. There is agreement, therefore, with the results presented here, that the neutral wind is enhanced in magnitude during magnetic disturbances. The degree of the enhancement observed, however, appears to be rather variable.

7.3.3.3 Comparison with Models

Several models of the neutral wind system in the F region have been published (Challinor, 1969 and 1970, Geisler, 1967 and Kohl and King, 1967). In general these models predict eastward winds in the evening, changing to equatorward about midnight and then westward in the early morning. These predictions are roughly in agreement with the results presented in this chapter. They do not, however, predict the pronounced seasonal variation of the zonal component.

It is clear that the models are unlikely to predict more than the gross features of the neutral wind pattern. It is not the author's intention to attempt to suggest improvements for the models and so further comparison between the results and the theoretical models is not warranted.

7.4 Concluding Remarks

The results presented in this chapter represent a significant addition to the body of thermospheric temperature and neutral wind data that has been obtained, particularly in the case of the wind results.

The diurnal patterns of the temperatures and winds have been shown and these are broadly in agreement with the results of previous workers. The zonal component of the neutral wind exhibits a pronounced seasonal variation which has not been reported previously.

During periods of magnetic disturbance the thermospheric temperatures and the meridional component of the neutral wind are enhanced in magnitude. Once again, these results are shown to be in agreement with the results of others.

CHAPTER 8

CONCLUSION AND SUGGESTIONS FOR FUTURE WORK

The greater part of this thesis has been devoted to the discussion of the development and construction of a very sophisticated optical instrument. It is quite clear however, that more work aimed at improving the FPI would be of value. In particular the étalon plates could be improved and the use of a better photomultiplier, such as an ITT FW130 could also lead to some reduction in the dark current noise.

A more important refinement would be the addition of a low-order FPI in front of the present instrument to allow daytime observations of the λ630nm line. At the time of writing this thesis, work has almost been completed to achieve this refinement, using a 50mm diameter FPI with a finesse of approximately 30. Collection of data over the full 24 hours of the day would be invaluable in assisting comparisons with other observations, in regard to any diurnal variations that may be present. This refinement would also assist in the collection of a large body of data using the FPI.

The measurement of exospheric temperatures and winds over a period of several years from one observatory is yet to be achieved. It is hoped that this will be carried out within the Mawson Institute to study further the trends reported in this thesis and possibly to bring to light other new phenomena.

APPENDIX

ELECTRONIC CIRCUITRY

Parallelism Control

The original electronics used by Ramsay has been described in detail by Kobler (1963) and has been completely redesigned by the author and others, for use in the Mawson Institute FPI. For this reason only the circuitry for which the author was directly responsible will be described in detail.

Three Phase Oscillator

This circuit provides the sine wave drives to the piezoelectric stacks supporting the upper FPI plate and reference waveforms to the phase sensitive detector. They are generated using an astable multivibrator, a digital shift register and a bridged-T filter. This produces a three phase sine wave source which would be capable of small variations in frequency, without the phase relationships between the outputs varying. The drive to the stacks is a 10 volt peak-to-peak sine wave, biased 10 volts positive so that the voltage applied to the stacks is always the same sign as the polarization of the piezoelectric discs.

PIN Diode Preamplifier

The PIN diode preamplifier is a modified version of the photomultiplier low current amplifier described in Chapter 5. The diode, cable and circuit capacitance cause the preamplifier response to roll off at 8 kHz and this limits high frequency noise. The preamplifiers are mounted in grounded metal containers to prevent unwanted stray signal pickup. These containers are mounted as close

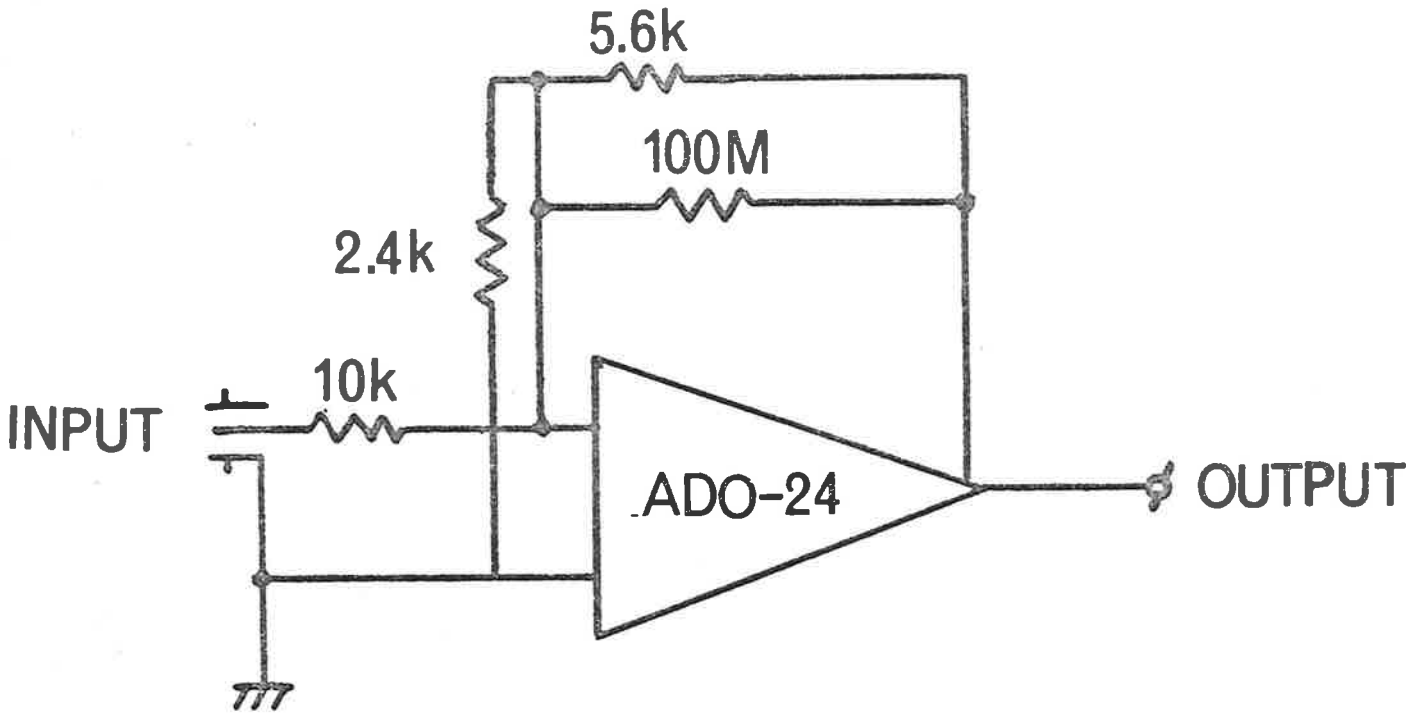

FIG. 49. PIN diode preamplifier circuit diagram.

as practicable to the diodes themselves in order to keep the input capacitance to a minimum. The circuit diagram of the preamplifier is shown in Figure 49.

The DC outputs from the two preamplifiers are indicated by two front panel meters to permit the servo loop to be locked onto the correct peak and not one of the subsidiaries.

Bandpass Filter and Phase Sensitive Detector

An active filter using an integrated circuit (709) is used as a bandpass filter tuned to 4 kHz with Q value of 20 and a gain of 40. The Q value of the tuned filter can be altered by changing resistors R and KR in Figure 50, according to the relation

$$Q = 1/(1-K) \quad \text{and}$$

$$KR + R = 25\ k\Omega\ .$$

A two transistor circuit follows to provide the two phase drive to a constant amplitude phase shift circuit (50 kΩ potentiometer and 4.7 nF capacitor). This allows phase adjustment of the input to the phase sensitive detector (PSD). A second transistor pair is used to present a high impedance (using the bootstrap technique) to the phase shift network. Any DC level at the output of the buffer stage can be minimized by changing the resistor R_1.

The PSD is an amplifier with a gain of 10, which is switched from an inverting to non-inverting configuration, according to the states of the input switching transistors. These transistors are driven by a square wave signal (V_D) and its complement ($\overline{V}_D$) provided by the 3 phase oscillator. The output of the PSD is either positive or negative, according to whether V_D and the error signal are 180° out

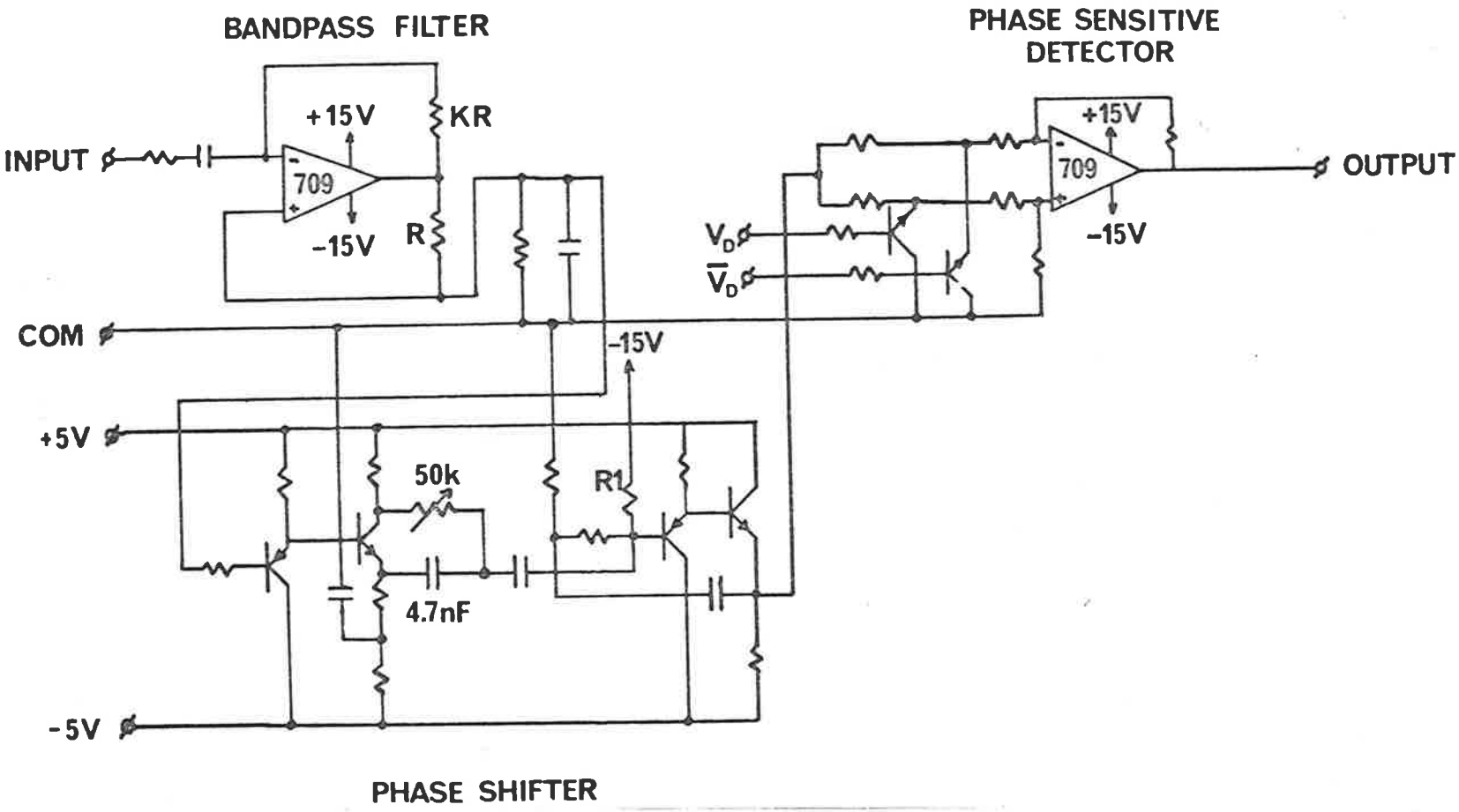

FIG. 50. Bandpass filter and phase sensitive detector circuit diagrams.

of phase or exactly in phase, respectively.

The Equalizer

The equalizer is designed to shape the response of the overall system according to a number of criteria. The loop gain should fall to unity at as high a frequency as can be obtained to achieve maximum benefit of the servo system. Below this frequency the loop gain should rise rapidly to its DC value. At any frequency the slope must not exceed 40 dB per decade or instability will occur.

The equalizer circuit illustrated in Figure 51 is based on a 709 integrated amplifier, which has sufficient gain to compensate for the insertion loss of the filter at the input. This ensures that the equalizer is nominally of unity gain. The equalized response of the servo loop rolls off at approximately 37 dB per decade from a frequency of 2 Hz (Bode stability criterion).

600V Supply

The supply is effectively an operational amplifier which provides an output voltage equal to the input current by 10^6. Resistors connected to the amplifier input allow input voltages to be summed. The supply is capable of delivering up to 600 volts at 3 mA.

Stabilized Power Supplies

A number of stabilised power supplies were constructed to provide power for the parallelism control electronics.

Dual 15 volt supplies capable of delivering 800 mA were required to power the integrated circuits in the various units described. Dual 5 volt supplies capable to delivering 500 mA were used to supply

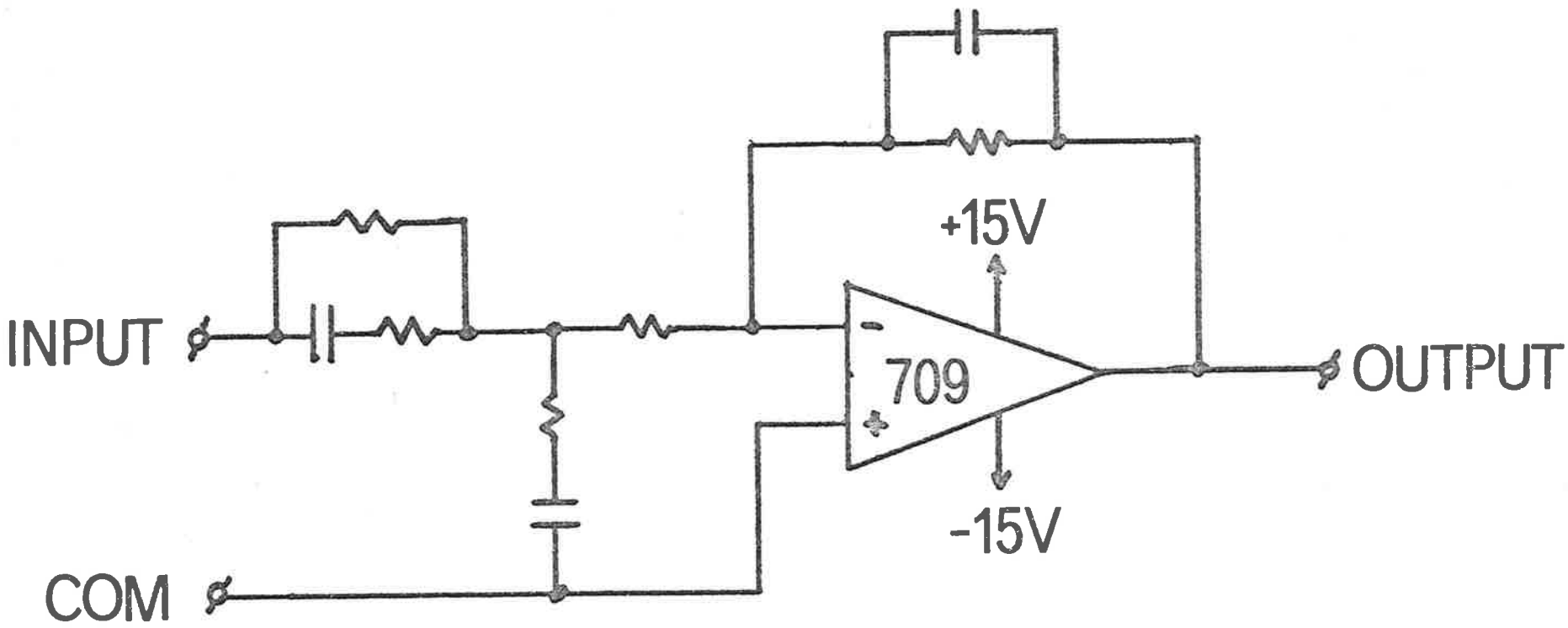

FIG. 51. Parallelism control servo-loop equalizer.

power to the logic circuitry in the three phase oscillator and the -5 volt supply is used to power the parallelism lamps and provide the reference for the manual set potentiometers.

Dual 20 volt supplies capable of delivering 500 mA provide the power for the PIN diode preamplifiers. They are also used for the photomultiplier low current amplifier or the pulse amplifier and discriminator, depending on which is in use. This power supply shares one of its mains transformers with the photomultiplier shutter control.

Adjustments

The FPI plates can be set parallel by mechanical adjustment to better than 0.1 μm so that only small corrections need to be made with the piezoelectric stacks. These provide up to 3 μm movement.

The frequency of the three phase oscillator should next be adjusted to match the bandpass filter, by varying the +5 volt supply rail. The PSD output for the X and Y servos should now be displayed on a two-beam oscilloscope and the phase shift adjusted so that the error signal input to the PSD is in phase or 180° out of phase with the reference drive (V_D) to the PSD. These last two adjustments need to be carried out periodically and are routinely checked about once a month.

The gain of the servo loop is now adjusted by varying the voltages applied to the lamps in the collimated light sources.

Separation Control

10 kHz Oscillator

The design chosen places quite stringent requirements upon the AC drive applied to the transducer. The servo loop includes a band-pass filter, which implies that the frequency of the oscillator must be kept stable. A 10 Hz change in frequency will introduce an error equivalent to a spacing change of 1 nm. This is not particularly difficult to achieve and is met by many commercial oscillators in the medium price bracket. The amplitude stability of the oscillator needs to be about one part in 10^3 which is much more difficult to achieve. The oscillator used was a Hewlett Packard Model 3300 function generator which was found to have the necessary frequency stability, but was somewhat marginal in regard to amplitude stability. Attempts were made to measure the oscillator amplitude stability using a Hewlett Packard Model 400E AC voltmeter, and digital voltmeter, but the resolution of this instrument was not quite sufficient to enable a completely definitive decision to be made as to the amplitude stability. Consideration was given to a number of designs to use in constructing an oscillator to replace the model 3300, but no straightforward solution to the amplitude stability problem was apparent and so it was decided to persevere with the 3300.

Differential Amplifier

The circuit diagram of the differential amplifier is shown in the servo loop schematic, given in Figure 21. It is based on the integrated circuit type LM308 which was chosen because it has high input impedance (40 MΩ) and high common mode rejection ratio. The amplifier is connected in differential mode with unity gain so that

the output is equal to the difference between the signals applied to the two inputs. The resistors used in the prototype circuit were of the carbon composition type and it was found that the noise inherent in this type of resistor impaired the performance of the separation control. Consequently they were replaced with metal film resistors which have low noise characteristics.

The circuit is assembled on a small printed circuit board, which is mounted on the transducer holder. This ensures that the connections between the capacitance transducer and the circuit board are kept short. A variable capacitor is provided on the board which can be adjusted from outside the étalon chamber. This is operated by passing a non-conducting screw-driver through a hole in the top brass plate of the chamber and the capacitor is adjusted by screwing a small brass bolt which is electrically grounded, closer to or further from one of the amplifier inputs. This adjustment is used to minimise the output from the amplifier when the capacitor is in its balance position. This operation has been denoted "nulling" the capacitance transducer and usually requires some fine adjustment after the étalon chamber has been closed and hence the need for the access from outside the chamber.

10 kHz Rectifier

The output from the differential amplifier goes to the input of the bandpass filter (see Figure 52). The input buffer to the filter is based on a 709 integrated circuit which is connected in the inverting configuration. This stage has a gain of 10 and with the associated resistor provides the correct source impedance for the filter. A T-section constant K bandpass filter centred on 10 kHz is used with a passband of about 900 Hz. The capacitors and inductors

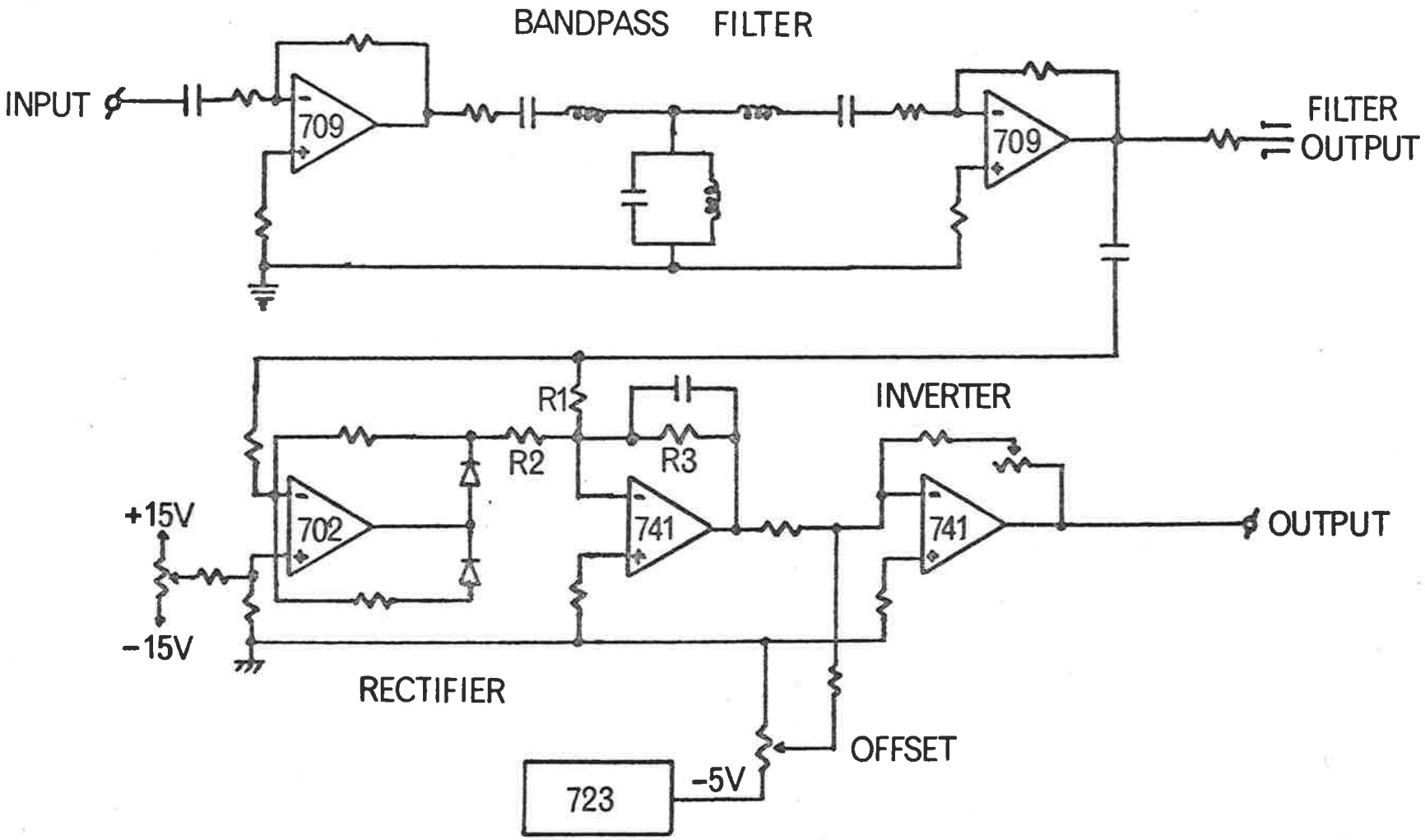

FIG. 52. 10 KHz rectifier circuit diagram.

used are selected to within 1%. The filter is followed by an output buffer, which provides the correct terminating impedance.

The signal is AC coupled to the input of the high speed rectifier which uses one 702 and one 741 integrated circuit amplifier. The design is based upon a circuit given in the Fairchild Handbook (1967). The first amplifier acts as a unity-gain, half-wave rectifier, giving negative output for positive input signals. The output, along with the original signal, is fed into the second amplifier, which sums them together. Because of the ratios R_3/R_1 and R_3/R_2, the second amplifier operates with unity gain to the original signal, and two times gain for the negative half wave output. The result is that the output is always positive-going and equal to the absolute value of the input. The second amplifier also acts as a low-pass filter with the 3 dB-point at 1.4 kHz.

The output from the rectifier and an offset voltage are summed at the input of the inverter stage which utilises a 741 integrated circuit. The offset voltage is obtained from a front-panel mounted, ten-turn potentiometer. The stable voltage applied across the potentiometer is generated using a 723 integrated circuit precision voltage regulator. The gain of the inverter is adjustable in order to set the overall gain of the transducer and electronics such that the voltage-displacement coefficient is 2 mV/nm referred to the output of the inverter. If this output were applied to the scan input of the piezoelectric stack supply system, then the resulting servo loop would have approximately unity-gain.

Particular care was taken to separate power and signal common lines in this circuitry except for one connection. This is an important precaution to be taken in the design of low level circuits

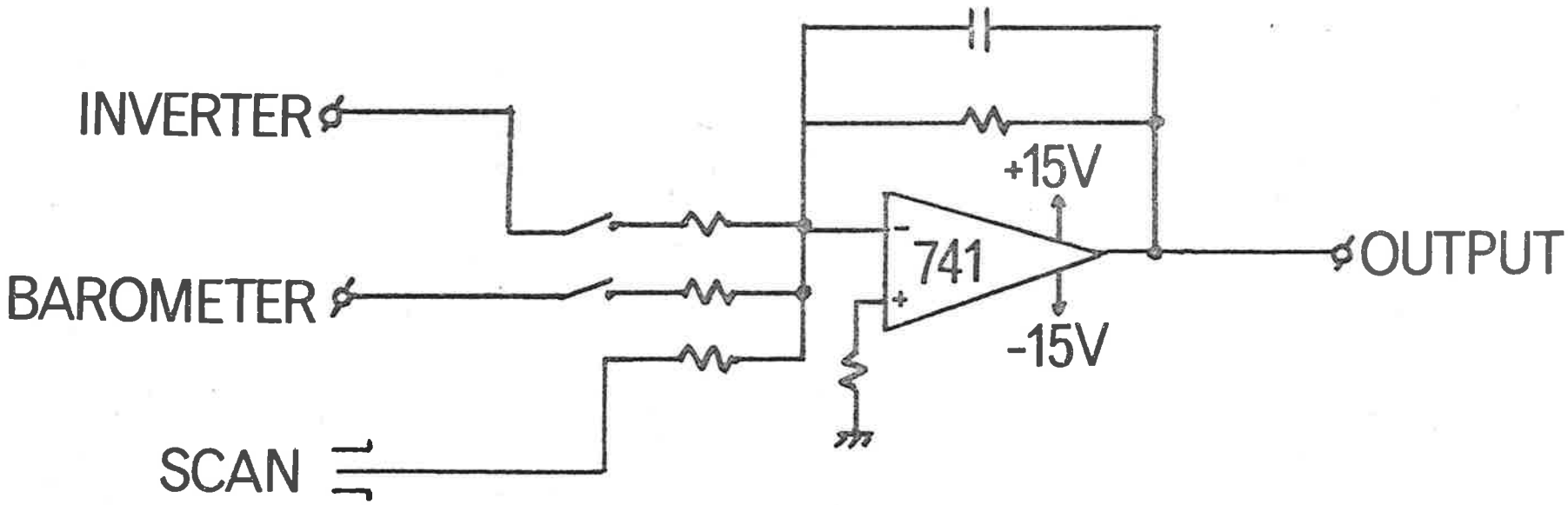

FIG. 53. Equalizer circuit for separation control servo loop.

such as the one described above.

Equalizer

The criteria for equalization of a servo loop were given earlier, as applied to the parallelism control and are equally applicable in the separation servo loop. It was decided, for the sake of simplicity to not attempt maximum bandwidth equalization where a 37 dB per decade roll-off is used. Instead a single pole R-C network, as shown in Figure 53, was used. This provides a 20 dB per decade roll-off from a frequency of 2 Hz.

The equalizer also acts as a summing amplifier for the inverter output signal, the barometer signal and the external scanning signal.

Scan Input Attenuator

When the signal averager scans over 512 channels the channel address analogue output swings from zero to four volts. This variation applied to the input of the equalizer would change the plate spacing by approximately four orders at λ630nm. To enable different ranges of plate spacing to correspond with the scan range of the averager, a variable attenuator was necessary between the averager output and the equalizer input (see Figure 54).

The input stage of the attenuator is a unity gain differential amplifier, which incorporates a low-pass filter, with 3 dB point at 100 Hz. This filtering is necessary to damp the rapid change in the channel address signal when the averager goes from channel 512 to channel one, at the end of a scan. The output of this stage is applied to a voltage divider and the input to the voltage follower

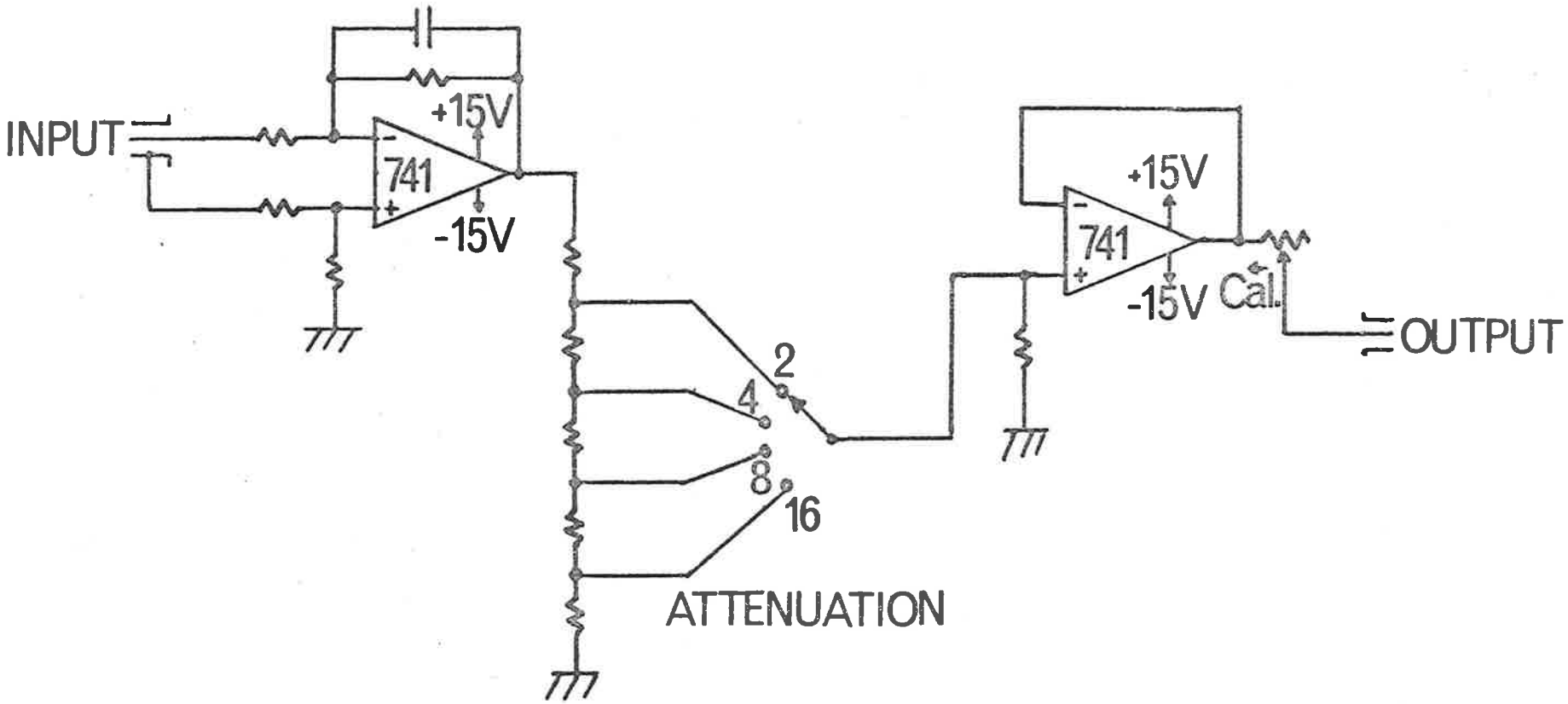

FIG. 54. Circuit diagram of the scan input attenuator.

stage is switched between four positions on this divider, thus providing 2, 4, 8, or 16 times attenuation. The 10kΩ potentiometer on the output of the voltage follower allows a continuous adjustment of the attenuation by up to two times.

Temperature Control

The temperature controller electronics provides facilities for one monitor thermistor, four temperature controllers and a panel meter for monitoring error signals in each of the five cases. The unit is self-contained and includes stabilised power supplies for the control and monitoring electronics.

Error Amplifier and Triac Trigger

The temperature sensing circuitry shown in Figure 55, uses a modified bridge technique. Instead of using a differential amplifier to measure the output of a wheatstone bridge, a unity gain amplifier is used to supply two arms of the bridge with $\pm$ V, such that the error amplifier sums currents into a ground point. The basic bridge supply is provided by a 723 regulator whose output is inverted by a unity gain 709 stage to provide -V. The two arms of the bridge consist of a thermistor and linearising resistor (2.7 kΩ) in one arm and a reference resistor, which is made equal to the resistance of the thermistor at the desired operating temperature and the same linearising resistor, in the second arm.

The output of the error amplifier (709) is then fed to a triac driver integrated circuit (742), which provides trigger pulses to the triac at zero crossing time of the mains supply. In the case of the air heater another amplifier (LM308) was used to add lead compensation (or rate feedback) to improve the control system.

The zero-crossing type of control was required to minimise the radio-frequency noise produced because of the sensitivity of the other low-level circuitry to such noise.

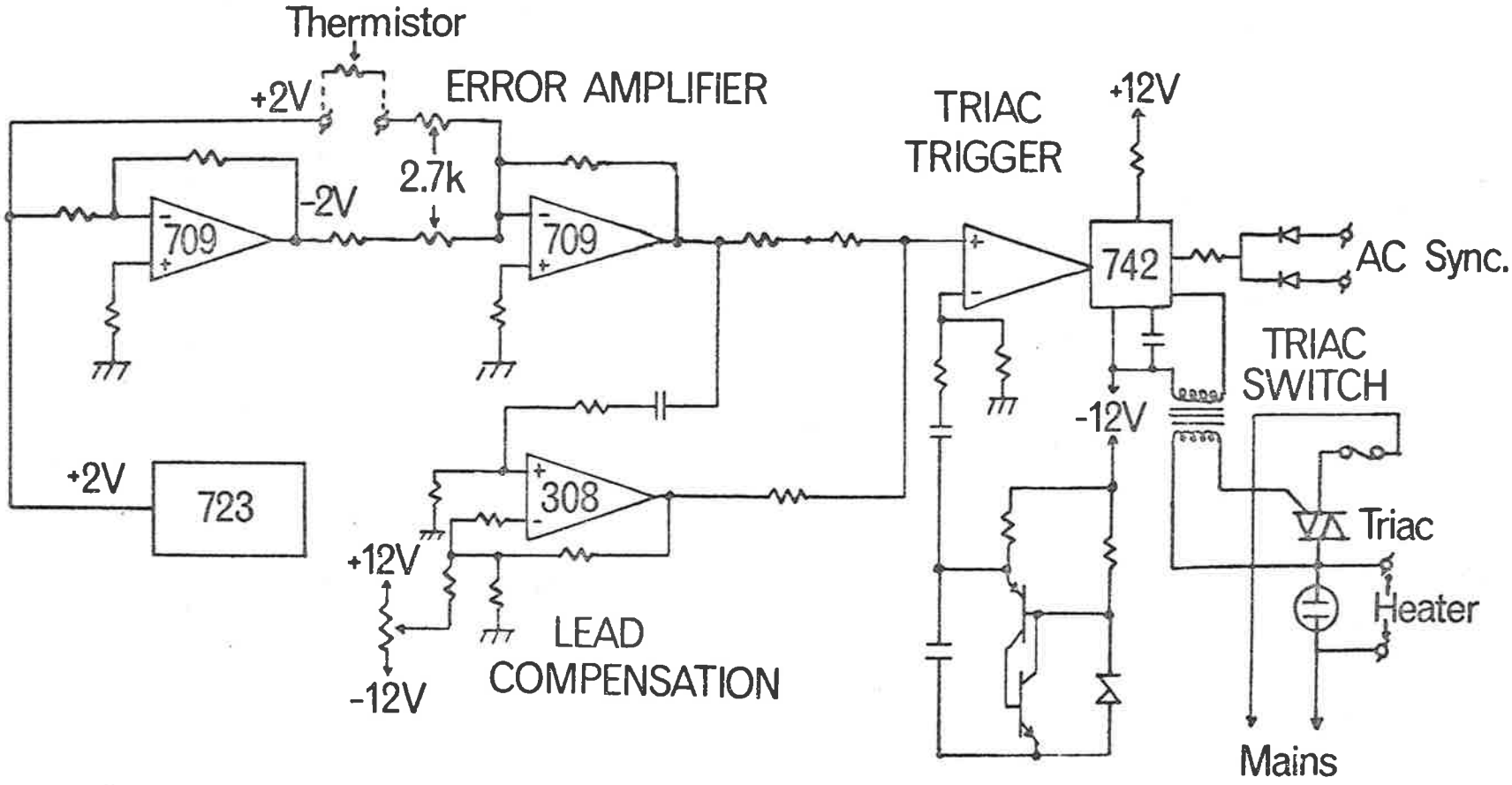

FIG. 55. Temperature control electronic circuitry.

Triac Switch

The trigger pulses from the 742 are passed to the triac AC06DT via a trigger transformer, in order to ensure isolation between the low level input circuitry and the AC mains. For the same reason and also in the interests of safety, the triac is mounted on a separate circuit card from the input electronics. A front panel neon indicator lamp gives a visual display of when the heater is on and is a useful guide to any malfunctioning in the temperature control servo loop.

Pulse Counting Electronics

Preamplifier and Discriminator

The pulse amplifier and discriminator circuit is shown in Figure 56. The preamplifier is based on a design by Eather and Reasoner (1969) and consists of three stages which provide an overall gain of about 50 dB, and a bandwidth of 15 MHz. Upper and lower discrimination are provided by two high speed differential comparators (Fairchild integrated circuit μA 710C), which compare the pulse amplitude with pre-set voltages determined by the settings of the two 1 kΩ helipots. If the pulse height is larger than the lower level setting then the monostable (74121) is triggered, unless the pulse height exceeds the upper setting in which case the monostable will be inhibited. The response time of the comparators is quoted as being 40ns for a 100 mV input step. The dynamic range of the circuit was measured as 67 dB, with the lower level threshold set just high enough to prevent noise triggering the monostable and with the upper level threshold set at 4.5 volts. The output pulses from the monostable are TTL compatible, being approximately 1.2 μs long and +5 volts in amplitude, and are fed directly to the input of the signal averager. The overall response of the circuitry was therefore limited by the monostable and was approximately 1 MHz. A wider frequency response was not provided because of the limited response of the signal averager and also because of the very low count rates normally encountered.

Ratemeter

The circuit diagram of the ratemeter is shown in Figure 57. The input pulses are fed via an emitter follower to an XR 320 package wired in a monostable configuration. The output pulses from the

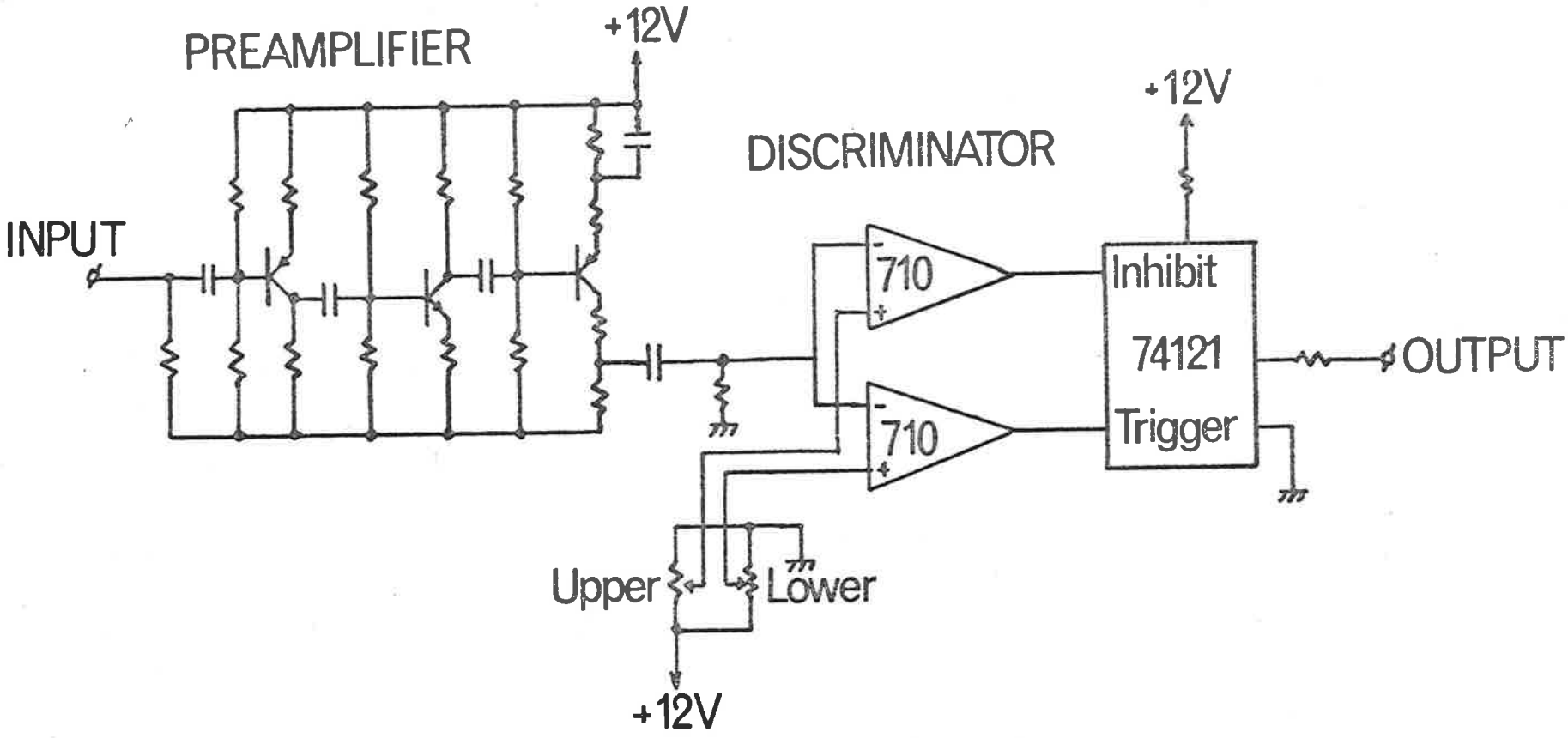

FIG. 56. Pulse amplifier and discriminator circuit diagram.

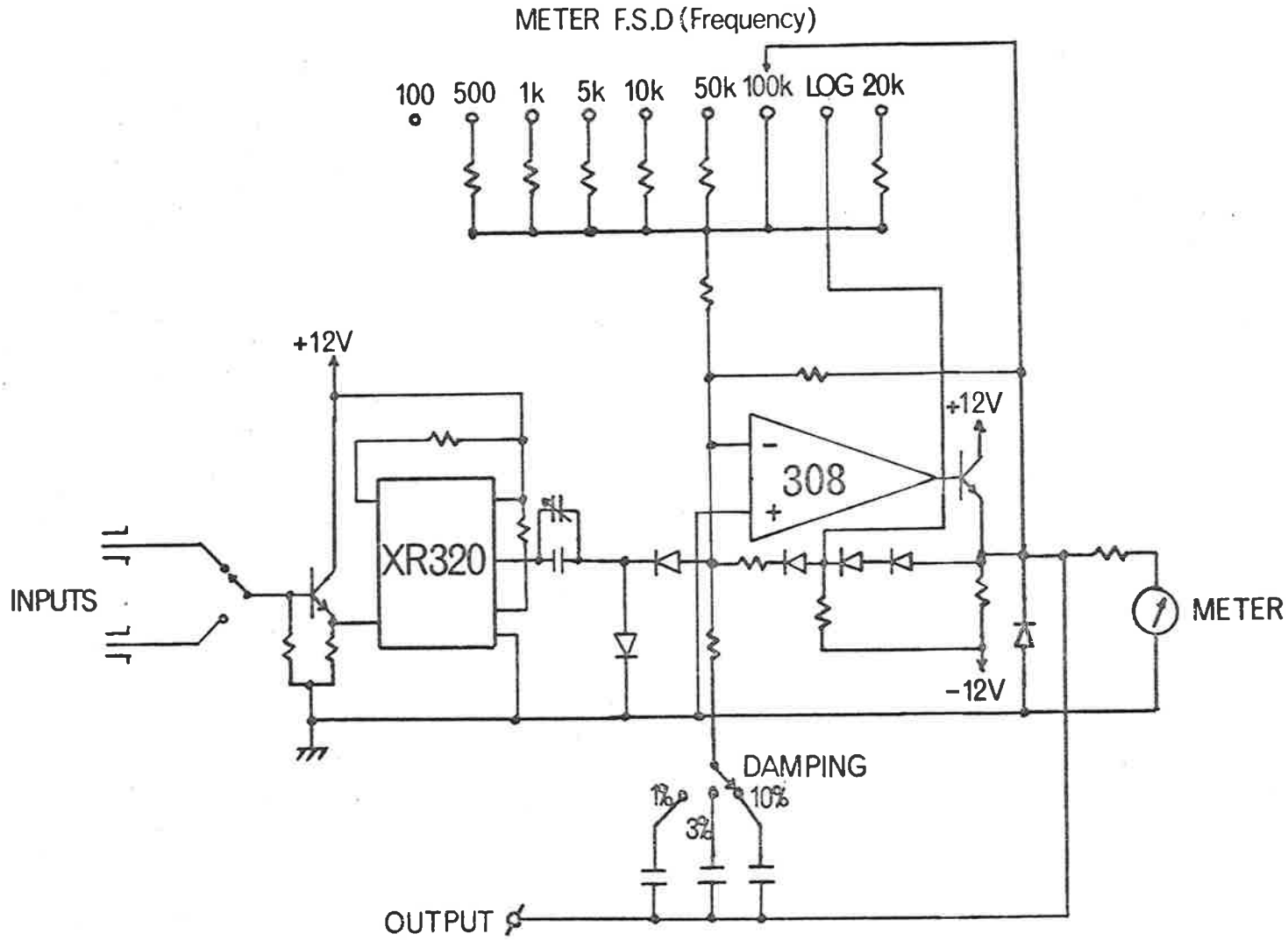

FIG. 57. Ratemeter circuit diagram.

monostable are approximately 2 μs long and +12 volts in amplitude. The output drives a diode pump circuit. A variable capacitor is provided to allow the unit to be calibrated. The feedback resistor across the amplifier (LM308) is varied to change the gain of the system and the frequency response is determined by one of three possible capacitors in parallel with this resistor.

The logarithmic response is achieved by replacing the feedback resistor with a diode, which provides a rough approximation to a logarithmic response with a sensitivity of 0.1 of full-scale-deflection per decade. If the maximum count rate of the rate-meter (300 kHz) is exceeded then the output drops back to zero volts.

Photomultiplier Shutter Control Electronics

The shutter is of the latching type, the state of which is changed by the activating solenoid (see Figure 58). This is achieved by discharging a capacitor through the activating solenoid. The secondary winding of the mains transformer provides 39 volts AC which is rectified and charges the storage capacitor to approximately 30 volts. To activate the shutter the push button is pressed and the capacitor discharges through the solenoid. A micro-switch mounted on the shutter senses whether it is open or closed and the appropriate panel lamp glows.

Power failure protection is provided by inclusion of the relay designated A. The coil of the relay is energised directly from the transformer centre-tap and so in the event of a power failure the contact A1 closes. If the shutter is open then a circuit is made via the microswitch such that the capacitor will discharge through

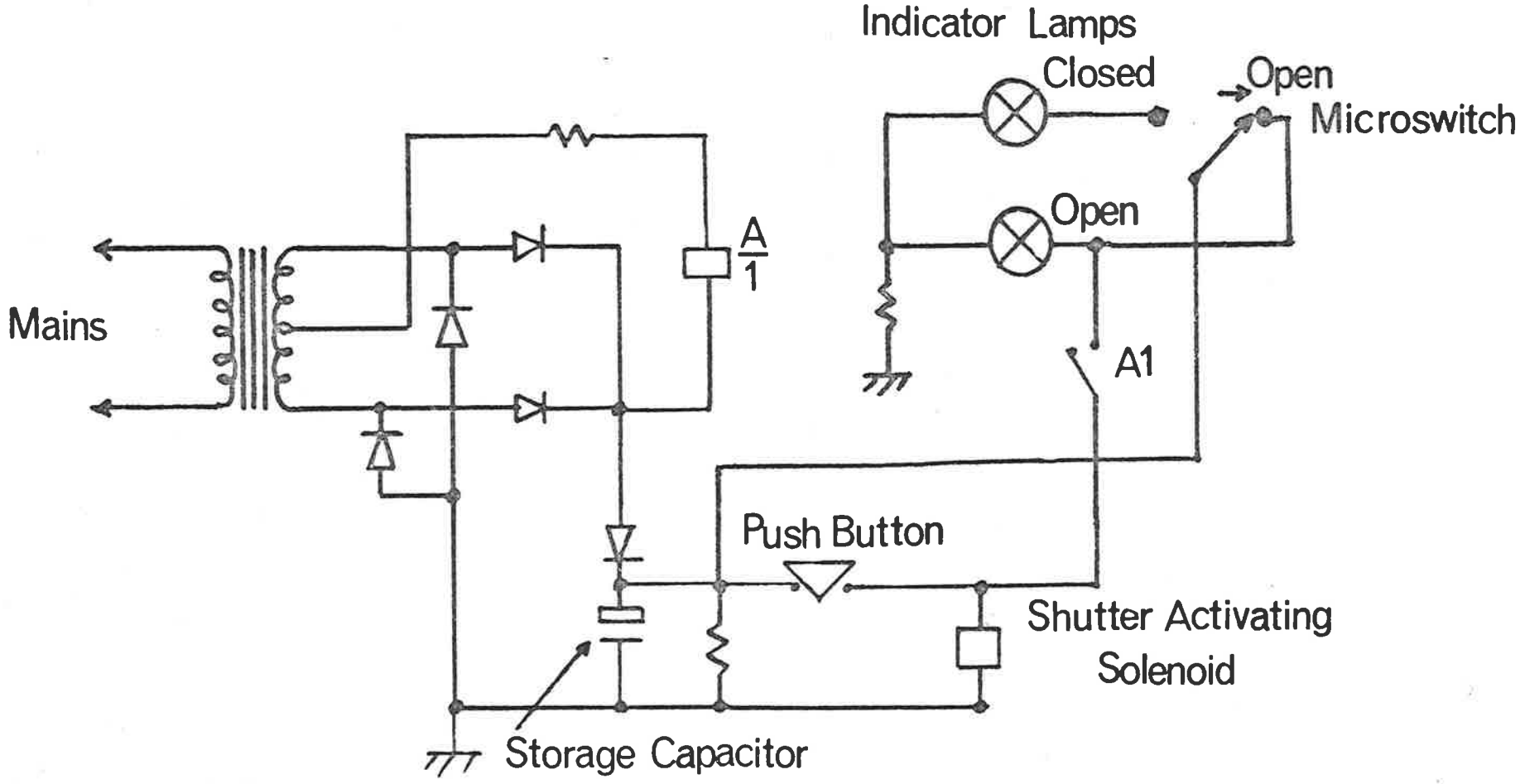

FIG. 58. Photomultiplier shutter control electronics. Relay A: A/1 is the solenoid for the power failure protection relay. Contact A1 is normally open.

the solenoid, protecting the photomultiplier tube from possible high light levels.

BIBLIOGRAPHY

Armstrong, E.B. (1955). The Observation of line widths in the airglow and aurora with a photo-electric Fabry-Perot Interferometer. The Airglow and the Aurora. (Ed. Armstrong, E.B. and Dalgarno, A.)

Amstrong, E.B. (1959). The temperature in the atmospheric region emitting the nightglow OI5577 line and in regions above faint auroral arcs. J. Atmos. Terr. Phys. 13, 205.

Armstrong, E.B. (1969). Doppler shifts in the wavelength of the OI λ6300 line in the night airglow. Planet. Space Sci. 17, 957.

Armstrong, E.B. and Bell, J.A. (1970). Variations in the width of the nightglow OI λ6300 line during the magnetic storm of October 30-November 2, 1968. Planet. Space Sci. 18, 784.

Babcock, H.D., (1923). Study of the green auroral line by the interference method. Astrophys. J. 57, 209.

Bedinger, J.F. (1970). Measurements of winds above 200 kilometers. J. Geophys. Res. 75, 683.

Bens, A.R., Cogger, L.L., and Shepherd, G.G. (1965). Upper Atmospheric temperatures from Doppler line widths-III Observations of the OI dayglow emission at 6300Å. Planet. Space Sci. 13, 551

Bevington, P.R. (1969). Data reduction and error analysis for the physical sciences. McGraw-Hill Book Company, New York.

Biondi, M.A. and Feibelman, W.A. (1968). Twilight and nightglow spectral line shapes of oxygen λ6300 and λ5577 radiation. Planet. Space Sci. 16, 431.

Blamont, J.E. and Lory, M.L. (1964). Sudden heating of the ionosphere in the auroral zone. Nature 201, 593.

Blamont, J.E. and Luton, J.M. (1972). Geomagnetic effect on the neutral temperature of the F region during the magnetic storm of September 1969. J. Geophys. Res. 77, 3534.

Born, M. and Wolf, E. (1965). Principles of Optics, Third Edition, Pergamon Press, New York.

Brault, J.W. and White, O.R. (1971). The analysis and restoration of astronomical data via the Fast Fourier Transform. Astron. & Astrophys. 13, 169.

Broadfoot, A.L. and Kendall, K.R. (1968). The airglow spectrum, 3100-10000Å. J. Geophys. Res. 73, 426.

Bruce, C.F. and Hill, R.M. (1961). Wavelengths of Krypton 86, Mercury 198, and Cadmium 114. Aust. J. Phys. 14, 64.

Buisson, H. and Fabry, Ch. (1912). Width of spectrum lines. J. Phys. 11, 442.

Cabannes, J. and Dufay, J. (1955). Etude interferentielle des raies rouges du ciel nocturne. The Airglow and the Aurorae. (Ed. Armstrong, E.B. and Dalgarno, A.)

Carlson, H.C. and Sayers, J. (1970). Discrepancy in electron temperatures deduced from Langmuir probes and from incoherent scatter radars. J. Geophys. Res. 75, 4883.

Chabbal, R. (1953). Recherche des meilleures conditions d' utilisation d'un spectrometre photoelectrique Fabry-Perot. J. Rech. Centre Nat. Rech. Sci. Lab., 24, 138.

Chabbal, R. (1958). Finesse limite d'un Fabry-Perot formé de lames imperfaites. J. Phys. et le Rad. 19, 295.

Challinor, R.A. (1969). Neutral-air winds in the ionospheric F-region for an asymmetric global pressure system. Planet. Space Sci. 17, 1097.

Challinor, R.A. (1970). Neutral-air winds in the ionospheric F-region for an asymmetric global pressure system. Planet. Space Sci. 18, 1485.

Chamberlain, J.W. and Smith, C.A. (1959). On the excitation rates and intensities of OH in the airglow. J. Geophys. Res. 64, 611.

Chamberlain, J.W. (1961). Physics of the aurora and airglow. Academic Press, New York.

Coates, P.B. (1973). Photomultiplier collection efficiencies and nonpoissonian pulse height distributions. J. Phys. D: Appl. Phys. 6, 153.

Cogger, L.L., Nelson, G.J., Biondi, M.A., Hake, R.D. and Sipler, D.P. (1970). Coincident F-Region temperature determinations from incoherent backscatter and doppler broadening of [OI] 6300Å. J. Geophys. Res. 75, 4887.

Connes, P. (1956). Increase of the product of luminosity x resolution with interferometers by employing path differences independent of the incidence. Rev. Opt. 35, 37.

Davies, W.E.R. (1972). Reduction of Dark Current in photomultiplier tubes. Rev. Sci. Instrum. 43, 556.

De Vries, L.L. (1972). Structure and motion of the thermosphere shown by density data from the Low-G Accelerometer Calibration System (LOGACS), Space Res. 12, 867.

Dickinson, R.E., Lagos, C.P. and Newell, R.E. (1968). Dynamics of the neutral gas in the thermosphere for small Rossby number motions. J. Geophys. Res. 73, 4299.

Eather, R.H. and Reasoner, D.L. (1969). Spectrophotometry of faint light sources with a tilting-filter photometer. Appl. Optics, 8, 227.

Evans, J.V. (1969). Theory and practice of ionosphere study by Thomson scatter radar. Proc. I.E.E.E., 57, 496.

Evans, J.V. (1972). Ionospheric movements measured by incoherent scatter: A review. J. Atmos. Terr. Phys. 34, 175.

Farkas, G.Y. and Varga, P. (1964). Reduction of dark current in transparent cathode photomultipliers for use in optical measurements. J. Sci. Instr. 41, 704.

Feibelman, W.A., Hake, R.D., Sipler, D.P., and Biondi, M.A. (1972). Twilight and night-time ionospheric temperatures from oxygen λ6300 and λ5577 spectral-line profiles. J. Geophys. Res. 77, 1869.

Foord, R., Jones, R., Oliver, C.J. and Pike, E.R. (1969). The use of photomultiplier tubes for photon counting. Appl. Optics 8, 1975.

Frommhold, L. and Feibelman, W.A. (1967). The reduction of noise and dark current in photomultiplier tubes by magnetic defocusing. J. Sci. Instrum. 44, 182.

Gadsden, M. (1965). Some statistical properties of pulses from Photomultipliers. Appl. Optics 4, 1446.

Geisler, J.E. (1967). A numerical study of the wind system in the middle thermosphere. J. Atmos. Terr. Phys. 29, 1469.

Giles, J.N. (1967) ed. Fairchild semiconductor linear integrated circuits application handbook. p.150.

Gunter, W.D., Erickson, E.F. and Grant, G.R. (1965). Enhancement of photomultiplier sensitivity by total internal reflection. Applied Optics 4, 542.

Gunter, W.D., Grant, G.R. and Shaw, S.A. (1970). Optical devices to increase photocathode quantum efficiency. Appl. Optics 9, 251.

Hays, P.B., Nagy, A.F. and Roble, R.G. (1969). Interferometric measurements of the 6300Å doppler temperature during a magnetic storm. J. Geophys. Res. 74, 4162.

Hays, P.B., Nagy, A.F., McWatters, K.D. and Evans, J.V. (1970). Comparison of radar and optical temperature measurements in the F-region. J. Geophys. Res. 75, 4881.

Hays, P.B. and Roble, R.G. (1971). A technique for recovering Fabry-Perot Interferometer fringes of very low intensity. Appl. Optics 10, 193.

Hays, P.B. and Roble, R.G. (1971) Direct observations of thermospheric winds during geomagnetic storms. J. Geophys. Res. 76, 5316.

Hernandez, G. (1966). Analytical description of a Fabry-Perot spectrometer. Appl. Opt. 5, 1745.

Hernandez, G. (1970). Analytical description of a Fabry-Perot photoelectric spectrometer. 2: Numerical results. Appl. Optics 9, 1591.

Hernandez, G. (1972). Spectroscopic studies of the arc of March 8-9, 1970. Planet. Space Sci. 20, 1309.

Hernandez, G. (1974). Contamination of the OI ($^3P_2$-$^1D_2$) emission line by the (9-3) band of OH $\chi^2\Pi$ in high resolution measurements on the night sky. Preprint.

Hilliard, R.L. and Shepherd, G.G. (1966a). Wide-angle Michelson interferometer for measuring Doppler line widths. J. Opt. Soc. Amer. 56, 362.

Hilliard, R.L. and Shepherd, G.G. (1966b). Upper Atmospheric Temperatures from doppler line widths - IV: A detailed study using the OI 5577Å auroral and nightglow emission, Planet. Space Sci. 14, 383.

Hirschfeld, T. (1968). Improvements in photomultipliers with total internal reflection sensitivity enhancement. Appl. Optics 7, 443.

Hunten, D.M., Rundle, H.N., Shepherd, G.G., Vallance-Jones, A. (1967), Optical upper atmospheric investigations at the University of Saskatchewan. Appl. Opt. 6, 1609.

Jacchia, L.G. (1965). Static diffusion models of the upper atmosphere with empirical temperature profiles. Smithson. Contrib. Astrophys. 8, 215.

Jacchia, L.G. (1970). New static models of the thermosphere and exosphere with empirical temperature profiles. Smithson. Astrophys. Obs. Spec. Rep. 313.

Jacquinot, P., and Dufour, Ch. (1948). Optical conditions in the use of photo-electric cells in spectrographs and interferometers. J. Res. Centr. Nat. Res. Sci. 6, 91.

Jacquinot, P. (1954). The luminosity of spectrometers with prisms, gratings or Fabry-Perot étalons. J. Opt. Soc. Amer. 44, 761.

Jacquinot, P. (1960). New developments in interference spectroscopy. Rept. Progr. Phys. 23, 267.

Jarrett, A.H. and Hoey, M.J. (1963). Ground level photographic observation of day airglow at 6300Å. Planet Space Sci. 11, 1251.

Jarrett, A.H., Hoey, M.J. and Paffrath, L. (1964). Observations of the 6300Å emission of the nightglow with a pressure scanning Fabry-Perot interferometer. Planet. Space Sci. 12, 591.

Jennings, R.J., Gunter, W.D. and Grant, G.R. (1970). Quantum efficiencies greater than 50% from commercially available photomultipliers. J. Appl. Phys. 41, 2266.

Jones, R.V. and Richards, J.C.S. (1973). The design and some applications of sensitive capacitance micrometers. J. Phys. E. 6, 589.

Karandikar, R.V. (1959). Investigation of interferometric methods for auroral and airglow studies. Final Report, Boston University, Boston, Contract No. AF19(604)-2172, AFCRC-TR-59-404.

King-Hele, D.G. (1962). Variations of scale height in the upper atmosphere. Nature, 194, 39.

King-Hele, D.G. (1964). The rotational speed at the upper atmosphere determined from changes in satellite orbits. Planet. Space Sci. 12, 835.

King-Hele, D.G., Scott, D.W. and Walker, D.M.C. (1970). Upper atmosphere rotational speed and its variation with height. Planet. Space Sci. 18, 1433.

Knight, W., Kohanzadeh, Y. and Longyel, G. (1968). Evaluation of magnetic defocusing for a photomultiplier tube with large area semitransparent photocathode. Appl. Optics 7, 1115.

Kobler, H. (1963). Servo-techniques in Fabry-Perot Interferometry. Proc. Inst. Radio Engrs. Aust. 24, 677.

Kochanski, A. (1964). Atmospheric motions from sodium cloud drifts. J. Geophys. Res. 69, 3651.

Kohl, H. and King, J.W. (1967). Atmospheric winds between 100 and 700km and their effects on the ionosphere. J. Atmos. Terr. Phys. 29, 1045.

Kondrashov, V.E. and Shefov, A.S. (1964). Method for determining the optical constants and the thickness of semi-transparent layers. Optical constants of multi-alkali metal photocathodes. Bull. Acad. Sci. USSR. Phys. Ser. (USA). 28, 1349.

Kvifte, G. (1959). Auroral and nightglow observations at Å, Norway. J. Atmos. Terr. Phys. 16, 252.

McClure, J.P. (1971). Thermospheric temperature variations inferred from incoherent scatter observations. J. Geophys. Res. 76, 3106.

Meriwether, J.W., Heppner, J.P., Stolarik, J.D., and E.M. Wescott. (1973). Neutral winds above 200 km at high latitudes. J. Geophys. Res. 78, 6643.

Mulyarchik, T.M. (1959). Interferometric measurements of the width of the line λ5577 [OI] in aurora. Izv. Akad. Nauk. SSSR. Ser. Geofiz. 12, 1902.

Nakamura, J.K. and Schwarz, S.E. (1968). Synchronous detection vs. pulse counting for sensitive photomultiplier detection systems. Appl. Optics 7, 1073.

Nilson, J.A.and Shepherd, G.G. (1962). Upper atmospheric temperatures from doppler line widths - I. Some preliminary measurements on OI 5577Å in aurora. Planet. Space Sci. 9, 295.

Oke, J.B. and Schild, R.E. (1968). A practical multiple reflection technique for improving the quantum efficiency of photomultiplier tubes. Appl. Optics 7, 617.

Oliver, C.J. and Pike, E.R. (1968). Measurement of low light flux by photon counting. J. Phys. D: Appl. Phys. 1, 1459.

Phillips, J.G. (1955). The determination of the airglow and twilight flash. The Airglow and the Aurorae. (Ed. Armstrong, E.B. and Dalgarno, A.)

Rambo, B.E. (1964). Improved long wavelength response of photoemissive surfaces. Air Force Avionics Laboratory Tech. Doc. Rept. ALTDR 64-19.

Ramsay, J.V. (1962). A rapid scanning Fabry-Perot interferometer with automatic parallelism control. Appl. Opt. 1, 411.

Ramsay, J.V. (1968). Control of Fabry-Perot interferometers and some unusual applications. The Australian Physicist 5, 87.

Ramsay, J.V., and Mugridge, E.G.V. (1962). Barium titanate ceramics for fine-movement control. J. Sci. Instrum. 39, 636.

Roble,R.G.(1969). A Theoretical and Experimental study of the stable mid-latitude red arc (SAR-arc). Ph.D. Thesis. The University of Michigan.

Roble, R.G., Hays, P.B. and Nagy, A.F. (1970). Photometric and interferometric observations of a mid-latitude stable auroral red arc. Planet. Space Sci. 18, 431.

Roble, R.G. and Dickinson, R.E. (1970). Atmospheric response to heating within a stable auroral red arc. Planet. Space Sci. 18, 1489.

Rodman, J.P. and Smith, H.J. (1963). Tests of photo-multipliers for Astronomical pulse-counting applications. Appl. Optics 2, 181.

Rostoker, G. (1972). Geomagnetic Indices. Rev. Geophys. Space. Sci. 10, 935.

Schaeffer, R.C. (1970). Mid-latitude Airglow and Auroral Phenomena. Ph.D. Thesis. The University of Adelaide.

Shepherd, G.G., Lake, C.W., Miller, J.R. and Cogger, L.L. (1965). A spatial spectral scanning technique for the Fabry-Perot spectrometer. Appl. Opt. 4, 267.

Shepherd, G.G. (1967). Applications of the Fabry-Perot Spectrometer to Upper Atmospheric Spectroscopy. Colloque sur les Methods Nouvelles Spectroscopie Instrumentale. J. Phys. 28, 301.

Slater, P.N., Betz, H.T. and Henderson, G. (1965). A new design of a scanning Fabry-Perot interferometer. Jap. J. Appl. Phys. 4, Supp. 1, 172.

Terrien, J. Hamon,J. and Masui, T. (1957). Profil spectral et causes d'élargisement de quelques radiations hautement monochromatiques du mercure 198. C.R. Acad.Sci. (Paris) 245,926.

Thompson, A.M. (1958). The precise measurement of small capacitances. IEEE Trans. Instr. I-7, 245.

Topp, J.A., Schrötter, H.W., Heicker, H. and Brandmüller, J. (1969). Improvement of the signal-to-noise ratio of photomultipliers for very weak signals. Rev. Sci. Instrum. 40, 1164.

Trutlse, Yu.L. and Yurchenko, O.T. (1971). Temperature of the upper atmosphere from the 6300Å emission data. Planet. Space Sci. 19, 545.

Turgeon, E.C. and Shepherd, G.G. (1961). Upper atmospheric temperatures from Doppler line widths - II Measurements on the OI 5577 and OI 6300 lines in aurora. Planet. Space Sci. 5, 295.

Wark, D.Q. and Stone, J. (1954). Measurement of the doppler width of the λ5577 line in the night sky. Nature, 175, 254.

Wark, D.Q. (1960). Doppler widths of the atomic oxygen lines in the airglow. Astrophys. J. 131, 491.

Young, A.T. (1963). Temperature effects in photomultipliers and astronomical photometry. Appl. Optics 2, 51.

Zwick, H .H. and Shepherd, G.G. (1973). Upper atmospheric temperatures from doppler line widths-V. Auroral electron energy spectra and fluxes deduced from the 5577 and 6300Å atomic oxygen emissions. Planet. Space Sci. 21, 605.